

## Durham E-Theses

---

# *Magic Wavelengths and Dipole-Dipole Interactions in Ultracold RbCs Molecules*

FERNLEY, LUKE, MICHAEL

### How to cite:

---

FERNLEY, LUKE, MICHAEL (2024) *Magic Wavelengths and Dipole-Dipole Interactions in Ultracold RbCs Molecules*, Durham theses, Durham University. Available at Durham E-Theses Online:  
<http://etheses.dur.ac.uk/15710/>

### Use policy

---

The full-text may be used and/or reproduced, and given to third parties in any format or medium, without prior permission or charge, for personal research or study, educational, or not-for-profit purposes provided that:

- a full bibliographic reference is made to the original source
- a [link](#) is made to the metadata record in Durham E-Theses
- the full-text is not changed in any way

The full-text must not be sold in any format or medium without the formal permission of the copyright holders.

Please consult the [full Durham E-Theses policy](#) for further details.

# Magic Wavelengths and Dipole-Dipole Interactions in Ultracold RbCs Molecules

Luke Michael Fernley

---

A thesis submitted in partial fulfilment  
of the requirements for the degree of  
Doctor of Philosophy



**Durham**  
University

Department of Physics  
Durham University

April 2024

# Magic Wavelengths and Dipole-Dipole Interactions in Ultracold RbCs Molecules

Luke Michael Fernley

---

Ultracold polar molecules have become the subject of burgeoning fields of research in recent years owing to their prospects in quantum simulation, quantum computation and precision measurement. Their relatively large ground state dipole moment, coupled with a complex internal structure forms an incredibly powerful toolbox in which to perform quantum science experiments. Unfortunately, spatial confinement using light, which is necessary for many of the aforementioned applications, causes differential ac Stark shifts between quantum states, limiting coherence times and stifling their applicability. By accessing a so-called *magic* condition, this effect can be eliminated.

This thesis presents work towards producing a quantum simulator based on a bulk gas of  $^{87}\text{Rb}^{133}\text{Cs}$  molecules. We develop a magic wavelength trap by exploring nominally forbidden transitions from the  $X^1\Sigma^+$  ground state to  $b^3\Pi_0$  states. By tuning our trapping laser between transitions to different vibrational states of  $b^3\Pi_0$ , we can arbitrarily tune the difference in polarisability between pairs of rotational states and engineer second-scale coherence times. When we trap our molecules in a superposition of rotational states that exhibit a dipole moment in the laboratory frame, we observe the effects of long-range dipole-dipole interactions between molecules. These dipole-dipole interactions form the basis for quantum simulation and computation applications, observations of which marks an important milestone for realising a quantum simulator using  $^{87}\text{Rb}^{133}\text{Cs}$ . We then demonstrate a route to ground state  $^{87}\text{Rb}^{133}\text{Cs}$  molecules that is compatible with a protocol for loading Feshbach molecules into an optical lattice, developed by researchers at the University of Innsbruck. This method can be combined with a magic wavelength trap to produce a sample of  $^{87}\text{Rb}^{133}\text{Cs}$  molecules in a magic lattice. Finally, we engineer synthetic dimensions that simulate simple single-particle Hamiltonians by coupling multiple rotational states in  $^{87}\text{Rb}^{133}\text{Cs}$ . This forms the foundations for utilising rotational states of diatomic molecules as a platform for exploring synthetic dimensions.

# Contents

	Page
<b>1 Introduction</b>	<b>12</b>
1.1 Quantum science with ultracold neutral atoms . . . . .	12
1.1.1 Why polar molecules? . . . . .	14
1.2 Creating ground state ultracold molecules . . . . .	17
1.3 Polar molecule applications . . . . .	19
1.3.1 Quantum simulation . . . . .	19
1.3.2 Quantum computation . . . . .	20
1.3.3 Measurement of fundamental constants . . . . .	22
1.4 Current experimental progress overview in Durham . . . . .	22
1.5 Thesis overview . . . . .	24
<b>2 Theoretical Background</b>	<b>27</b>
2.1 Introduction . . . . .	27
2.2 Structure of RbCs . . . . .	27
2.2.1 Quantum numbers for diatomic molecules . . . . .	28
2.2.2 Vibrational structure . . . . .	30
2.2.3 Rotational structure . . . . .	32
2.2.4 Hyperfine structure . . . . .	32
2.3 RbCs state control . . . . .	33
2.3.1 Zeeman effect . . . . .	34
2.3.2 ac Stark effect in RbCs . . . . .	34
2.3.3 Coupling rotational states . . . . .	37
2.3.4 Dipole-dipole interactions . . . . .	39
<b>3 Experimental Overview and Microwave Control</b>	<b>42</b>
3.1 Making ultracold RbCs molecules . . . . .	42
3.1.1 Atomic mixtures . . . . .	42
3.2 Feshbach association . . . . .	44
3.3 STIRAP . . . . .	46
3.4 Magnetic field coils . . . . .	48

3.4.1	Magnetic field calibration . . . . .	49
3.5	Vacuum upgrades . . . . .	50
3.5.1	Pulling out and breaking vacuum . . . . .	51
3.5.2	Baking vacuum and activating dispensers . . . . .	52
3.6	Microwave sources . . . . .	54
3.6.1	Microwave generators . . . . .	54
3.6.2	Linear monopole and microwave horn . . . . .	55
3.6.3	Characterising microwave polarisation . . . . .	55
3.6.4	Engineering arbitrary polarisations using phased-arrays . . . . .	59
3.6.5	Dipole antennae array . . . . .	60
<b>4</b>	<b>Magic Spectroscopy</b>	<b>63</b>
4.1	Introduction . . . . .	63
4.1.1	RbCs rotational magic background . . . . .	64
4.1.2	RbCs rotational magic theory . . . . .	65
4.2	Experimental setup . . . . .	68
4.2.1	Scanning transfer cavity locking . . . . .	69
4.2.2	STCL testing . . . . .	71
4.2.3	PDH locking . . . . .	73
4.3	$b^3\Pi_0$ vibrational structure at 181.5 G . . . . .	74
4.4	$b^3\Pi_0$ rotational structure at 181.5 G . . . . .	75
4.4.1	Zeeman shifts of the excited state . . . . .	76
4.4.2	HF structure overview . . . . .	76
4.5	Linewidths . . . . .	79
4.5.1	Partial linewidths . . . . .	79
4.5.2	Total linewidths . . . . .	82
4.6	Finding the rotationally magic detuning . . . . .	83
4.6.1	Coarse spectroscopy . . . . .	83
4.6.2	High-resolution spectroscopy . . . . .	85
4.7	Ramsey interferometry at rotationally magic detuning . . . . .	87
4.8	STIRAP magic . . . . .	87
4.9	Analysis of results . . . . .	89
4.10	Summary . . . . .	90
<b>5</b>	<b>Magic Trapping and Dipole-Dipole Interactions</b>	<b>91</b>
5.1	Introduction . . . . .	91
5.2	Magic trapping overview . . . . .	92
5.3	Magic trapping setup . . . . .	94
5.3.1	Lifetimes in the magic trap . . . . .	95
5.4	Identifying the rotationally magic detuning with Ramsey . . . . .	97
5.5	Long coherence times . . . . .	99

5.6	Observation of dipole-dipole interactions . . . . .	100
5.7	Spin echo efficacy . . . . .	102
5.8	Phase slip in Ramsey fringes . . . . .	102
5.9	Tuning dipole-dipole interactions . . . . .	103
5.10	Sources of non-dipolar decoherence . . . . .	104
5.10.1	Instability in trap laser frequency . . . . .	104
5.10.2	Uncertainty in magic from Ramsey optimisation . . . . .	105
5.10.3	10 MHz difference in trapping beams . . . . .	105
5.10.4	Magnetic field instability and total coherence limit . . . . .	105
5.11	Summary . . . . .	106
<b>6</b>	<b>Towards Molecules in Lattices</b>	<b>107</b>
6.1	Introduction . . . . .	107
6.2	Innsbruck Method . . . . .	108
6.3	Theoretical calculations . . . . .	110
6.4	Shorthand state notation . . . . .	111
6.5	Associating at $\sim 352.74$ G . . . . .	111
6.6	Searching for strong STIRAP transitions . . . . .	113
6.7	RF-assisted avoided crossing jumping . . . . .	113
6.8	Continued pump spectroscopy and pump Rabi oscillations . . . . .	117
6.9	Stokes Spectroscopy at 305 G . . . . .	117
6.10	Identifying ground state occupancy with MW spectroscopy . . . . .	120
6.11	Stokes Rabi oscillation at 305 G . . . . .	122
6.12	Summary . . . . .	122
<b>7</b>	<b>Synthetic Dimensions in RbCs</b>	<b>124</b>
7.1	Introduction . . . . .	124
7.2	Synthetic dimensions in RbCs . . . . .	125
7.3	Controlling relative synthetic lattice site depths . . . . .	129
7.4	Controlling synthetic lattice site hopping . . . . .	129
7.5	SSH model . . . . .	131
7.6	Summary . . . . .	133
<b>8</b>	<b>Conclusion</b>	<b>135</b>
8.1	Summary . . . . .	135
8.2	Outlook . . . . .	137
8.2.1	Plans for a magic lattice . . . . .	137
8.2.2	Interactions in 1D lattice pancakes. . . . .	138
8.2.3	3-level interacting system . . . . .	139
8.2.4	Interacting SSH model . . . . .	140
8.3	Concluding remarks . . . . .	141

<b>9</b>	<b>Appendix</b>	<b>142</b>
9.1	Analytical solutions to multi-level systems . . . . .	142
9.1.1	2-level eigenvalues and eigenvectors . . . . .	142
9.1.2	3-level eigenvalues and eigenvectors . . . . .	143
9.1.3	4-level SSH eigenvalues and eigenvectors . . . . .	144

# List of Figures

Figure	Page
1.1 Dipole-dipole interactions with neutral atoms . . . . .	14
1.2 Atomic and molecular structure . . . . .	16
1.3 Photoassociation and magnetoassociation . . . . .	18
1.4 Overview of the Durham experiment . . . . .	23
2.1 Relevant Hund's cases . . . . .	28
2.2 RbCs structure overview . . . . .	31
2.3 Coordinate system for describing ac Stark shifts . . . . .	35
2.4 ac Stark shifts in $N = 1$ RbCs with vertically and horizontally polarised light . . . . .	37
2.5 Rotational state coupling in RbCs . . . . .	38
2.6 Dipole-dipole interactions with molecules . . . . .	39
3.1 Experimental setup overview . . . . .	43
3.2 Association and dissociation steps . . . . .	45
3.3 STIRAP pulse sequence overview . . . . .	46
3.4 Magnetic field calibration . . . . .	50
3.5 Vacuum maintenance: pumping down . . . . .	52
3.6 Vacuum maintenance: baking . . . . .	53
3.7 Vacuum maintenance: activating dispensers . . . . .	54
3.8 Microwave sources diagram . . . . .	56
3.9 Microwave polarisation determination . . . . .	57
3.10 Phased array experiment . . . . .	60
3.11 Antenna scalar-network analyser setup . . . . .	62
4.1 Rotationally magic trap scheme . . . . .	65
4.2 Homebuilt probe laser setup for $X \rightarrow b$ spectroscopy . . . . .	68
4.3 Commercial laser setup for $X \rightarrow b$ spectroscopy . . . . .	70
4.4 STCL beat note analysis . . . . .	72
4.5 Low-lying vibrational structure of $b^3\Pi_0$ . . . . .	74

4.6	Rotational structure of $b^3\Pi_0(v' = 0)$ . . . . .	77
4.7	Zeeman shifts in $X^1\Sigma^+(v'' = 0) \rightarrow b^3\Pi_0(v' = 0)$ transitions . . .	78
4.8	Partial linewidths of $b^3\Pi_0$ states . . . . .	81
4.9	Total linewidths of $b^3\Pi_0$ states . . . . .	82
4.10	Coarse spectroscopy of rotational transitions in the presence of probe light . . . . .	84
4.11	High-resolution spectroscopy of rotational transitions in the presence of probe light . . . . .	86
4.12	Ramsey interferometry in the presence of probe light . . . . .	88
5.1	Magic trapping overview . . . . .	93
5.2	Magic trap setup . . . . .	96
5.3	Lifetime of molecules in the trap . . . . .	97
5.4	Bloch spheres and pulse sequences . . . . .	98
5.5	Finding magic using Ramsey . . . . .	99
5.6	Second-scale coherence between different rotational states . . .	101
5.7	Spin echo efficacy and phase slip . . . . .	103
5.8	Tuning dipole-dipole interactions in the magic trap . . . . .	104
6.1	Intraspecies and interspecies scattering lengths and inter- species miscibility . . . . .	109
6.2	STIRAP energy levels and theoretical proposition for STIRAP transfer at 305 G . . . . .	110
6.3	Feshbach resonance search between $\sim 300$ and $\sim 360$ G . . . . .	112
6.4	Pump spectroscopy as a function of magnetic field . . . . .	113
6.5	Landau-Zener avoided crossing and dressed-state picture . . .	115
6.6	RF-avoided crossing transfer scheme and efficiency . . . . .	116
6.7	Pump spectroscopy showing occupation of $sd_6$ state and Rabi oscillation on pump transition . . . . .	118
6.8	Stokes spectroscopy at 305 G . . . . .	119
6.9	Ground state occupation after STIRAP transfer . . . . .	120
6.10	Rabi oscillation of Stokes transition at 305 G . . . . .	121
7.1	Synthetic dimension mapping . . . . .	126
7.2	Rotational synthetic dimension map in RbCs . . . . .	128
7.3	Controlling relative site depths in the synthetic dimension. . .	130
7.4	Controlling the hopping between adjacent sites in the syn- thetic dimension . . . . .	131
7.5	Probing the SSH synthetic dimension . . . . .	133
8.1	Interacting lattice pancakes . . . . .	139
8.2	Interacting three-level system . . . . .	140

---

8.3 Interacting SSH . . . . .	141
-------------------------------	-----

# List of Tables

3.1	Polarisation of microwaves produced by $\lambda/4$ antenna and Horn	58
3.2	Polarisation of microwaves produced by North and South dipole antennae . . . . .	61
4.1	Absolute $X^1\Sigma^+(v'' = 0, N'' = 1) \rightarrow b^3\Pi_0(v', N' = 0)$ transition frequencies . . . . .	75
4.2	Features identified in spectroscopy of $X^1\Sigma^+(v'' = 0) \rightarrow b^3\Pi_0(v' = 0)$ transitions . . . . .	79
4.3	Features identified in spectroscopy of $X^1\Sigma^+(v'' = 0) \rightarrow b^3\Pi_0(v' = 1)$ transitions . . . . .	80
4.4	$X^1\Sigma^+(v'' = 0, N'' = 1) \rightarrow b^3\Pi_0(v' = 2, N'' = 0)$ transition . . .	80
4.5	Transition frequencies, partial linewidths and total linewidths	90
6.1	Confirmation of $X^1\Sigma^+$ state occupation after STIRAP at 305 G	122
6.2	Summary of STIRAP transitions at 181.5 and 305 G . . . . .	122

# Acknowledgements

I guess this is the opportunity for me to be a bit poetic, or at the very least expressive, but at the moment my head is awash with Ramsey fringes, scattering lengths and Feshbach resonances and I'm fighting the urge to just list off names with bullet points. But given a PhD an experience that lasts for the best part of 4 years, I'll put aside my current mindset and make an effort to show my appreciation for the people who helped me along the way.

First and foremost, I have to express my deepest gratitude to my supervisor Professor Simon Cornish. Simon's enthusiasm and fantastic eye for detail can't help but transfer to his students. He exudes a passion for science which leads to an invigorating research environment. I can honestly say I would not have developed anywhere near as much as a scientist without his supervision.

Working in an ultracold molecule lab is often fraught with complications. The results it produces can never really be attributed to one person, but to a collaborative team and I am thankful to have been part of a team that was collaborative and nurturing. I'd like to thank the resident post-doc of PH60, Phil Gregory, for if nothing else his supreme patience with me. With an almost encyclopedic knowledge of RbCs and his pragmatism and drive in the lab, he has been a fantastic person to work alongside and learn from. I think it's safe to say the experiment would be nowhere near what it is today without him. Good luck with the new experiment! To other members of PH60 (past and present), Albert, Arpita, Jake and Fritz, you have been wonderful to work with and I know the experiment will continue to flourish because of your efforts.

QLM in Durham has a welcoming and supportive atmosphere. I'm afraid I will just resort to listing names here as there are too many people that deserve a personalised shout-out. To the rest of the "Cornish empire": Alex ( $\times 2$ ), Dan, Tom, Tobias, Jack, Joe, Ben, Jonathan, Adarsh. It's been brilliant being able to work alongside you. Thank you to the 2020 QLM cohort:

Anton, Vivek, Joe, Jack, Toon, Ben and Dan (whom I still owe a pint). Arriving at a new place is always difficult, especially during covid, but being greeted by some friendly faces really helped get me settled. Thank you to the QLM football squad, especially the CEOs: Puya, Fraser, and Matt (for showing me not all Mackems are that bad). Thank you to the rest of QLM: Giannluca, Bethan, Archie, Liam, Mitch, Jack etc and the weekly cake club.

To my annual review team, Professor Ifan Hughes and Professor Matthew Jones. Having such accomplished and friendly academics as my reviewers helped put the work into perspective. Thank you to the QLM workshop team members who helped me along the way, especially John, Fabrice, Andrew and Rob who responded to my many urgent problems with haste.

To my Southampton Physics cohort: Vik, Lumber, Afro, James and Dan. Working through problem sheets, past papers and going to Jesters made for some of the best years of my life. Thank you also to my personal tutor D.C. Smith for supporting me throughout undergrad.

Outside of academia, I want to thank the people in I have met and spent time with in Durham: Sean, Mo, Andrew, Adam, Brad, Nick and Georgie. To the TTDE guys, thank you for all the years of invaluable friendship. To the online boys, thank you for taking my mind off the lab so that we could “collect some dubs” (or at least try). Prior to university, I’d like to thank my A-level teachers, Mr Cobbold and Mr Friend, for igniting my love of physics and encouraging me to pursue a life in science, for better or for worse.

Finally, to Mum, Dad and Jack. Thank you for all the support of the years, it really has helped. I appreciate your attempted interest as I tried to explain what I do. Mum, thanks for being there to help re-ground myself and offer some kind words. Dad, thanks for your philosophical wisdom you’ve tried to impart over the years. I’ll try to remember to “go placidly”. All my love.

# Chapter 1

## Introduction

### 1.1 Quantum science with ultracold neutral atoms

The field of ultracold atomic research has exhibited exciting growth in recent decades, ignited by the pioneering work of [1–3] at the turn of the millennium. Scientific minds around the world turned their attention towards interacting atomic systems, spurred on by the prospect of a plethora of scientific and technological applications in the fields of quantum metrology [4, 5], quantum computation and simulation [6–8] and quantum chemistry [9, 10] just to name a few.

An aspect that is of particular interest to us is that of quantum simulation. For these applications, neutral atoms become the foundation on which to imprint and extract information using their internal quantum states. The internal states then act as analogies to the properties of their simulated counterpart. As an example, the hyperfine states of atoms can be used to encode pseudo-spins to engineer the Hamiltonians found in condensed matter physics such as the Ising spin or Bose-Hubbard models [11–14].

Realising a successful quantum simulator is predicated on a few general requirements:

1. Access to tunable long-range interactions.
2. Interaction times are appropriately long.
3. Sufficient quantum coherence.

Let's examine the first point above. Long-range interactions facilitate entanglement between neighbouring atoms in a quantum simulator. Short-range collision-based interactions are not desirable<sup>1</sup>. The key to engineering long-range interactions with neutral atoms is utilising their magnetic or electric dipole moments. Interactions between dipoles are hence termed 'dipole-dipole' interactions with interaction strength given by [17, 18]

$$V_{dd} = \frac{(\mathbf{d}_i \cdot \mathbf{d}_j) r^2 - 3(\mathbf{d}_i \cdot \mathbf{r})(\mathbf{d}_j \cdot \mathbf{r})}{r^5}, \quad (1.1)$$

where  $\mathbf{d}_i$  ( $\mathbf{d}_j$ ) is the dipole moment of the  $i^{\text{th}}$  ( $j^{\text{th}}$ ) dipole and  $\mathbf{r}$  is the vector connecting the two dipoles with magnitude  $r$ .

Considering the case where dipoles are aligned in the same spatial direction as illustrated in Fig. 1.1(a), Eq. 1.1 reduces to the form

$$V_{dd} = \frac{C_{dd}}{4\pi} \frac{1 - 3 \cos^2(\theta)}{r^3}, \quad (1.2)$$

where  $V_{dd}$  is the strength of the dipole-dipole interaction and  $C_{dd}$  is the dipole-dipole coupling constant which is proportional to the product of the magnitude of the dipole moments of the interacting dipoles.  $r$  is the magnitude of the separation and  $\theta$  is the angle between the axis of the direction of the dipoles and a vector connecting interacting dipoles. Dipoles can be aligned through the presence of an external field.

The second condition requires that interactions occur on the time scale of typical interaction strengths. This is dependent on the interplay between dipolar interaction strength and the interaction time, and allows the resulting Hamiltonian to carry out significant evolution owing exclusively to the dipolar interactions. Ensuring enough interaction time is achieved by spatially confining the atom, or 'trapping', for example in an optical lattice potential as illustrated in Fig. 1.1(b). The value of  $C_{dd}$  in Eq. 1.2 is a property of the interacting states and  $r$  in Eq. 1.2 is dictated by the distance between 'sites' where trapped atoms reside. The key is to engineer a system where the interacting dipoles are close enough together and held for a long enough time.

The final requirement is more subtle. Quantum states of atoms must maintain their appropriate character to protect the fidelity of the interactions. The evolution of quantum states is fragile and susceptible to influence

---

<sup>1</sup>Collisions lead to loss and chaotic effects [15, 16].

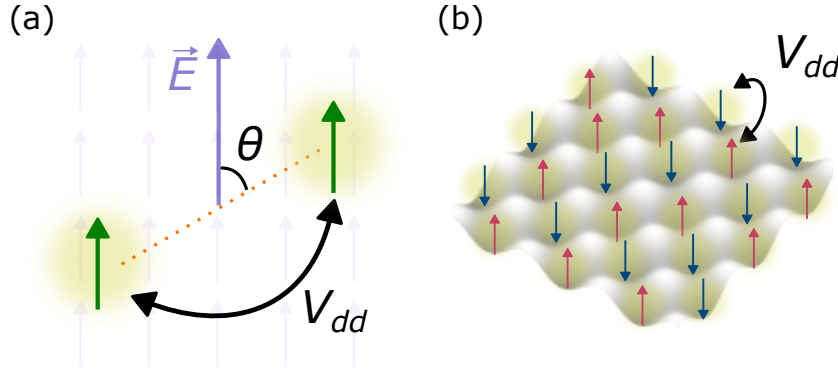


**Figure 1.1:** Dipole-dipole interactions and dipoles in lattices. (a) Dipole-dipole interaction with interaction strength  $V_{dd}$  between two dipoles aligned using an external field,  $\vec{E}$ . (b) Dipoles confined to a 2D lattice potential aligned or anti-aligned using an external field, appropriate for simulating models such as XXZ Hamiltonians.

by external fields. It's important to eliminate or at least minimise these effects.

### 1.1.1 Why polar molecules?

Unfortunately, the majority of neutral atoms with practical cooling mechanisms do not possess a large dipole in their ground quantum state. There are notable exceptions such as Dysprosium [19], Erbium [20] and Chromium [21] which have a substantial magnetic dipole moment  $\mu$  owing to the high ground state angular momentum. Given typical experimental parameter orders of magnitude,  $\mu \sim 10$  Bohr magneton,  $\mu_B$ , and separations  $\sim 500$  of nm we can expect interaction strengths of  $\sim 10$  Hz.

Alternatively, one can take advantage of exciting ground state neutral atoms to an excited state with a large principal quantum number,  $n$ . Increasing the Kepler radius of the electron orbital brings with it an exceptionally large electric dipole moment,  $d$ , that scales with  $n^4$  [22, 23]. These atoms are known as ‘Rydberg’ atoms. Current experiments typically access  $n$  between 50 and 60 (leading to an electric dipole moment of between  $\sim 100$  and 1000 Debye, D,  $1 \text{ D} \sim 3.335 \times 10^{30} \text{ C}\cdot\text{m}$ .), allowing for exceedingly fast Hamiltonian evolution times [24]. With typical experimental spacing of  $\sim 1 \mu\text{m}$ , the interaction strength is on the order of  $\sim 100$  MHz.

Both magnetic atoms and Rydberg atoms are spatially confined using optical trapping potentials [25], however in the case of Rydberg atoms, interaction times are limited by radiative lifetimes. Rydberg atoms decay rapidly from their Rydberg state. As the principal quantum number of the Rydberg atom increases, the lifetime of the state increases with a dependence of  $n^3$  leading to typical Rydberg atom lifetimes on the order of  $\sim 10/100\mu\text{s}$ <sup>2</sup>. For magnetic atoms, the ground states possess a permanent dipole moment and so support long lifetimes.

Regarding the third requirement in section 1.1, magnetic atoms are limited in coherence by magnetic field noise to  $\sim 500\mu\text{s}$  [27]. For quantum computing purposes, magnetic atoms are typically doped in nanophotonic structures, yielding coherence times exceeding 1 second [28, 29]. Typically, sources of decoherence in a Rydberg atomic system arise from differential ac Stark shifts caused by the trapping light or from motional states of the trapped atoms [30]<sup>3</sup>. However, in Rydberg systems, coherence times are on the order of  $1 \times 10^4$  greater than the Rydberg state lifetime [26], hence lifetime is typically the limiting factor in the case of Rydberg atoms.

However, there is another option, straying away from the realm of atoms and instead looking towards polar molecules. Molecules offer a middle ground between magnetic and Rydberg atoms. Polar molecules possess a substantial molecule-frame electric dipole moment of order  $\sim 1\text{ D}$  in their ground state. With the typical experimental spacing of molecules ( $\sim 500\mu\text{m}$  in an optical lattice), interaction strengths are of the order  $\sim 1\text{ kHz}$ . Moreover, molecules have a rich internal structure which serves as a powerful toolbox in which to encode and store quantum information as presented in Fig. 1.2<sup>4</sup>. Moreover, the multitude of hyperfine states available in each rotational manifold allows for great tunability of dipolar interaction strength with external fields [31], making polar molecules fantastically versatile.

Quantum simulators based on dipolar molecules may be used to understand complex many-body phenomena, such as those underpinning quantum magnetism [17, 32–35], superconductivity [36] and quantum phase transitions [37–39]. Simulation architectures exploit the rotational structure of ground state dipolar molecules. The symmetry of rotational states leads to a net zero lab frame dipole moment. However, coupling different rotational

<sup>2</sup>Rb<sup>87</sup> in the  $70\text{ S}_{1/2}$  Rydberg state exhibits a lifetime of  $150\mu\text{s}$  [26]

<sup>3</sup>Rydberg atom coherence times have been extended to 1.5 seconds using XY16-128 pulse sequences [26].

<sup>4</sup>The structure of  $^{87}\text{Rb}^{133}\text{Cs}$  is discussed in more detail in chapter 2

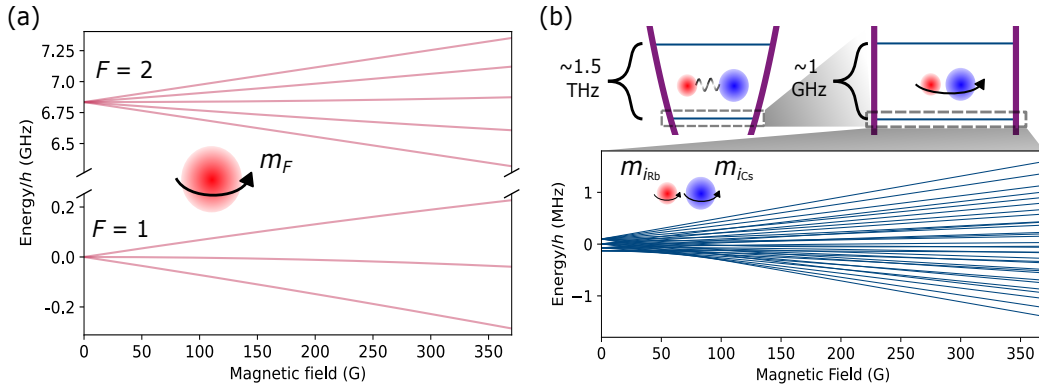


**Figure 1.2:** Atomic and molecular energy level structures. The inset cartoon shows the degree of freedom causing splittings in each case. (a)  $5^2S_{1/2}$   $^{87}\text{Rb}$  Breit-Rabi diagram. (b)  $^{87}\text{Rb}^{133}\text{Cs}$  rovibrational and hyperfine structure. Top left, vibrational energy splitting on the order of  $\sim 1.5$  THz. Top right, rotational energy splitting of the lowest energy vibrational state. Energy splitting between lowest and second-lowest rotational states  $\sim 1$  GHz. Lower plot, the hyperfine structure of the lowest rovibrational state of  $^{87}\text{Rb}^{133}\text{Cs}$ . 32 different hyperfine states are present.

states using an external electric or microwave field induces tunable dipolar interactions. These rotational states are anharmonically separated on the order of  $\sim$  GHz, allowing for specific addressing of rotational state couplings.

As with Rydberg atoms, ultracold dipolar molecules are confined using optical traps. Recently, researchers have begun exploring and controlling the internal structure of polar molecules for use in quantum science [40–43], however short coherence times between different rotational states have made observations of dipolar interactions difficult, primarily caused by differential ac Stark shifts from the trapping light [44–49]. In this work, we develop a method of accessing dipolar interactions by engineering long coherence times in  $^{87}\text{Rb}^{133}\text{Cs}$  molecules (hereafter RbCs). This is accomplished by tuning the wavelength of the trapping light to access a so-called *magic* condition where differential ac Stark effects are eliminated. Additionally, we present a method for transferring molecules to the ground state which is compatible with a technique for loading molecules into an optical lattice developed by the University of Innsbruck [50] and present results utilising different rotational energy states of RbCs as a method of simulating real spatial dimensions.

## 1.2 Creating ground state ultracold molecules

Methods for creating ultracold ground state polar molecules generally fall into one of two categories; *direct* and *indirect* methods. Direct methods involve producing ground state diatomic molecules and subsequently cooling and trapping them with laser light. Indirect methods involve creating separate ultracold samples of each atomic species and associating them using a photon (photoassociation) or by sweeping an external magnetic field over an interspecies Feshbach resonance (magnetoassociation).

Direct methods utilise transitions to different electronic states as the basis for a laser cooling scheme. With a greater number of states available and a greater number of photons to be scattered to reach a given temperature, it is often more difficult to laser cool molecules compared to atoms. Certain criteria about the molecular structure must be fulfilled for effective production of ground state molecules using direct methods [51]. As with the laser cooling of atoms, molecules must possess an excited state with a suitably short lifetime and can form part of a cooling cycle which is sufficiently closed [52].

There is no vibrational quantum number selection rule that governs electronic transitions. Instead, the decay rates along different pathways from an excited state are given by wavefunction overlap which is described by the Franck-Condon matrix. The most appropriate molecules for direct cooling have a highly-diagonal Franck-Condon matrix with minimal intervening electronic states, minimising decay outside the proposed cooling cycle. In these schemes, minimal change to the molecular geometry occurs during excitation. As with atomic cooling schemes, repump lasers are implemented to pump the populations back into the cooling cycle [53]. These typically target transitions to other vibrational states in the electronic ground state. Diatomic molecules which have been cooled and trapped with lasers include SrF [54], CaF [55, 56], YO [57], YbF [58], BaH [59] and TiO [60]. It is also noted that molecules such as Sr<sub>2</sub> have been created using STIRAP and then a second STIRAP sequence can be used to transfer molecules to the ground state [61].

Photoassociation is a fantastic tool for molecular spectroscopy [62, 63] and for probing the scattering properties of atoms [64, 65], however it can also be implemented to create ground state molecules. The general principle is that colliding atoms with energy  $E_{\text{FA}}$  can absorb a photon,  $\gamma_{\text{PA}}$ , and associate into a bound state as illustrated in Fig. 1.3(a). The molecule then occupies an excited electronic state which readily decays, in some instances

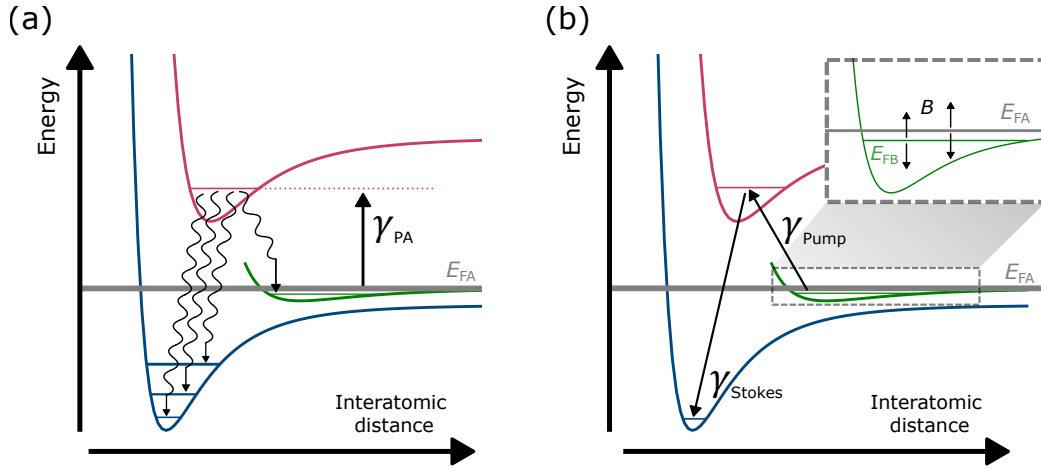


**Figure 1.3:** Photoassociation and magnetoassociation diagrams. Blue and red curves are the ground and excited electronic states respectively. The green curve is the Feshbach state that is occupied after the magnetoassociation presented in (b). (a) Photoassociating atoms into molecules. Transitions from atoms in a free atom pair state with energy  $E_{FA}$  (grey horizontal line) to an excited state (red horizontal line) are facilitated by a photon,  $\gamma_{PA}$ . Molecules in the excited state potential then readily decay through various channels. The relative probabilities of a molecule following specific decay channels are dictated by Franck-Condon factors. (b) Magnetoassociating atoms into molecules. Applying an external magnetic field allows the tuning of energy of the bound state,  $E_{FB}$ , with respect to the free atom pair state. Sweeping the magnetic field over the region these states are degenerate in energy forms a weakly bound Feshbach molecule. The Feshbach molecule is then transferred to the ground state with hyperfine resolution using STIRAP, a two-photon transition facilitated by pump and Stokes lasers,  $\gamma_{pump}$  and  $\gamma_{Stokes}$ .

to the ground state [66]. However, the multitude of electronic, vibrational, rotational and hyperfine decay pathways makes ground state production using photoassociation an undesirable approach.

Magnetoassociation, which we adopt in our experiment, uses a Feshbach resonance to create a weakly bound molecule which is then transferred to a more deeply bound state with a two-photon transfer process. Pioneered in 2003 by researchers in JILA in the creation of  $K_2$  [67], magnetoassociation has become arguably the most robust route to diatomic molecules. In the context of creating heteronuclear molecules, the process begins with a high phase-space-density mixture of two species in an external magnetic field. The magnetic moment of the free atoms is typically different to that of bound states, allowing the relative energy of the free atoms and bound states to

be controlled by varying the strength of the external field as illustrated in Fig. 1.3(b). If the magnetic field is swept over the region where the bound state and the free atoms are degenerate in energy, the free atom state can adiabatically follow an avoided crossing, forming a weakly-bound Feshbach molecule. This process is described using Landau-Zener theory [68]. The Feshbach molecules are then transferred to a more deeply bound ground state with stimulated Raman adiabatic passage (STIRAP). Heteronuclear diatomic molecules created using Feshbach association include KRb [69, 70], RbCs [71, 72], NaK [73–76], NaRb [77], NaCs [78], LiK [79] and NaLi [80].

## 1.3 Polar molecule applications

We shall briefly summarise some of the many applications of polar molecules.

### 1.3.1 Quantum simulation

Consider the situation where molecules are confined to individual lattice sites in the limit where site depth is sufficient that tunnelling between sites is neglected. Two rotational states can be used to encode pseudo-spin information describing many-body systems with spin states  $|\uparrow\rangle$  and  $|\downarrow\rangle$  being “mapped” onto rotational states. Rotational states are defined using  $|N, M_N\rangle$  where  $N$  is the rotational quantum number and  $M_N$  the projection of  $N$  onto the quantisation axis. With single-site occupancy in a 2-dimensional optical lattice and dipolar interactions between sites defined by Eq. 1.1, the system dynamics are described by the XXY Hamiltonian [81, 82]

$$\hat{H}_{\text{XXZ}} = \frac{1}{2} \sum_{i \neq j} \frac{1 - 3 \cos^2 \theta_{ij}}{r^3} \left[ \frac{J_{\perp}}{2} (\mathbf{S}_i^+ \mathbf{S}_j^- + \mathbf{S}_i^- \mathbf{S}_j^+) + J_z \mathbf{S}_i^z \mathbf{S}_j^z \right], \quad (1.3)$$

where  $\mathbf{S}_{i,j}$  are spin-1/2 operators and  $\theta_{ij}$  is the angle between the dipole moments and the vector connecting different dipoles  $i$  and  $j$ .  $J_{\perp}$  describes the dipole-dipole coupling strength and  $J_z$  describes Ising interactions. The specific values of  $J_{\perp}$  and  $J_z$  can be tuned by varying the states used to encode pseudo spins.

By considering two sets of  $|N, M_N\rangle$  states, we can show the tunability of interaction strengths by simply changing the states used in the simulation. For  $\{|\downarrow\rangle, |\uparrow\rangle\} = \{|0, 0\rangle, |1, 0\rangle\}$ ,  $J_{\perp} = 2d_{\downarrow\uparrow}^2$  for and  $J_z = (d_{\uparrow} - d_{\downarrow})^2$ . For  $\{|\downarrow\rangle, |\uparrow\rangle\} = \{|0, 0\rangle, |1, 1\rangle\}$ ,  $J_{\perp} = -d_{\downarrow\uparrow}^2$  and  $J_z = (d_{\uparrow} - d_{\downarrow})^2$  [83, 84].  $d_{\downarrow}$ ,  $d_{\uparrow}$  and  $d_{\uparrow\downarrow}$  are the dipole moments given by the expectation value of the dipole

operator  $d$ .  $d_{\downarrow\uparrow}$  represents the transition dipole moment for the  $|0, 0\rangle \rightarrow |1, 0\rangle$  transition,  $\langle 0, 0 | d | 1, 0\rangle$  [85, 86]. Similarly,  $d_{\downarrow\uparrow}$  pertains to the  $|0, 0\rangle \rightarrow |1, 1\rangle$  transition. Tuning the values of  $J_{\perp}$  and  $J_z$  allows the simulation of different models. For example, setting  $J_{\perp} = 0$ ,  $J_z = 0$  or  $J_{\perp} = J_z$  transforms Eq. 1.3 into the Ising, XY and Heisenberg models respectively.

Moving away from the tight binding limit whereby molecules can tunnel between lattice sites, the system is described by the Bose-Hubbard model given by [87, 88]

$$\hat{H}_{\text{BH}} = -J \sum_{\langle i,j \rangle} \hat{b}_i^\dagger \hat{b}_j + V \sum_{i < j} \frac{\hat{n}_i \hat{n}_j}{r_{ij}^3} - \sum_i \mu \hat{n}_i, \quad (1.4)$$

where  $\langle i, j \rangle$  represents the nearest-neighbour sites  $i$  and  $j$ ,  $\hat{b}_j^\dagger$  ( $\hat{b}_i$ ) are the bosonic creation (annihilation) operator of the lattice site  $i$  and h.c. is the hermitian conjugate.  $V$  is the dipolar interaction between sites separated by a distance  $r$  and  $\hat{n}_i$  is the number operator at site  $i$ .  $\mu$  is the chemical potential. Tuning the dipole-dipole interaction facilitates Mott-solid to superfluid phase transitions.

Finally, without the need for lattice confinement, the internal quantum states of molecules can be harnessed to simulate spatial positions in real dimensions [89, 90]. This is known as a *synthetic dimension*. For example, with diatomic molecules, a real 1-dimensional landscape, such as the position of a particle in a 1-dimensional optical lattice potential, can be imitated as a synthetic dimension engineered using rotational angular momentum states. The rotational energy states form the analogy for positions in an optical lattice where each site in the real lattice potential can be mapped onto a rotational energy state of the molecule. Tunnelling between sites in the synthetic dimension is controlled by varying the power of the microwaves that couple different rotational states together. Synthetic dimensions offer a highly tunable structure compared to their real-dimensional counterpart, can be enriched by dipolar interactions [91, 92] and combined with real dimensions to simulated higher-dimensional systems [93, 94].

### 1.3.2 Quantum computation

Binary data can be encoded onto a superposition of two quantum states,  $|0\rangle$  and  $|1\rangle$ , forming a *qubit*. Qubits are the building blocks of quantum computers which are transformed in calculations using "gate" operations. Typically,

molecular gates are proposed using an array of individual tight optical potentials called *tweezers* [95] although schemes for molecular gates using an array of molecules have been proposed which could be accomplished with lattice potentials [96]. Using tweezers, the position of molecules can be controlled so that quantum states can be initialised, stored and read-out away from the locations where gate operations are performed. We highlight a proposal from Ni *et al.* [97] for an iSWAP gate using two polar molecules.

In [97], dipole-dipole interactions facilitate the exchange of ground and excited states between the molecules. Consider two molecules occupying separate hyperfine states in the ground rotational manifold, given by  $|0\rangle$  and  $|1\rangle$ . A microwave  $\pi$ -pulse transfers the molecule in  $|1\rangle$  to an excited state  $|e\rangle$ .  $|e\rangle$  is chosen such that there is a transition dipole moment coupling to both  $|0\rangle$  and  $|1\rangle$ . The molecule-molecule interaction is described in the  $\{|0, 0\rangle, |0, e\rangle, |e, 0\rangle, |e, e\rangle\}$  basis with the first and second positions in the state labelling referring to the first and second molecule respectively by

$$\hat{U} = e^{-i\hat{H}t/\hbar} = \begin{pmatrix} 1 & 0 & 0 & 0 \\ 0 & \cos(\Omega t) & i \sin(\Omega t) & 0 \\ 0 & i \sin(\Omega t) & \cos(\Omega t) & 0 \\ 0 & 0 & 0 & 1 \end{pmatrix}, \quad (1.5)$$

where  $\Omega = D/r^3$ ,  $D$  is the dipole-dipole interaction strength and  $r$  is the intermolecular distance. To perform an iSWAP operation,  $t = \pi/(2\Omega)$ . Recently, researchers in Princeton and Harvard Universities [40, 42] have produced an experiment that deterministically prepares Bell states pairs of molecules in reconfigurable tweezer arrays. They demonstrate the iSWAP gate proposed in [97] with  $\sim 0.8$  fidelity, limited by single molecule decoherence times.

Many current quantum computing architectures have problems with scalability [98]. Forming a large Hilbert space for more advanced computations is difficult. Minimising this issue can be accomplished by using higher-dimensional quantum bits, known as *qudits*, which hold more information than qubits. In Sawant *et al.* [99], they proposed a protocol for utilising different rotational states of dipolar molecules as a qudit platform which demonstrated that the number of  $d$ -dimensional qudits which hold the equivalent information of  $n$  qubits is about  $n/\log_2(d)$ . The current record for the number of logical qubits used in gate operations is held by the Lukin group [100] with 48 logical qubits based on reconfigurable Rydberg atom tweezer arrays. In the RbCs lab in Durham, we have reached up to  $N = 6$  [101]. A

7-dimensional qudit system comprising 17 molecules would contain similar information to the one demonstrated in [100].

### 1.3.3 Measurement of fundamental constants

A diatomic molecule's state energies are sensitive to perturbations in external electric fields, making them prime candidates for precision measurement. Most prominently, polar molecules are utilised for measuring the electron electric dipole moment (eEDM) [102]. CP symmetry violation, which is included in many extensions to the standard model of particle physics, predicts a non-zero value of the eEDM [103]. Placing limits on the value of the eEDM disproves some of the standard model extensions.

The internal electric field serves as a probe for the eEDM. The eEDM would either be aligned or anti-aligned to the molecule's electric field leading to an energy shift equal to  $\mathbf{d}_e \cdot \mathbf{E}_{\text{mol}}$  where  $\mathbf{d}_e$  is the eEDM and  $\mathbf{E}_{\text{mol}}$  is the electric field across the molecule. The experiments at the forefront of eEDM precision measurement are the ACME collaboration using ThO [104], Imperial College London using YbF [105] and JILA using HfF<sup>+</sup> molecules [106]. The latter of these three boasts the most accurate eEDM limit to date of  $|d_e| < 4.1 \times 10^{-30} e \text{ cm}$  at 90% confidence.

## 1.4 Current experimental progress overview in Durham

As will become apparent in later chapters (particularly chapter 3), the bulk RbCs experiment in Durham is a culmination of almost two decades of work from many different Master's, post-graduate and post-doctorate researchers. In an effort to contextualise the results presented in this thesis, Fig. 1.4 presents a summary of key experimental milestones.

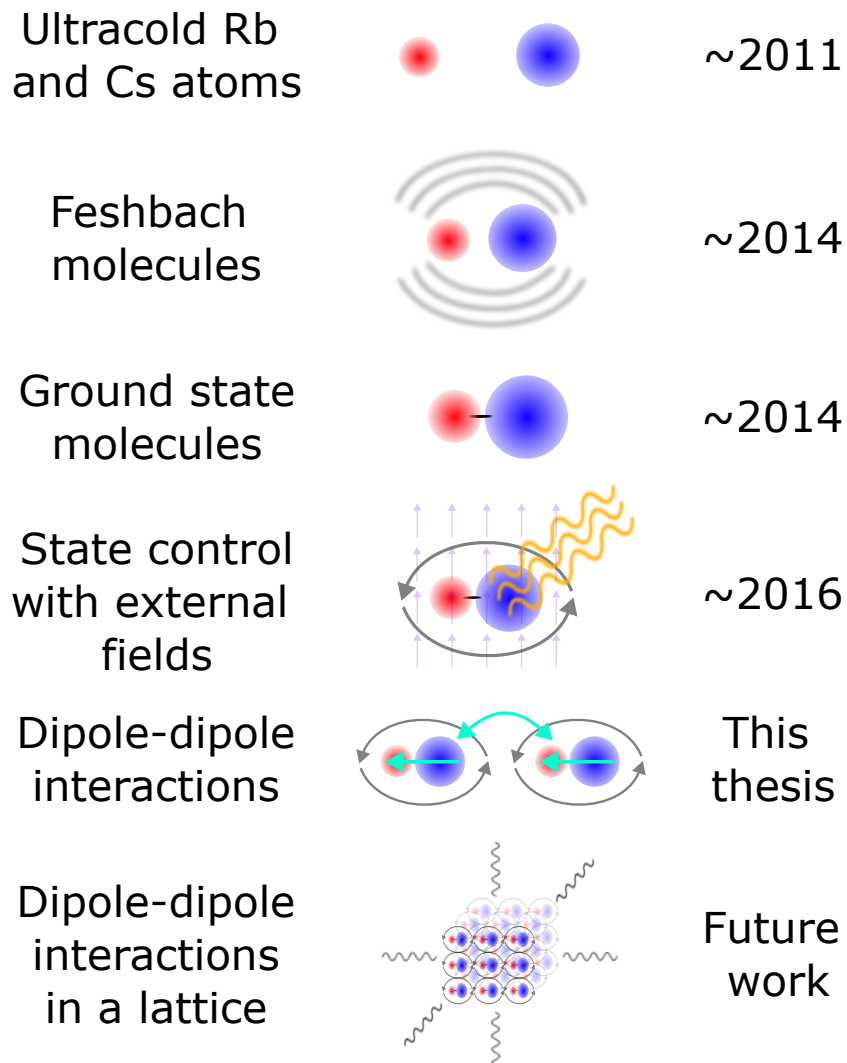


**Figure 1.4:** Overview of the steps to observing dipole-dipole interactions between ultracold RbCs molecules in the lab and when each of the steps was established at Durham University. First, we produce an ultracold mixture of Rb and Cs atoms [107–109]. Next, we ramp the magnetic field over an interspecies Feshbach resonance, creating weakly-bound Feshbach molecules [110–112]. We then transfer the Feshbach molecules to their electronic and rovibrational ground state using STIRAP [113–116]. Using external fields, we manipulate the internal states of the molecules, presenting a rich energy landscape that can be used as the foundation for quantum science [49, 101, 117–120]. By engineering long-coherence times between different rotational quantum states, we observe dipolar interactions in our sample [121]. In the future, the immediate plan will be to confine molecules in an optical lattice potential and begin to simulate tunable lattice-spin models.

## 1.5 Thesis overview

This thesis is structured as follows:

In chapter 2, we introduce the theoretical background necessary for understanding the results presented in this thesis. We begin by outlining the structure of RbCs molecules. We then describe the interactions between RbCs molecules and external fields, before giving a brief insight into how utilising these interactions can lead to engineering tunable many-body Hamiltonians.

Chapter 3 concentrates on the details of the experimental setup. We summarise the methods we employ in creating ultracold ground state RbCs molecules in the laboratory. We discuss recent experimental upgrades, including the replacement of the atomic dispensers and an ion pump. Finally, we detail the installation and characterisation of new microwave antennae.

In chapter 4, we introduce a scheme to produce magic optical traps for different pairs of rotational states of RbCs using light tuned close to an electronic transition. We conduct a comprehensive investigation into the low-lying vibrational, rotational and hyperfine structure of the excited state potential. Next, we identify the laser detunings required for producing rotationally magic traps before performing Ramsey experiments near the magic wavelength, demonstrating its prospects for engineering long quantum coherence times between different rotational states of RbCs.

In chapter 5, we prove the efficacy of the magic trapping protocol investigated in chapter 4 by trapping our molecular sample and performing a series of Ramsey experiments. We present world-record coherence times between different rotational states of diatomic polar molecules. These long coherence times facilitate the observation of dipolar interactions in our bulk gas. We coarsely tune the strength of the interactions in our sample by initialising our molecules in different superpositions of rotational states.

In chapter 6, we explore a route for creating ground state RbCs that is compatible with a method for producing a low-entropy sample of RbCs molecules in an optical lattice, demonstrated by researchers at the University of Innsbruck. We associate atoms into molecules using a Feshbach resonance at a magnetic field different to our typical experimental procedure before presenting a method of accessing a near-threshold bound state suitable for transferring to the ground state via STIRAP. We then directly measure the

---

diagonal and off-diagonal elements of the STIRAP Hamiltonian by performing spectroscopy and Rabi oscillations on the relevant transitions.

Chapter 7 focuses on utilising different rotational states of RbCs as a synthetic dimension landscape. By coupling different rotational states simultaneously, we engineer Hamiltonians analogous to single-particle dynamics in a one-dimensional optical lattice potential.

# List of Publications

The following publications were completed during the course of this work:

- [122] P. D. Gregory, J. A. Blackmore, M. D. Frye Matthew, L. M. Fernley, S. L. Bromley, J. M. Hutson and S. L. Cornish, *Molecule-molecule and atom-molecule collisions with ultracold RbCs molecules*, New J. Phys. **23** 125004, 2021
- [123] A. Das, P. D. Gregory, T. Takekoshi, L. Fernley, M. Landini, J. M. Hutson, S. L. Cornish, H-C. Nägerl, *An association sequence suitable for producing ground-state RbCs molecules in optical lattices*, SciPost Phys. **15**, 220 (2023)
- [121] P. D. Gregory, L. M. Fernley, A. L. Tao, S. L. Bromley, J. Stepp, Z. Zhang, S. Kotochigova, K. R.A. Hazzard, S. L. Cornish, *Second-scale rotational coherence and dipolar interactions in a gas of ultracold polar molecules*, Nature Physics volume **20**, 415-421 (2024)
- *In preparation*, L. M. Fernley, P. D. Gregory, A. L. Tao, S. L. Bromley, A. Das, F. V. Gierke, S. Kotochigova, and S. L. Cornish, *High-resolution spectroscopy of the lowest electronically excited state of  $^{87}\text{Rb}^{133}\text{Cs}$  for the engineering of rotationally-magic wavelength optical traps*

# Chapter 2

## Theoretical Background

### 2.1 Introduction

In this chapter, we will provide an overview of the theoretical framework that underpins the results presented in this thesis. Many of the concepts discussed herein apply not only to RbCs molecules but also to the structure and interactions of other diatomic molecules. We will begin by presenting a comprehensive description of the relevant structure of RbCs, arranged according to progressively lower energy scales. We will then describe the state-sensitive interactions of RbCs with external electromagnetic (EM) fields and using EM fields to access different rotational and hyperfine states. Finally, we will discuss the interactions between molecules through their electric dipole moments.

### 2.2 Structure of RbCs

A chief benefit to utilising diatomic molecules as a platform for quantum computation and simulation lies in their rich internal quantum structure. Unlike atoms, molecules possess not only electronic and hyperfine internal degrees of freedom contributing to the energy of a given state but also degrees of freedom associated with vibration and rotation. The Hamiltonian describing the internal energy of a given molecular state is

$$\hat{H}_{\text{Int}} = \hat{H}_{\text{Electronic}} + \hat{H}_{\text{Vibrational}} + \hat{H}_{\text{Rotational}} + \hat{H}_{\text{HF}}, \quad (2.1)$$

where  $\hat{H}_{\text{Electronic}}$ ,  $\hat{H}_{\text{Vibrational}}$ ,  $\hat{H}_{\text{Rotational}}$  and  $\hat{H}_{\text{HF}}$  are the terms relating to electronic, vibrational, rotational and hyperfine degrees of freedom and typically contribute on the order of  $\sim 100$  THz,  $\sim 1.5$  THz,  $\sim$ GHz and  $\sim$ MHz to the overall energy of a state respectively.

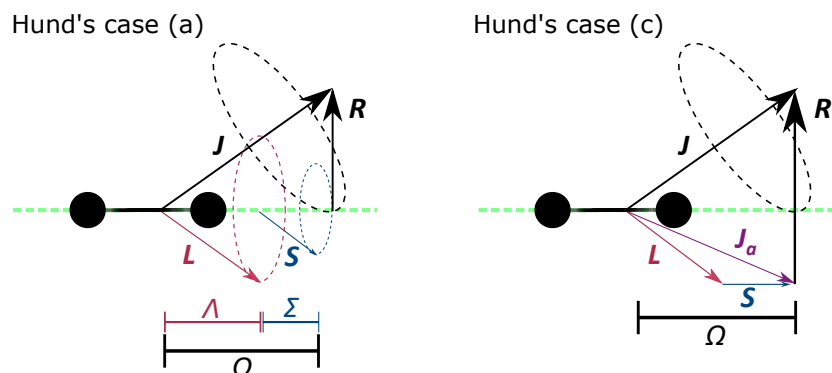


Figure 2.1: Hund's cases (a) and (c).

### 2.2.1 Quantum numbers for diatomic molecules

Dissecting the energy level structure of diatomic molecules is initially addressed by defining a set of good quantum numbers used to describe our states. Good quantum numbers are determined by which of Hund's cases is appropriate to describe the coupling of the angular momenta of the molecule. The relevant Hund's cases for RbCs are (a) and (c), presented in Fig. 2.1. Angular momenta quantum numbers used in Hund's cases are [124]:

- $L$ : the total electronic orbital angular momentum,  $L = l_{\text{Rb}} + l_{\text{Cs}}$
- $S$ : the total electron spin angular momentum,  $S = s_{\text{Rb}} + s_{\text{Cs}}$
- $J$ : the total angular momentum,  $J = L + S + R$
- $R$ : the rotational angular momentum of the nuclei
- $N$ : the total angular momentum excluding spin,  $N = J - S$ <sup>1</sup>
- $I$ : the total nuclear spin angular momenta,  $I = i_{\text{Rb}} + i_{\text{Cs}}$ .

Hund's cases are adopted in accordance with the relative coupling strength of  $L$  coupling to the internuclear axis via electrostatic forces, the coupling of the orbital and spin angular momenta ( $L$  and  $S$ ) and the coupling of  $L$  and  $S$  to the total angular momentum  $J$  [125]. In both instances, (a) and (c), the coupling of  $L$  and  $S$  to  $J$  is relatively weak, allowing  $J$  to serve as a good quantum number.

Hund's case (a) asserts that the orbital angular momentum,  $L$ , is strongly coupled to the internuclear axis, while the coupling of  $L$  and  $S$  is weak in

<sup>1</sup>For the ground state  $N = J$ .

comparison. This weak coupling enables the projections of  $L$  and  $S$  with respect to the internuclear axis to be well-defined and are denoted as  $\Lambda$  and  $\Sigma$  respectively. Their summation is given the label  $\Omega$ . In this case, the vector  $\boldsymbol{\Omega}$  points along the internuclear axis, with magnitude  $\Omega$ , combines with  $\boldsymbol{R}$  to give  $\boldsymbol{J}$ . Additionally,  $\boldsymbol{I}$  couples to  $\boldsymbol{J}$  resulting in a new quantum number describing the total angular momenta  $F$ .

In Hund's case (c), the coupling between  $L$  and  $S$  is stronger than the coupling between  $L$  and the internuclear axis. Therefore, it's useful to define a new quantum number  $\boldsymbol{J}_a$  which is the vectorial sum of the total orbital and spin angular momenta,  $\boldsymbol{J}_a = \boldsymbol{L} + \boldsymbol{S}$ . The projection of  $\boldsymbol{J}_a$  onto the internuclear axis defines  $\boldsymbol{\Omega}$ .  $\boldsymbol{\Omega}$  then couples with  $\boldsymbol{R}$  to form  $\boldsymbol{J}$ .

Hund's case (a) has good quantum numbers  $S, \Sigma, \Lambda, \Omega, J, I$  and  $F$ . This case is typically applicable for describing low-lying  $J$  states [126]. Hund's case (c) features good quantum numbers  $J_a, \Omega$  and  $J$  and is used to describe states of large nuclear separations.

The electronic potentials for Rb and Cs interactions arise from the interplay between repulsive Coulomb forces, attractive Van der Waals forces and short-range chemical bonding effects. Coulomb interaction varies as  $R^{-12}$  whereas the Van der Waals interaction varies as  $R^{-6}$ , resulting in a characteristic Lennard-Jones potential shape where  $R$  is the distance separating the two nuclei [127] as shown in 2.2(a). At short interatomic distances, repulsive coulomb interaction dominates, causing a rapid increase in potential energy as  $R$  tends to zero. At large interatomic distances however, the potential tends towards the free atom energy as  $R$  tends to  $\infty$ . Between these two extremes, if a minimum can be found with sufficient depth, bound molecular states can be supported. The ground electronic state potential supports  $\sim 120$  vibrational states [128].

The term symbols used to denote electronic states take the form  $n^{(2S+1)}\Lambda_{\Omega}^{\pm}$ . Here,  $n$  denotes the relative energies of potentials and is represented by a letter. Beginning from the ground state and proceeding in order of ascending energy  $n$  is X, A, B, C etc <sup>2</sup>.  $n$  symbols in upper case and lower case refer to singlet and triplet states respectively. The quantum number  $\Lambda$  is represented using capital Greek letters  $\Sigma, \Pi, \Delta$  for  $\Lambda = 0, 1, 2$  etc.  $\Omega$  is only specified when necessary to distinguish between different values of

<sup>2</sup>Although, this convention is sometimes broken.  $n$  is defined with respect to discovered states at the time.

$L$ .  $\pm$  refers to reflection symmetry in a plane containing the internuclear axis.

We typically couple to three electronic energy states in our experiment:  $a^3\Sigma$  where our Feshbach state lies;  $b^3\Pi$  which we utilise to access an intermediate excited state to facilitate STIRAP transfer; and  $X^1\Sigma^+$  which is the electronic ground state.  $b^3\Pi$  is also used to engineer magic wavelength traps which is discussed in detail in later chapters. We use “primes” to denote quantum numbers of particular states as shorthand. For example,  $v$ ,  $v'$  and  $v''$  are the vibrational quantum numbers of the Feshbach, excited and ground states respectively. Coupling between  $b^3\Pi$  and  $X^1\Sigma^+$  is forbidden due to selection rules, however it is weakly allowed due to the existence of spin-orbit coupling causing mixing between the  $b^3\Pi^+$  and  $A^1\Sigma^+$  states [129, 130].

## 2.2.2 Vibrational structure

At energies near the bottom of the electronic potential, the potential appears approximately harmonic. Therefore, an appropriate estimation of the energy level splitting can be obtained by treating the system as a quantum harmonic oscillator [131]. Energies of vibrational states are therefore given by

$$E_v = \hbar\omega_v \left( v + \frac{1}{2} \right), \quad (2.2)$$

where  $\hbar$  is the reduced Planck’s constant,  $\omega_v$  is the vibrational angular frequency of state  $v$ . Consequently, vibrational state wavefunctions are described by Hermite polynomials as presented in Fig. 2.2(b). The energy difference between  $v'' = 0$  and  $v'' = 1$  in RbCs is  $h \times 1.49270$  THz [128]. In electronic transition, there is no selection rule purely regarding change of vibrational quantum numbers. Transition strength is instead governed through arguments related to Frank-Condon overlapping of the relevant wavefunctions combined with rotational transition dipole moment calculations [132–134].

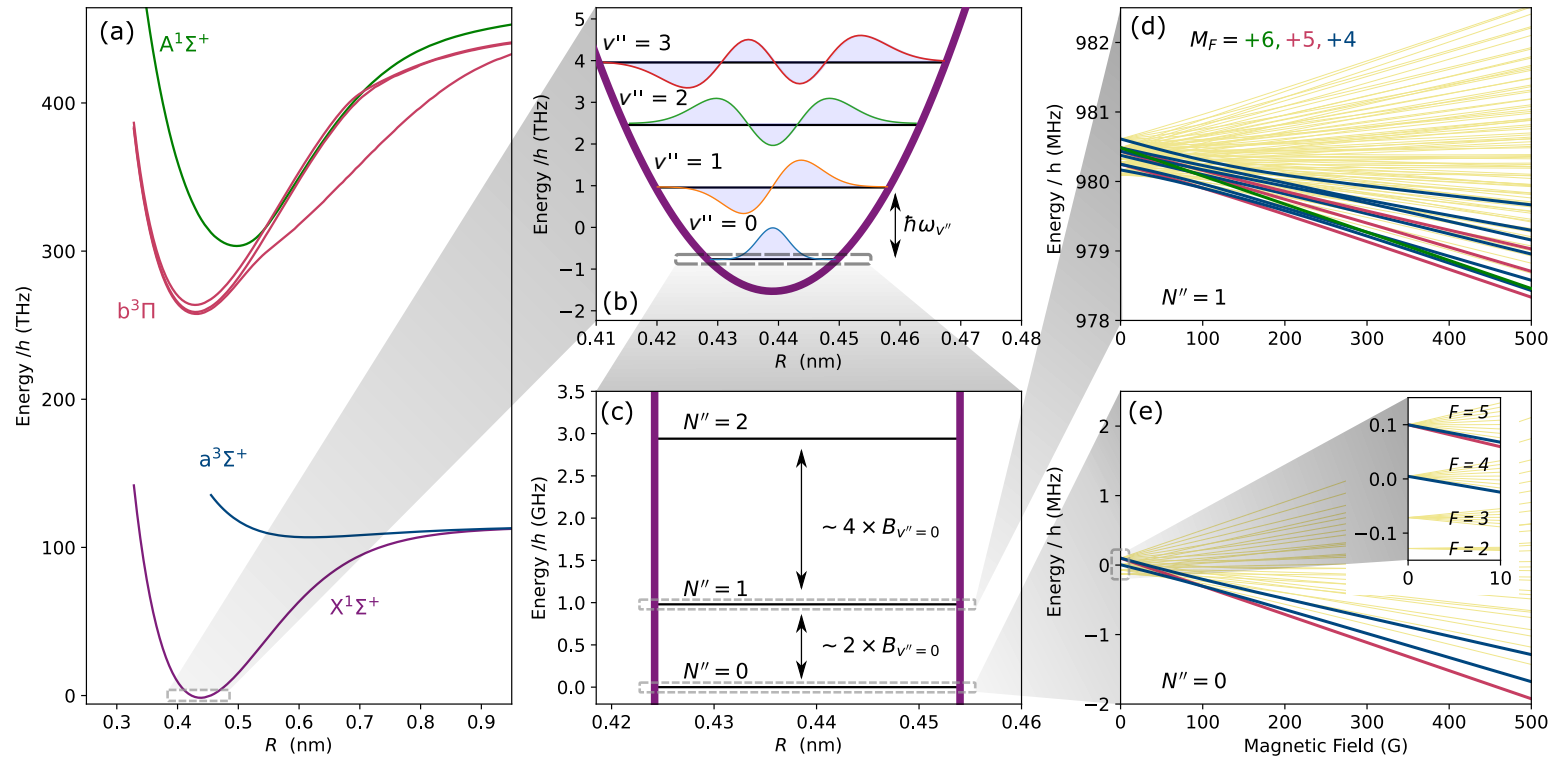


**Figure 2.2:** Overview of RbCs structure at various energy scales. (a) Relevant molecular potentials of RbCs based on calculations found in [135]. (b) Vibrational splitting of  $X^1\Sigma^+$  potential. Hermite wavefunctions for each vibrational state are illustrated. (c) Rotational splitting of  $X^1\Sigma^+(v''=0)$ . (d) and (e) Zeeman structure of  $N=0$  and  $N=1$  rotational energy levels respectively. States with  $M_F = +6, +5$  and  $+4$  labelled with green, red and blue colours respectively. Inset in (e) shows the hyperfine splitting at low magnetic fields for  $N=0$ .

### 2.2.3 Rotational structure

Diatomic molecules can be modelled as two masses separated by an effective distance  $r$ . This is known as the “rigid rotor” model. By examining the associated kinetic energy, given the symmetry about the internuclear axis, we arrive at rotational energies given by

$$E_{\text{Rigid}}(N) = B_v N(N + 1), \quad (2.3)$$

where  $N$  is the rotational quantum number and  $B_v$  is the rotational constant of a given vibrational state. The ground vibrational states in RbCs have a rotational constant of  $B_{v''=0} = 490.173\,994(45)$  MHz [136].

However, molecules are not entirely rigid. As we consider higher rotational energy states, centrifugal distortion effects begin to have a non-negligible influence on the rotational energies. To account for centrifugal distortion, we introduce a correction term, resulting in rotational energies are given by

$$E_{\text{Rot}}(N) = B_v N(N + 1) - D_v N^2(N + 1)^2, \quad (2.4)$$

where  $D_v$  denotes the centrifugal distortion term. For low-lying rotational states of the vibrational ground state, centrifugal corrections are on the order of hundreds of Hz [137].

The rigid rotor model supports wavefunctions described by spherical harmonics [138]:

$$\psi_{R,N,M_N} = A_R e^{-iM_N\phi} P_N^{M_N}(\cos\theta) = Y_{N,M_N}(\theta, \phi), \quad (2.5)$$

where  $R$  is an index relating to the appropriate normalisation constant,  $A$ ,  $M_N$  is the projection of  $N$  onto the quantisation axis,  $P$  denotes the associated Legendre polynomial and  $Y$  is the symbol for spherical harmonics.

An important feature of rotational states is made evident by Eq. 2.4. Rotational energy levels are anharmonically spaced, illustrated in Fig. 2.2(c). This allows us to experimentally address the coupling between two pairs of rotational states independently with ease.

### 2.2.4 Hyperfine structure

The finest energy contribution to the overall Hamiltonian in RbCs originates from the interactions of nuclear spins.  $^{87}\text{Rb}$  and  $^{133}\text{Cs}$  possess nuclear spin

magnitudes  $I_{\text{Rb}}=3/2$  and  $I_{\text{Cs}}=7/2$  respectively. We can define a hyperfine Hamiltonian as [124, 136, 139, 140]

$$\begin{aligned} \hat{H}_{\text{HF}} = & \sum_{i=\text{Rb,Cs}} \mathbf{V}_i \cdot \mathbf{Q}_i + \sum_{i=\text{Rb,Cs}} c_i \mathbf{N} \cdot \mathbf{I}_i \\ & + c_3 \mathbf{I}_{\text{Rb}} \cdot \mathbf{T} \cdot \mathbf{I}_{\text{Cs}} + c_4 \mathbf{I}_{\text{Rb}} \cdot \mathbf{I}_{\text{Cs}}. \end{aligned} \quad (2.6)$$

The first term results from the interaction between the nuclear quadrupole,  $\mathbf{Q}_i$ , with the electric-field gradient caused by electron distribution,  $\mathbf{V}_i$ , for each nucleus. The second term relates to the coupling between nuclear spins and the magnetic field produced by the rotation of the molecule. The third and fourth terms correspond to tensor and scalar interactions between the nuclear spins of each atom respectively.

For the rotational ground state of RbCs, the first two terms are zero and  $c_3$  is a factor of  $\sim 100$  smaller than  $c_4$ . As illustrated in the inset of Fig. 2.2(e), in the absence of external fields, we observe 4 distinct manifolds corresponding to  $F = 2, 3, 4$  and 5. These are separated by factors of  $c_4$ .

Hyperfine interactions split rotational manifolds into  $(2N + 1)(2i_{\text{Rb}} + 1)(2i_{\text{Cs}} + 1)$  energy levels leading to 32 states in  $N = 0$ , 96 in  $N = 1$  etc. This splitting becomes apparent in the presence of external fields as shown in Fig. 2.2(d) and (e).

In this work, molecular energies for  $X^1\Sigma^+$  states are calculated by diagonalising an “effective” Hamiltonian which only includes rotational, hyperfine and external field contributions. We use [141, 142] in our calculations.

## 2.3 RbCs state control

It’s important to understand the interactions of the molecule with external fields and with each other. In the presence of external fields, an absolute Hamiltonian describing the energies of RbCs can be formed with the addition of an external term to Eq. 2.1:

$$\hat{H}_{\text{Tot}} = \hat{H}_{\text{Int}} + \hat{H}_{\text{Ext}}. \quad (2.7)$$

In this section, we provide a brief overview of the external field interactions that are relevant to our experiment.

### 2.3.1 Zeeman effect

The magnetic moment associated with RbCs arises solely from the contributions of nuclear spin magnetic moments. By virtue of Rb and Cs being alkali atoms, the outermost electrons in the two nuclei are paired, resulting in no contribution to the overall magnetic moment. The RbCs molecular magnetic moment is therefore on the order of  $\mu_N/\mu_B$  smaller than their individual atomic counterparts. The Zeeman Hamiltonian is defined as

$$\hat{H}_{\text{Zeeman}} = -g_r \mu_N \mathbf{N} \cdot \mathbf{B} - \sum_{i=\text{Rb,Cs}} g_i (1 - \sigma_i) \mu_N \mathbf{I}_i \cdot \mathbf{B}, \quad (2.8)$$

where  $g_r$  is the rotational g-factor of the molecule and  $g_i$  is the rotational g-factor of each atom ( $i = \text{Rb, Cs}$ ).  $\sigma_i$  denotes the nuclear shielding factor of the atom. Zeeman shifts in molecular states are presented in Fig. 2.2 (d) and (e).

Our experiments typically operate at 181.5 G. In this “mid” magnetic field regime, nuclear spins are not well-defined. Instead, there is mixing between states of different nuclear spin. This ultimately leads to our general labelling convention used throughout this work of  $(N, M_F)_k$  where  $M_F$  is the projection of the total angular momentum onto the quantisation axis,  $M_F = M_N + m_{I_{\text{Rb}}} + m_{I_{\text{Cs}}}$ , and  $k$  is an index counting up in increasing energy.  $k$  is omitted for nuclear spin-stretched states.

### 2.3.2 ac Stark effect in RbCs

Interactions of atoms or molecules with a time-varying electric field, for instance off-resonant light, generate perturbations in their respective energy level structure given by the equation

$$\hat{H}_{\text{AC}} = -\frac{\boldsymbol{\alpha} \cdot \mathbf{I}}{2\epsilon_0 c}, \quad (2.9)$$

where  $c$  is the speed of light,  $\epsilon_0$  is the vacuum permittivity,  $\boldsymbol{\alpha}$  is the polarisability and  $I$  is the intensity of the field experienced by the atom or molecule.

Unlike atoms, the anisotropy of diatomic molecules leads to molecules having two polarisabilities associated with them. The polarisability parallel to the internuclear axis,  $\alpha_{\parallel}$  and the one orthogonal to the internuclear axis,  $\alpha_{\perp}$ . It's therefore helpful to adopt a coordinate system that defines the polarisability of the molecule with respect to these axes, shown in Fig 2.3.

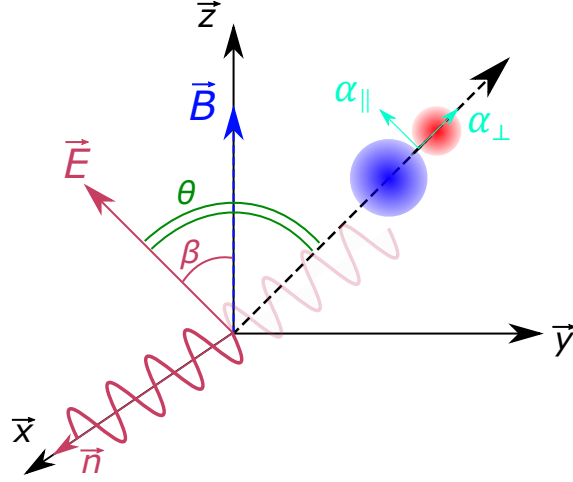


**Figure 2.3:** Coordinate system for describing ac Stark shifts in RbCs. A light wave propagating along  $\vec{n}$  with an electric field vector,  $\vec{E}$ , orthogonal to the direction of propagation.  $\vec{E}$  is at an angle  $\beta$  with respect to the quantisation axis provided by the magnetic field,  $\vec{B}$ , and  $\theta$  with respect to the internuclear axis.

Using the basis of  $\vec{a}$ ,  $\vec{b}$  and  $\vec{c}$ , where  $\vec{c}$  is the vector parallel to the internuclear axis and  $\vec{a}$  and  $\vec{b}$  are vectors orthogonal to this, we can construct a vector polarisability matrix,

$$\boldsymbol{\alpha} = \begin{pmatrix} \alpha_{\perp} & 0 & 0 \\ 0 & \alpha_{\perp} & 0 \\ 0 & 0 & \alpha_{\parallel} \end{pmatrix}. \quad (2.10)$$

The intensity of a Gaussian beam is given by

$$I = \frac{c\epsilon_0 n}{2} |\vec{E}|^2, \quad (2.11)$$

where  $n$  is the refractive index of the material the light is propagating through. Using our molecular coordinates, we can define a vector associated with the electric field of the propagating light,

$$\vec{E} = E \begin{pmatrix} 0 \\ \sin \theta \\ \cos \theta \end{pmatrix}. \quad (2.12)$$

We can rewrite Eq. 2.9 using 2.10, 2.11 and 2.12 as

$$\hat{H}_{AC} = -\frac{I}{2\epsilon_0 c} [\alpha_{\parallel} \cos^2 \theta + \alpha_{\perp} \sin^2 \theta]. \quad (2.13)$$

Here we have set  $n = 1$ . It is often useful to separate contributions to the overall polarisability into their isotropic and anisotropic components. We hence rewrite Eq. 2.13 as

$$\hat{H}_{AC} = -\frac{I}{2\epsilon_0 c} [\alpha^{(0)} + \alpha^{(2)} P_2(\cos \theta)], \quad (2.14)$$

where  $P_2$  is the second Legendre polynomial.  $\alpha^{(0)}$  is termed the ‘*isotropic*’ polarisability and is the same for all rotational energy levels,  $N$ , and  $\alpha^{(2)}$  is the ‘*anisotropic*’ polarisability and is, in general, different for different values of  $N$ . These polarisabilities are given the forms:

$$\alpha^{(0)} = \frac{1}{3} (\alpha_{\parallel} + 2\alpha_{\perp}) \quad (2.15)$$

$$\alpha^{(2)} = \frac{2}{3} (\alpha_{\parallel} - \alpha_{\perp}). \quad (2.16)$$

Let’s now apply this perturbation to a molecular state. We apply light linearly polarised with a propagation vector  $\vec{n}$  parallel to  $\vec{x}$  at an angle  $\beta$  to the magnetic field. We find the matrix elements of this perturbation become [143]

$$\begin{aligned} & \langle N', M'_N | I\alpha | N, M_N \rangle \\ &= I\alpha^{(0)} \delta_{NN'} \delta_{M_N M'_N} \\ &+ I\alpha^{(2)} \sum_M d_{M0}^2(\beta) (-1)^{M'_N} \sqrt{(2N+1)(2N'+1)} \\ &\times \begin{pmatrix} N' & 2 & N \\ 0 & 0 & 0 \end{pmatrix} \begin{pmatrix} N' & 2 & N \\ -M'_N & M & M_N \end{pmatrix}, \end{aligned} \quad (2.17)$$

where  $d_{M0}(\beta)$  is the reduced Wigner-D matrix rotating the polarisability tensor by the angle  $\beta$ ,  $M_N$  is the projection of  $N$  along the quantisation axis and terms in two-rowed parentheses are Wigner-3j symbols.

The form of Eq. 2.17 presents an important phenomenon. Matrix elements with  $|N' - N| \neq 0, 2$  or  $|M'_N - M_N| > 2$  do not feature any contribution from the second term in Eq. 2.17, therefore each  $M_N$  projection is perturbed in energy equally. However, for  $N = N' = 1$ , the matrix elements do have a contribution from the second term. This can be interpreted as the anisotropic component of the polarisability,  $\alpha^{(2)}$ , mixing different projections of  $M_N$ . We can show this explicitly by presenting the form of Eq. 2.17 for the case where  $N = 1$  with basis  $M_N = 0, +1, -1$ :

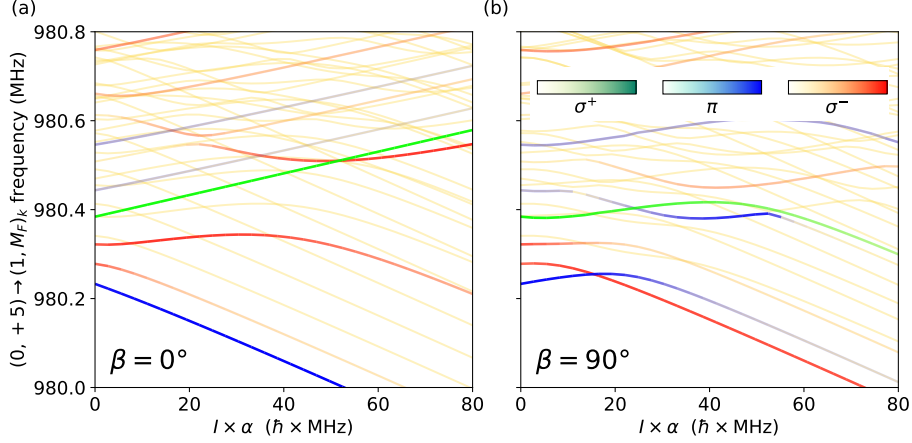


**Figure 2.4:** ac Stark shifts in  $N = 1$  RbCs interacting with a linearly polarised oscillating electric field for light polarised (a) parallel and (b) orthogonal with respect to the quantisation axis. States coloured by the transition dipole moment (TDM) magnitude coupling from the  $(0, +5)$  ground state with  $\sigma^+$ ,  $\pi$  and  $\sigma^-$  transitions that correspond to  $\Delta M_F = 1, 0$  and  $-1$  being coloured green, blue and red respectively.

$$\langle 1, M'_N | I\alpha | 1, M_N \rangle = I\alpha^{(0)} + \frac{I\alpha^{(2)}}{5} \begin{pmatrix} 2P_2(\cos \beta) & -\frac{3}{\sqrt{2}} \sin \beta \cos \beta & +\frac{3}{\sqrt{2}} \sin \beta \cos \beta \\ -\frac{3}{\sqrt{2}} \sin \beta \cos \beta & -P_2(\cos \beta) & \frac{3}{2} \sin^2 \beta \\ +\frac{3}{\sqrt{2}} \sin \beta \cos \beta & \frac{3}{2} \sin^2 \beta & -P_2(\cos \beta) \end{pmatrix}. \quad (2.18)$$

The ac Stark shifts in RbCs for  $N = 1$  states in the presence of light polarised parallel and orthogonal to the quantisation axis is presented in Fig. 2.4. We can see from Eq. 2.18 that another important result is evident, the diagonal terms associated with mixing  $M_N = 0$  is twice that and the opposite sign of  $M_N = \pm 1$ . This means that ac Stark shifts associated with coupling states with the same  $M_N$  are twice the magnitude as for  $\Delta M_N = \pm 1$ .

### 2.3.3 Coupling rotational states

Different rotational states are accessed in RbCs by driving electronic transitions with microwaves. At 181.5 G, we operate in a regime where nuclear spins are sufficiently coupled and  $M_F$  is a good quantum number. Electric transition dipole moments are calculated in the  $|N, M_N\rangle$  basis to be

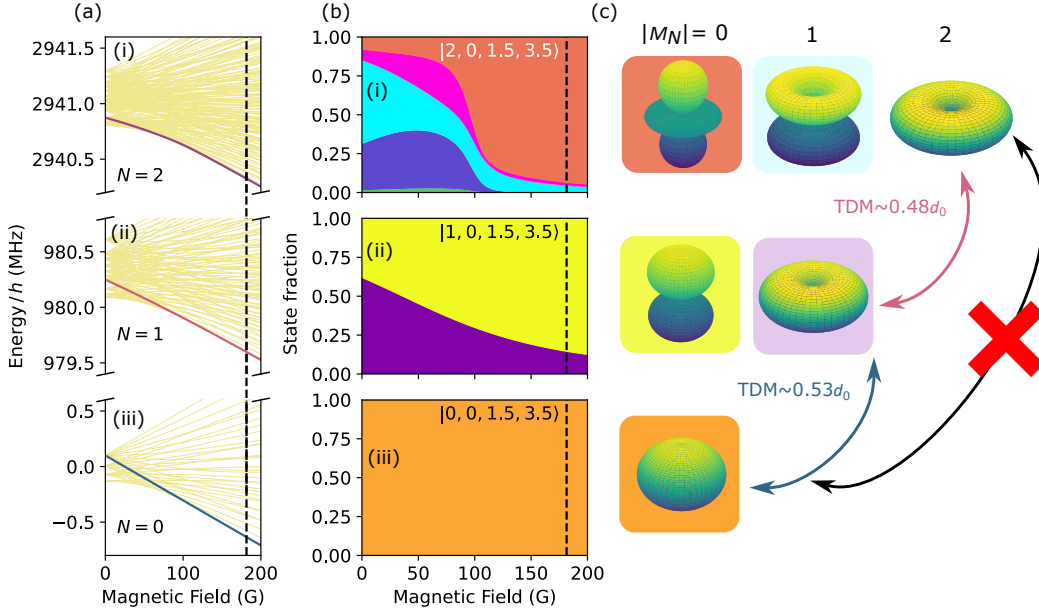


**Figure 2.5:** Rotational coupling in RbCs. (a) Zeeman structure of (i)  $N = 2$ , (ii)  $N = 1$  and (iii)  $N = 0$  rotational states. A magnetic field of 181.5 G is indicated with the vertical dashed line. States highlighted in blue, red and purple correspond to  $(0, +5)$ ,  $(1, +5)_0$  and  $(2, +5)_0$  respectively. (b) State compositions as a function of magnetic field for the coloured states in (a) for (i)  $N = 2$ , (ii)  $N = 1$  and (iii)  $N = 0$ . The colours in the plots correspond to the magnitude of the components of the nuclear spin states of the state coloured in (a). The dominant character at 181.5 G is presented in the plot in the  $|N, M_N, m_{\text{Rb}}, m_{\text{Cs}}\rangle$  basis. Code adapted from Tom Hepworth's MSci project [142, 144]. (c) Spherical harmonic wavefunctions for different values of  $|M_N|$ . The transition dipole moments for  $(0, +5) \rightarrow (1, +5)_0$  and  $(1, +5)_0 \rightarrow (2, +5)_0$  at 181.5 G given in blue and red respectively. Transitions of  $\Delta N > 1$  are forbidden. Wavefunction compositions for each  $N$  state are represented by the opacity of the squares surrounding the relative wavefunctions.

$$d = d_0 \sqrt{(2N+1)(2N'+1)} (-1)^{M_N} \begin{pmatrix} N & 1 & N' \\ -M_N & M & M'_N \end{pmatrix} \begin{pmatrix} N & 1 & N' \\ 0 & 0 & 0 \end{pmatrix}, \quad (2.19)$$

where  $d_0$  is the molecular frame dipole moment (1.225 D [145, 146],  $\text{D} \sim 3.34 \times 10^{-30} \text{ C m}$ ).  $M = M_N - M'_N = -1, 0$  and  $+1$  which correspond to  $\sigma^+$ ,  $\pi$  and  $\sigma^-$  transitions respectively.

An important aspect of rotational transitional dipole moments is made evident from Eq. 2.19. If  $N = N'$ , the transition dipole moment is zero. Pure

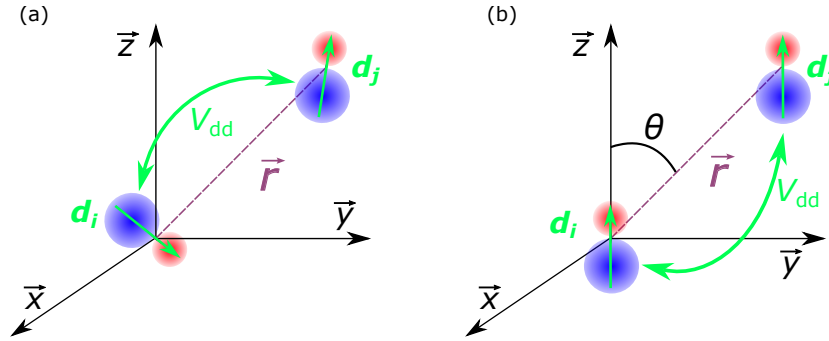


**Figure 2.6:** Dipole-dipole interactions. (a) Dipoles orientated arbitrarily and (b) dipoles aligned along a common axis. The moment of dipole  $i$  ( $j$ ) is given by  $\mathbf{d}_i$  ( $\mathbf{d}_j$ ),  $\vec{r}$  is the vector connecting the two dipoles with magnitude  $r$ ,  $V_{dd}$  is the dipole-dipole interaction energy and  $\theta$  is the angle between the quantisation axis in the  $\vec{z}$  direction and  $\vec{r}$ .

$N$  states possess no dipole moment. To realise dipole moments in the lab frame, a mixture of states with opposing parities is necessary. This breaks the symmetry of the spherical harmonic wavefunctions. The transition dipole moment for  $N = 0 \rightarrow N = 1$  states is  $d_0/\sqrt{3}$ .

Selection rules for rotational transitions are  $\Delta N = \pm 1$  and  $\Delta M_F = 0, \pm 1$ . As illustrated in Fig. 2.5(b), states with non-nuclear-spin-stretched projections are a mixture of different nuclear spin states. Transitions with  $\Delta M_F = 0, +1$  and  $-1$  are given the names  $\pi$ ,  $\sigma^+$  and  $\sigma^-$  respectively.

### 2.3.4 Dipole-dipole interactions

Consider two dipoles situated in arbitrary positions and orientations in space as shown in Fig. 5.8(a). The dipole-dipole interaction energy is then given by [17, 18]

$$V_{dd} = \frac{(\mathbf{d}_i \cdot \mathbf{d}_j) r^2 - 3(\mathbf{d}_i \cdot \mathbf{r})(\mathbf{d}_j \cdot \mathbf{r})}{r^5}, \quad (2.20)$$

where  $\mathbf{d}_i$  ( $\mathbf{d}_j$ ) is the dipole moment of the  $i^{\text{th}}$  ( $j^{\text{th}}$ ) dipole and  $\mathbf{r}$  is the vector connecting the two dipoles with magnitude  $r$ .

$N$  and  $M_N$  define the spherical harmonic wavefunction of a given state as illustrated in Fig. 2.5(c).  $M_N$  is given with respect to a quantisation axis. Therefore, we consider the case where interacting dipoles are aligned along the quantisation axis, shown in Fig. 5.8(b). This simplifies Eq. 2.20 to

$$V_{dd} = \frac{(\mathbf{d}_i \cdot \mathbf{d}_j)(1 - 3 \cos^2 \theta)}{r^3}, \quad (2.21)$$

where  $\theta$  is the angle between the quantisation axis and  $\mathbf{r}$ . Eq. 2.21 presents two important attributes about dipole-dipole interactions, their relatively long-range ( $\propto 1/r^3$ ) and anisotropic character (dependence on  $\theta$ ). Typical dipole-dipole interaction strengths for diatomic molecules with separation distances achievable in optical tweezers ( $\sim 1 \mu\text{m}$ ) are on the order of kHz [97].

For two molecules in equal superpositions of states, the dipole-dipole interaction energy is [36, 121, 147, 148]

$$V_{dd} = \frac{1 - 3 \cos^2 \theta}{r^3} \left( \mathbf{d}_0 \cdot \mathbf{d}_0 + \frac{\mathbf{d}_1 \cdot \mathbf{d}_{-1} + \mathbf{d}_{-1} \cdot \mathbf{d}_1}{2} \right), \quad (2.22)$$

where  $\mathbf{d}_0 = \mathbf{d}_z$ ,  $\mathbf{d}_{\pm 1} = \mp(\mathbf{d}_x \pm i\mathbf{d}_y)/\sqrt{2}$  are the spherical components of the dipole operator. This expression only considers the case where the total change in angular momentum of the molecules is zero.

Considering two molecules labelled  $i$  and  $j$  confined to a common plane, we will briefly discuss how dipole-dipole interactions can be used to encode pseudospins for quantum simulation using the different  $|N, M_N\rangle$  states. We will focus on cases where  $N = 0, 1$  and  $M_N = 0, \pm 1$  for simplicity.

We can map our  $|N, M_N\rangle$  states onto spins as  $\{|\downarrow\rangle, |\uparrow\rangle\} = \{|0, 0\rangle, |1, 0\rangle\}$  or  $\{|\downarrow\rangle, |\uparrow\rangle\} = \{|0, 0\rangle, |1, 1\rangle\}$ . First, let's concentrate on the former.

In this case, only  $\mathbf{d}_0$  components are considered due to selection rules. The dipole-dipole interaction, Eq. 2.22, is described with basis  $|\uparrow_i \uparrow_j\rangle, |\uparrow_i \downarrow_j\rangle, |\downarrow_i \uparrow_j\rangle, |\downarrow_i \downarrow_j\rangle$  as

$$V_{dd} = \frac{1 - 3 \cos^2 \theta}{r^3} \begin{pmatrix} d_{\uparrow}^2 & 0 & 0 & d_{\downarrow\uparrow}^2 \\ 0 & d_{\downarrow}d_{\uparrow} & d_{\downarrow\uparrow}^2 & 0 \\ 0 & d_{\downarrow\uparrow}^2 & d_{\downarrow}d_{\uparrow} & 0 \\ d_{\downarrow\uparrow}^2 & 0 & 0 & d_{\downarrow}^2 \end{pmatrix}, \quad (2.23)$$

where  $d_{\downarrow}, d_{\uparrow}$  are  $\langle 0, 0 | d | 0, 0 \rangle$  and  $\langle 1, 0 | d | 1, 0 \rangle$  respectively. In the absence of external fields, these terms are zero [85, 86]. The other components,  $d_{\downarrow\uparrow}$ , correspond to dipole-dipole interaction facilitated ‘‘flip-flopping’’, exchanging  $|\uparrow\rangle$  and  $|\downarrow\rangle$  states between molecules. The  $d_{\downarrow\uparrow}$  terms in  $|\uparrow_i \uparrow_j\rangle \langle \downarrow_i \downarrow_j|$  and its conjugate are also flip-flops but correspond to a total change in angular

momentum of 2 and are typically far off-resonant.

For the case of  $\{|\downarrow\rangle, |\uparrow\rangle = \{|0, 0\rangle, |1, 1\rangle\}$ , we consider only the  $\mathbf{d}_{\pm 1}$  terms in Eq. 2.22 [84]. Here, we replace  $d_{\uparrow}$  etc terms with  $d_{\tilde{\uparrow}}$ . The dipole-dipole interaction is

$$V_{dd} = \frac{1 - 3 \cos^2 \theta}{r^3} \begin{pmatrix} d_{\tilde{\uparrow}}^2 & 0 & 0 & d_{\downarrow\tilde{\uparrow}}^2 \\ 0 & d_{\downarrow}d_{\tilde{\uparrow}} & -\frac{d_{\downarrow\tilde{\uparrow}}^2}{2} & 0 \\ 0 & -\frac{d_{\downarrow\tilde{\uparrow}}^2}{2} & d_{\downarrow}d_{\tilde{\uparrow}} & 0 \\ d_{\downarrow\tilde{\uparrow}}^2 & 0 & 0 & d_{\downarrow}^2 \end{pmatrix}. \quad (2.24)$$

A few important distinctions between Eq. 2.23 and 2.24 are worth highlighting. The flip-flopping term has a factor of  $-1/2$  difference between the cases. The minus sign is a consequence of the  $(-1)^{M_N}$  coefficient in Eq. 2.19. The factor of a half appears from the fact that only  $\mathbf{d}_1\mathbf{d}_{-1}$  or  $\mathbf{d}_{-1}\mathbf{d}_1$  in Eq. 2.22 acts in the cases of  $|\uparrow_i\downarrow_j\rangle\langle\uparrow_i\downarrow_j|$  and its conjugate. This can be interpreted as the average interaction between dipoles rotating within the plane of confinement as being half as strong as the interaction between dipoles oscillating orthogonal to the plane of confinement.

# Chapter 3

## Experimental Overview and Microwave Control

Work in the bulk gas RbCs laboratory in Durham has spanned decades. The experiment as it stands today is the culmination of the efforts of many generations of undergraduate, PhD and post-doctoral researchers [107, 110, 111, 113, 117, 149–151]. One major benefit of this long history is that new members of the group can promptly delve into cutting-edge physics, given that the experimental groundwork has already been laid. However, long-running experiments naturally lead to their own set of difficulties. The complexity, not to mention the idiosyncrasies that one must get to grips with before being able to run the experiment can be a real challenge. Moreover, with the setup being relatively old compared to other ultracold atomic physics experiments, we decided to undertake major refurbishments which occurred in the last six months of my PhD in order to increase productivity. These refurbishments included the renewal of atomic dispensers and one of the vacuum ion pumps and the addition of an antenna array which were accomplished successfully. In this chapter, we will outline the procedure for producing ultracold ground state RbCs molecules and will outline the crucial components in our experimental setup. We also present results in creating and characterising microwave antennae.

### 3.1 Making ultracold RbCs molecules

#### 3.1.1 Atomic mixtures

Our experiment comprises two vacuum chambers and magneto-optical traps (MOTs). The first, the pyramid MOT, serves as a source of cold  $^{87}\text{Rb}$  and

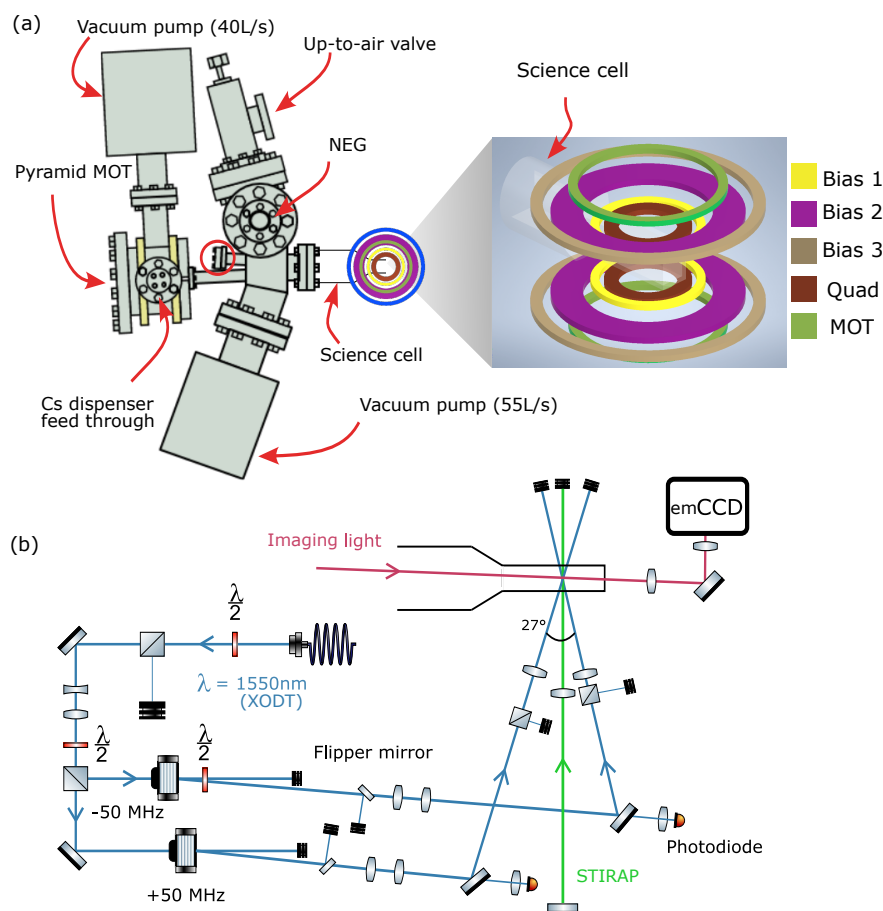


**Figure 3.1:** Experimental setup overview. (a) Vacuum chambers and magnetic field coils. The imaging beam enters the vacuum chamber through the viewport indicated by the red circle. Rb dispenser feed-through on the opposite side of the pyramid chamber (not pictured). (b) Dipole trap and imaging laser setup (MOT beams omitted). STIRAP beam enters using a periscope. Only the final mirror of the periscope is shown.

$^{133}\text{Cs}$  (hereafter Rb and Cs) atoms. These atoms are subsequently captured in the second “science” cell where molecules are created and experiments are conducted. An overview of the vacuum chambers is presented in Fig. 3.1(a)

During experimental operation, current is passed through commercial dispensers (SAES) containing Rb and Cs that reside on the outer edge of the pyramid MOT mirrors via vacuum feed-throughs. This releases atoms into the chamber. The pyramid MOT then cools the atoms and an imbalance in trapping beams forces them through an aperture in the mirrored structure,

creating a beam of cold atoms directed towards our “science cell” (fused silica cell) with internal dimensions of 20 mm by 20 mm by 83 mm and 2 mm thick walls. The cell is not AR coated [149, 150]. The cell is surrounded by copper coils shown in the inset of Fig. 3.1(a), providing magnetic field control.

In the science cell, two conventional MOTs are loaded (one for each species), each comprising 6 counter-propagating laser beams. After the MOT fluorescence has reached a given set point, a compressed-MOT stage begins. We then perform optical molasses cooling on both species before optically pumping each of them into a magnetically trappable state, ( $f_{\text{Rb}} = 1, m_{f_{\text{Rb}}} = -1$ ) and ( $f_{\text{Cs}} = 3, m_{f_{\text{Cs}}} = -3$ ).

Next, both atomic species are loaded into a common magnetic trap. Forced RF evaporation of Rb is performed, while Cs is sympathetically cooled through interspecies elastic collisions with Rb. We then load the atoms into a crossed-optical dipole trap (xODT) by ramping on two 1550 nm beams illustrated in Fig. 3.1(b). Using adiabatic passage facilitated by the addition of an RF-field, we transfer our atoms into their respective hyperfine ground states ( $f_{\text{Rb}} = 1, m_{f_{\text{Rb}}} = +1$ ) and ( $f_{\text{Cs}} = 3, m_{f_{\text{Cs}}} = +3$ ). The xODT intensity is then decreased, allowing the most energetic atoms to escape and reducing the average temperature of the atomic mixture. At this stage, atoms of both species have a temperature of  $\sim 300$  nK and a phase-space density of  $\sim 0.1$  [117].

## 3.2 Feshbach association

We associate Rb and Cs atoms into RbCs molecules by ramping our bias magnetic field over an interspecies Feshbach resonance at 197 G [71, 72], adiabatically following the avoided crossing as illustrated in Fig. 3.2(b).

To associate in the experiment, the magnetic bias field is quickly (on the order of 100  $\mu\text{s}$ ) ramped to  $\sim 217$  G. We then hold for  $\sim 1$  ms to allow the field to stabilise before decreasing to  $\sim 0.4$  G above the 197 G resonance. We perform the association by sweeping our magnetic field at a rate of  $\sim 250$  G/s, forming weakly-bound Feshbach molecules. When labelling molecular bound states near the dissociation threshold, we adopt the notation  $n(f_{\text{Rb}}, f_{\text{Cs}})L(m_{f_{\text{Rb}}}, m_{f_{\text{Cs}}})$  [71]. Here,  $n$  represents the vibrational quantum number counting down from the least-bound state.  $L$  denotes the quantum number associated with the rotational angular momenta of the atoms about the centre-of-mass of the molecule, represented by the letters  $s, p, d$  etc cor-

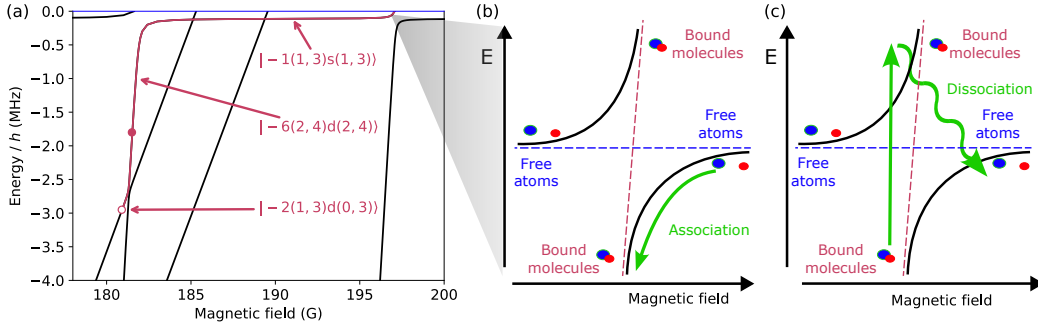


**Figure 3.2:** Magnetic ramp association and dissociation steps. (a) Binding energy of near-threshold bound states for RbCs molecules as a function of magnetic field around 190 G. Binding energy is given relative to the dissociation energy of Rb and Cs in their spin-stretched hyperfine ground state at a given magnetic field. Filled and unfilled red markers denote the locations where STIRAP and Stern-Gerlach separation are performed respectively. (b) Association and (c) dissociation sequence using the Feshbach resonance at 197 G. Note, (b) and (c) are not direct enlargements of a region in (a).

responding to  $L = 0, 1, 2$  etc. The quantum numbers that denote each state are determined through experimental spectroscopy [128]. As presented in Fig. 3.2(a), after association we occupy the  $|-1(1,3)s(1,3)\rangle$  state which runs nearly parallel to the free atomic state with binding energy of 110(2) kHz.

We reduce the magnetic field to occupy the  $|-2(1,3)d(0,3)\rangle$  state following the red path in Fig. 3.2(a). At this point, we exploit the different magnetic-moment-to-mass ratio of atoms and molecules to perform Stern-Gerlach separation. We apply a magnetic field gradient such that the atoms are over-levitated while the molecules are exactly levitated, resulting in non-associated atoms being removed from our trap [152]. Typically  $\sim 8000$  Feshbach molecules are produced in this manner. Over the next  $\sim 20$  ms, the magnetic field gradient is ramped off and the xODT intensity is increased, transferring the molecules to a purely optical trap. We typically lose about half the molecules during this step due to heating. Due to xODT trap geometry, the size of the molecular cloud is  $\sim 30 \mu\text{m}$  by  $\sim 10 \mu\text{m}$ .

To detect our molecular population, we rapidly reverse the magnetic field ramp performed in our association sequence so as not to follow the avoided crossing as illustrated in Fig. 3.2(c). After jumping the avoided crossing, the molecules occupy a state with energy greater than that of the atomic threshold. Consequently, the molecules dissociate into their constituent atoms. We

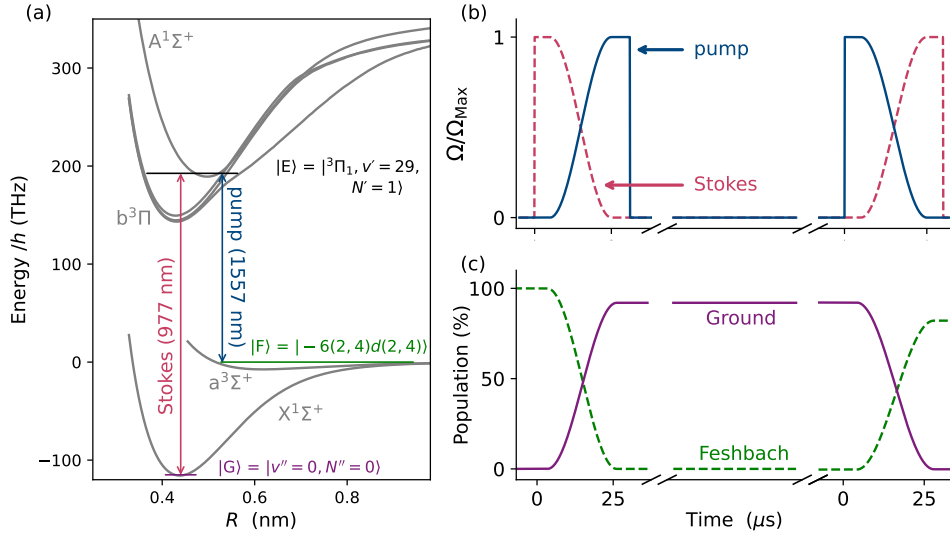


**Figure 3.3:** STIRAP overview. (a) Relevant energy levels used in STIRAP transfer. (b) Laser pulse scheme used in STIRAP, x-axis shared with (c). (c) Population in ground and the  $n = -6$  Feshbach state.

then image the atoms using conventional absorption imaging. Imaging light is provided by an “imaging” beam that is incident along the long axis of the cell. The imaging light is collected by an emCCD camera (Andor iXon 885) as shown in Fig. 3.1. We image in situ, providing a lower limit on detection of  $\sim 100$  atoms. The molecular population is then given by the mean population of each atomic species.

### 3.3 STIRAP

After creating weakly-bound Feshbach molecules, the final step is to transfer to the  $X^1\Sigma^+$  state using stimulated Raman adiabatic passage (STIRAP). This is achieved by realising a  $\Lambda$ -type energy level structure, coupling both the Feshbach state,  $|F\rangle$  and the ground state  $|G\rangle$  to a common excited state  $|E\rangle$  using two lasers. By carefully modulating of the intensity of the lasers, we are able to transfer the molecules from the Feshbach state to the ground state without populating the excited state.

To perform STIRAP following the association at 197 G and Stern-Gerlach separation, we tune our magnetic bias field to 181.5 G, transferring our popu-

lation to a  $n = -6$  state. This bias field persists when performing experiments unless otherwise specified.

We couple the Feshbach state,  $|F\rangle = |-6(2,4)d(2,4)\rangle$ , to a state in the  $b^3\Pi_1$  potential,  $|E\rangle = |b^3\Pi_1, v' = 29, N' = 1, M'_F = +4\rangle$  using the “pump” laser ( $\lambda = 1557$  nm). The specific state  $|E\rangle$  is selected for its favourable coupling with both  $|F\rangle$  and  $|G\rangle$  [153]. Coupling between  $|E\rangle$  and  $|G\rangle = |X^1\Sigma^+, v'' = 0, N'' = 0, M''_F = +5\rangle$  is provided by the “Stokes” laser ( $\lambda = 977$  nm). Fig. 3.3(a) shows the states involved in STIRAP.  $|G\rangle$  is a specific hyperfine state of  $v'' = 0, N'' = 0$ . With vertically polarised Stokes light, we access  $M_F = +4$  states and with horizontally polarised light, we access  $M_F = +3, +5$  [145]. Light from both lasers is combined using a dichroic mirror on the experimental table and is directed towards the molecules at normal incidence to the science cell using a common mirror via a periscope setup [113].

We can model the  $\Lambda$ -type system using the  $|F\rangle, |E\rangle, |G\rangle$  basis with the following Hamiltonian [154]:

$$\hat{H}_{\text{STIRAP}} = \frac{\hbar}{2} \begin{pmatrix} 0 & \Omega_p & 0 \\ \Omega_p & 2\Delta_p & \Omega_S \\ 0 & \Omega_S & 2(\Delta_p - \Delta_S) \end{pmatrix}, \quad (3.1)$$

where  $\Omega_p$  and  $\Omega_S$  are the Rabi frequencies of the pump and Stokes transitions respectively and  $\Delta_p$  and  $\Delta_S$  are the detunings from resonance of the pump and Stokes lasers respectively.

If we tune the lasers to be on the two-photon resonance ( $\Delta_p = \Delta_S = 0$ ), the eigenstates of  $\hat{H}_{\text{STIRAP}}$  can be given analytically as

$$\begin{aligned} |a^+\rangle &= \sin\theta \sin\phi |F\rangle + \cos\phi |E\rangle + \cos\theta \sin\phi |G\rangle \\ |a^0\rangle &= \cos\theta |F\rangle - \sin\theta |G\rangle \\ |a^-\rangle &= \sin\theta \cos\phi |F\rangle - \sin\phi |E\rangle + \cos\theta \cos\phi |G\rangle \end{aligned} \quad (3.2)$$

where  $\theta$  and  $\phi$  are “mixing angles” defined as

$$\tan\theta = \frac{\Omega_p}{\Omega_S} \quad (3.3)$$

and

$$\tan 2\phi = \frac{\sqrt{\Omega_p^2 + \Omega_S^2}}{\Delta_p}. \quad (3.4)$$

We want to utilise the  $|a^0\rangle$  eigenstate or “dark state” during STIRAP. This eigenstate crucially lacks an  $|E\rangle$  component, meaning there is no occupation of the excited state. Performing a “counter-intuitive” pulse sequence allows the transfer of the molecule population from  $|F\rangle$  to  $|G\rangle$  using the dark state.

Beginning with our Stokes light on and pump off, we find that Eq. 3.3 becomes zero and  $|a^0\rangle \equiv |F\rangle$ . Similarly, if the pump light is on and the Stokes light is off,  $|a^0\rangle \equiv |G\rangle$ . By ramping the Stokes light off and the pump light on, we are able to transfer the population completely without populating the excited state, shown pictorially in Fig. 3.3(b-c). However, in our experimental setup, we are limited in STIRAP transfer efficiency by the adiabaticity of the evolution of the dark state we can achieve.

The waists of STIRAP laser beams at the molecules are both  $\sim 35\mu\text{m}$  with peak laser powers of  $\sim 11\text{ mW}$  and  $\sim 7.6\text{ mW}$  for pump and Stokes respectively. We estimate our STIRAP lasers to have a linewidth of  $\sim 1\text{ kHz}$ . Details of the locking setup can be found in [113, 155]. We achieve typical one-way transfer efficiencies of 92(1)%. The STIRAP process is reversed for detecting ground state molecule population.

When necessary, STIRAP light (and light from other lasers) is coupled into a wavemeter (Bristol instruments 621 wavelength meter) for frequency referencing. The wavemeter provides an absolute frequency reference with an accuracy of 60 MHz.

### 3.4 Magnetic field coils

To generate the magnetic fields required in the science cell, we use five pairs of copper coils, each with the plane of the coils aligned horizontally as presented in Fig. 3.1(a). These coils are fixed in place with two Tufnol epoxy glass mounts (grade 10G/40, “G10”), separated vertically by a  $\sim 32.5\text{ mm}$  gap, allowing the science cell to lie between. The innermost and outermost coils are also arranged in an anti-Helmholtz configuration. They provide the levitation gradient and MOT fields respectively. The last three, labelled from inner-most to outer-most are Bias 1, Bias 2 and Bias 3 coils, arranged in a Helmholtz configuration. These provide bias fields of up to  $\sim 1000\text{ G}$ . Bias 1 can produce the larger (up to  $\sim 300\text{ G}$ ) contribution to the overall magnetic field while Bias 3 produces a smaller (up to  $\sim 60\text{ G}$ ) contribution. The Bias 1 and Bias 3 coils produce the fields we require for our purposes and so Bias

2 is disconnected. We use Bias 1 to provide a large offset in the magnetic field. We use Bias 3 as a means of finely controlling the aggregate magnetic field strength at the molecules.

The current flowing through the coils is regulated by an array of field-effect transistors (FETs). The gate voltage applied to the FETs is determined by a proportional-integral-derivative (PID) feedback loop, which monitors the current in the coils. This current is compared to a reference voltage provided by a field-programmable gate array (FPGA), which is connected to our experimental computer and controlled with the Durham experimental terminal software (DExTer). Feedback electronics are then employed to maintain the current in each coil pair stable to within approximately 1 part in 1000. To adjust the current supplied to a specific coil pair, we simply modify the voltage set point in DExTer.

### 3.4.1 Magnetic field calibration

We calibrate our magnetic field by observing Zeeman shifts in the ground state  $^{87}\text{Rb}$  hyperfine levels,  $|f = 1, m_f = 1\rangle \rightarrow |f = 2, m_f = 2\rangle$ . The effective Hamiltonian used to calculate the energy of a given hyperfine state of  $^{87}\text{Rb}$  occupying  $5S_{1/2}$  at a particular magnetic field is

$$\hat{H}_{\text{Rb}} = \hat{H}_{\text{HF}} + \hat{H}_{\text{Zeeman}} \quad (3.5)$$

where  $\hat{H}_{\text{HF}}$  is the hyperfine state structure component and

$$\hat{H}_{\text{Zeeman}} = \frac{\mu_{\text{B}}}{\hbar} (g_{\text{S}}\mathbf{S} + g_{\text{L}}\mathbf{L} + g_{\text{I}}\mathbf{I}) \cdot \mathbf{B} \quad (3.6)$$

is the contribution from the magnetic field interaction. Here,  $g_{\text{S}}$ ,  $g_{\text{L}}$  and  $g_{\text{I}}$  correspond to electron spin, electron orbital and nuclear g-factors respectively.  $\mu_{\text{B}}$  is the Bohr magneton,  $\hbar$  is the reduced Planck's constant and  $\mathbf{B}$  is the applied magnetic field.

Using our microwave horn (AtlanTecRF AS6366), we drive the  $|f = 1, m_f = 1\rangle \rightarrow |f = 2, m_f = 2\rangle$  transition with a Rabi frequency on the order of kHz. We subsequently utilise the Stern-Gerlach effect by applying a magnetic field gradient to spatially separate atoms in  $f = 1$  and  $f = 2$  states, allowing us to measure both populations. We then repeat the process for different microwave frequencies as presented in Fig. 3.4(a). The slight asymmetry suggests the magnetic field had not quite settled before the microwave pulse. We can reference the transition frequency to the Zeeman shift

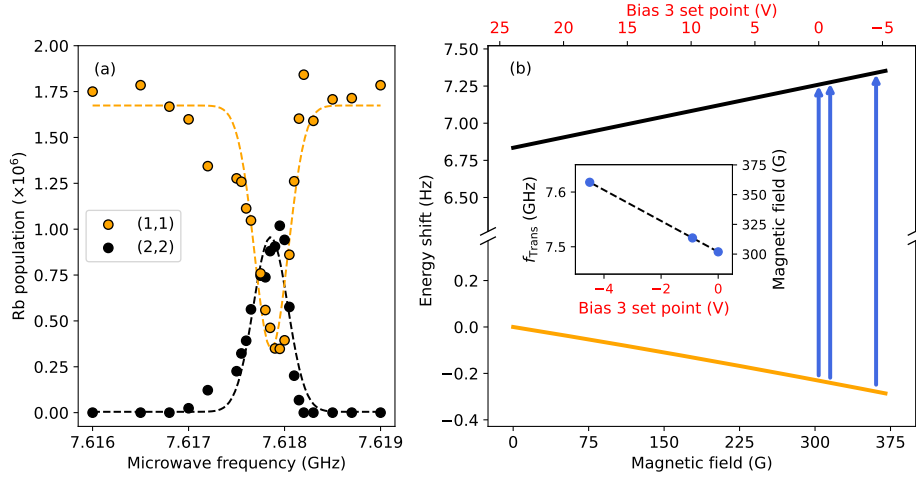


**Figure 3.4:** Magnetic field calibration. (a) Example spectroscopy of  $^{87}\text{Rb}$  hyperfine transition at  $\sim 360$  G, showing the population of both relevant states. States labelled  $(f, m_f)$  (b) Breit-Rabi diagram relevant hyperfine states. Blue arrows indicate the transitions used in calibration. Inset, centre frequency of calibration features as a function of Bias 3 voltage set point.

of the relevant states, shown by the Breit-Rabi diagram in Fig. 3.4(b) and discern the corresponding magnetic field.

We repeat this process for various Bias coil voltage set points. This confirms the linearity of our set point and magnetic field relationship as presented in the inset in Fig. 3.4(b). We are typically limited in determining the magnetic field at our atoms/molecules by the uncertainty in centres of the spectroscopic features. We typically know the magnetic field on the order of  $\sim 5$  mG.

### 3.5 Vacuum upgrades

The dispensers only contain a finite amount of alkali metal and eventually run out. For the duration of my PhD, the experiment was effectively running with depleted dispensers. Also throughout my PhD, the 55 L/s pump drew  $< 1$  mA during operation whereas the 40 L/s drew around 7 mA (both have a maximum pump current of 10 mA). We did not monitor the pressure of the vacuum chambers directly. Instead, we roughly inferred the quality of the vacuum by the amount of current each ion pump draws as it's operating. We concluded the possibility of a poor vacuum in the science cell.

The primary symptom of these factors was that the MOT load at the start of the day would be a few seconds, but increase to minutes after over the course of a day. It took at least one day of not running the experiment for the MOT load time to return to its initial rate, rendering consecutive days of experiments unfeasible. We decided to replace the dispensers and 40 L/s ion pump to rectify it.

### 3.5.1 Pulling out and breaking vacuum

We first move the vacuum chambers as a single piece away from the optics, coils and G10 coil mounts that surround the science cell to provide space for maintenance. The pyramid MOT and 1550 nm xODT optics are situated on breadboards which are moved to a separate table, clearing a path for the vacuum chambers to move. A ratchet strap system is then attached to the experimental table and the base on which the vacuum chambers sit. The chambers are then slowly winched away from the science MOT coils while base plates are screwed into the table on either side of the vacuum setup as it moves, providing a stabilising track.

Once the chambers are positioned away from the science MOT coils and optics as pictured in Fig. 3.5(a), we detach the up to air valve and connect a vacuum pump (Pfeiffer vacuum turbo pump) via vacuum bellows. The pump is then activated, decreasing the pressure in the bellows and poppet valve, as presented by the blue line in Fig. 3.5(b). Pressure is measured using the Pfeiffer pump's internal monitoring system. After the pressure decrease begins to slow, we turn both ion pumps off and open the poppet on the poppet valve by loosening the screw.

Next, we attach a Nitrogen canister to the vacuum pump, allowing Nitrogen to fill the chambers. Nitrogen is an inert gas that prevents moisture in the air from attaching to the inside of the vacuum chambers when the inside is exposed. When the pressure inside the chambers is about the pressure in the room <sup>1</sup>, we turn off the vacuum pump. Coils surrounding the pyramid MOT are then removed.

The old 40 L/s ion pump is removed and the new one is installed (Agilent Vaclon Plus). The new dispensers are spot-welded onto a pair of feed-throughs. The old feed-throughs are removed and the new ones are placed.

---

<sup>1</sup>This is monitored using an inflatable rubber ball that is connected to the tube carrying Nitrogen from the canister to the pump.

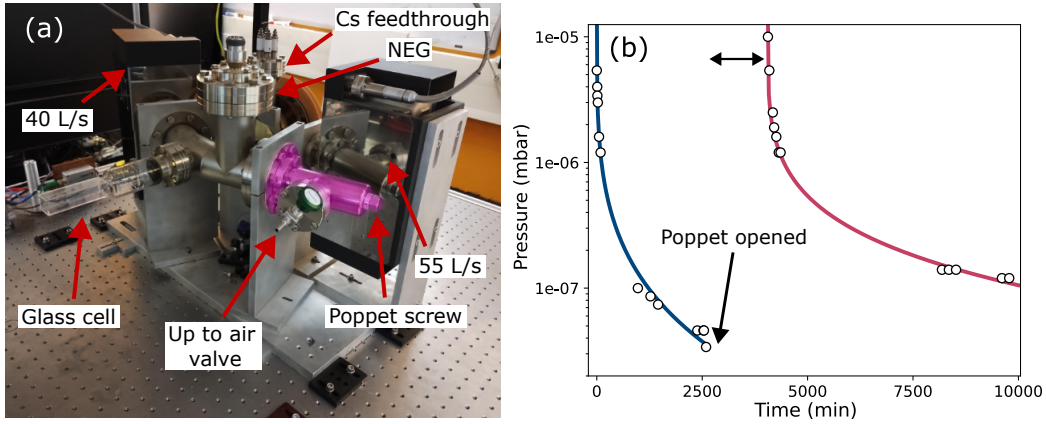


**Figure 3.5:** Pulling out the vacuum chambers and first decompression steps. (a) Vacuum chambers pulled away from the science MOT coils and surrounding optics. The purple shaded region is the poppet valve referenced in the text. (b) Pressure measured in the Pfeiffer as a function of time during decompression of the poppet valve and second decompression after maintenance. Ion pump and dispensers replaced in double-headed arrow region. Exponential curves to guide the eye.

To accomplish this, the pyramid viewport is removed so that the new dispensers can be bent into position correctly. We subsequently reseal the vacuum chambers by reattaching the pyramid viewport and reactivating the Pfeiffer pump. The pressure is then allowed to decrease until it starts to plateau as shown by the red line in in Fig. 3.5(b).

### 3.5.2 Baking vacuum and activating dispensers

To achieve ultra-high vacuum, it is necessary to bake the chamber at high temperature [156, 157]. We heat the vacuum setup using three heater tapes wrapped around the chambers, flanges, ion pumps, feed-throughs and bellows. The glass cell is encased in an aluminium cylindrical tube for protection during the baking process. The tube is secured to the vacuum setup with a set of screws, fastening it around the flange at the base of the cell. It is then supported by a homemade aluminium stand which is in turn screwed to the optical bench. We tape down nine thermocouples to different components of the setup for temperature monitoring. The whole structure is then wrapped in aluminium foil to provide insulation as pictured in Fig. 3.6(a).

We heat the setup, steadily increasing the temperature over a few days up to  $\sim 180^\circ\text{C}$ . Pressure and the mean temperature of all nine thermocou-

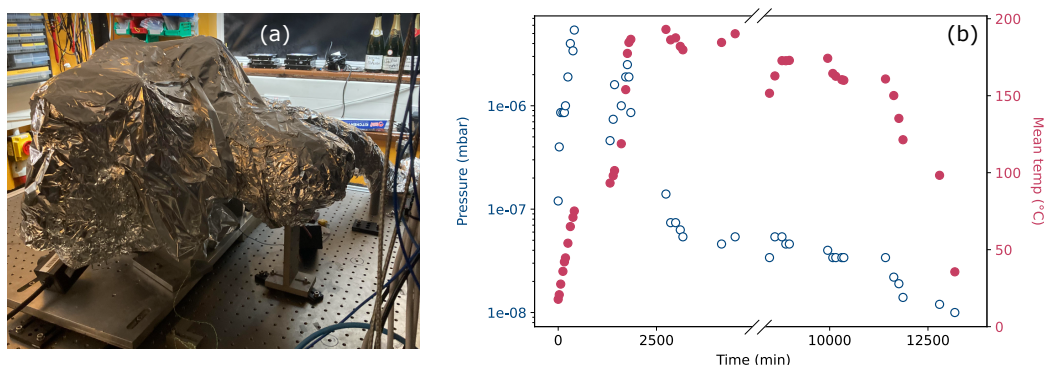


**Figure 3.6:** Vacuum baking and pressure/temperature monitoring. (a) Vacuum chambers and bellows surrounded by heater tape and aluminium foil. (b) Pressure measured in the Pfeiffer (blue unfilled markers) and mean temperature of all nine thermocouple readings (red filled markers) during the baking stage as a function of time.

ples during the baking process are presented in Fig. 3.6(b). As temperature increases, the moisture absorbed into the inner walls of the chambers is expelled and the pressure rises. The temperature is subsequently decreased in the next few days until the heater tapes are turned off. Connections between the vacuum feed-throughs and dispenser power supplies are then installed.

Next, we activate our new dispensers by passing high current through them. Current is supplied to each of the dispenser sets in turn, beginning at 0 A and increasing up to 4.9 A and 5.5 A for Cs and Rb respectively in  $\sim 0.5$  A steps every 10 seconds for a period of  $\sim 100$  seconds and then turned off. Activation causes the relevant dispensers to produce an incandescent glow as pictured in Fig. 3.7. We typically pass  $\sim 3$  A of through the dispensers during normal operation. After activating each of the dispensers, the non-evaporable getter (NEG) power cable is connected.

We then perform a second baking stage, similar to the first, to remove unwanted particulates released after activation. We increase the temperature up to  $\sim 150^\circ\text{C}$  over two days. The temperature is then reduced to  $\sim 80^\circ\text{C}$  in  $\sim 1$  day and the NEG is activated for around 1 hour causing pressure to increase sharply. The NEG cable is then disconnected and the pressure is given time to stabilise. Finally, the ion pumps are turned on, the poppet is closed, the up to air valve is reattached and closed and the heater tapes are turned down until they can be removed. The foil is removed and the vacuum chambers are then pushed back along the optics base track to their original



**Figure 3.7:** Incandescence of a set of Rb dispensers during activation. Pyramid MOT mirrors visible as the square object in the centre of the viewport. Other atom dispensers are arranged around the pyramid mirrors in a hexagonal formation.

position.

## 3.6 Microwave sources

$X^1\Sigma^+$  RbCs molecules rotational energy manifolds are spaced with GHz separation. Accessing different rotational states requires microwave emitters which usually come in the form of antennae. In our experiment, we have a homemade linear  $\lambda/4$  antenna, a commercial microwave horn and a homemade dipole antennae array. The latter is a recent addition whereas the former two have been a permanent part of the experiment for years [117]. With the exception of the horn, all our microwave sources can be considered “omnidirectional” (they have no directional pattern in a given plane).

### 3.6.1 Microwave generators

Microwave sources are connected via SMA cables to analogue signal generators. We use the following microwave generators in our experiment:  $2 \times$  Agilent MXG N51832,  $2 \times$  Agilent E4400B, Agilent E4421B,  $2 \times$  Windfreak SynthHD (v2) and a Windfreak SynthNV. All sources are connected to the same external 10 MHz GPS disciplined oscillator (Jackson Labs Fury) for frequency referencing when necessary. Microwave pulsing is controlled through

a TTL signal provided by DExTer or by using the internal pulsing function of the signal generators.

### 3.6.2 Linear monopole and microwave horn

A homemade  $\lambda/4$  antenna is installed to drive  $N'' = 0 \rightarrow N'' = 1$  rotational transitions. The antenna consists of a 1 mm diameter copper wire soldered to the pin of a female SMA connector. A square ceramic-filled PTFE composite (Rogers Corp. RO3003) is soldered to the ground of the SMA connector forming a reflective ground plate. The antenna is taped to the lower G10 and aligned along the long-axis of the cell as shown in Fig. 3.8.

We use a microwave horn (AtlanTecRF AS6366) which is specified for  $\sim 2$  GHz to 13 GHz to drive transitions between rotational states with  $N'' \geq 1$ . The horn is equipped with an output designed to produce circularly polarised light. However, positioning the horn along our quantisation axis will result in MOT beams being blocked. It is instead positioned at  $\sim 30^\circ$  angle from the quantisation axis above the cell and outside G10 as shown in Fig. 3.8. The microwaves propagate through the G10 and coils.

### 3.6.3 Characterising microwave polarisation

We first characterise the polarisation of our current microwave sources by performing a series of Rabi oscillations on  $\sigma_+$ ,  $\sigma_-$  and  $\pi$  transitions. Producing a microwave source with well-defined polarisation is a powerful tool for quantum state control. The rich hyperfine structure of ultracold molecules becomes problematic when attempting high-fidelity state transfer, owing to off-resonant coupling to neighbouring states<sup>2</sup>. When coupling to neighbouring rotational states,  $\Delta M_F = +1, -1, 0$  transitions are driven by right-handed circular, left-handed circular and vertically polarised microwaves respectfully in our experiment. Consider the case of a well-defined microwave source with right-handed circular polarisation at the molecules. Only  $\Delta M_F = 1$  transition are available. Beginning in the spin-stretched ground state, only the spin-stretched state in each rotational manifold is coupled to. This allows the driving of transition with high Rabi frequency without fear of off-resonantly coupling to different hyperfine states, providing a “cleaner” landscape in which to perform quantum science experiments. Also, microwave sources

<sup>2</sup>This is especially true when coupling to higher rotational energy states due to the hyperfine state population and  $N$  relationship described in section 2.2.4.

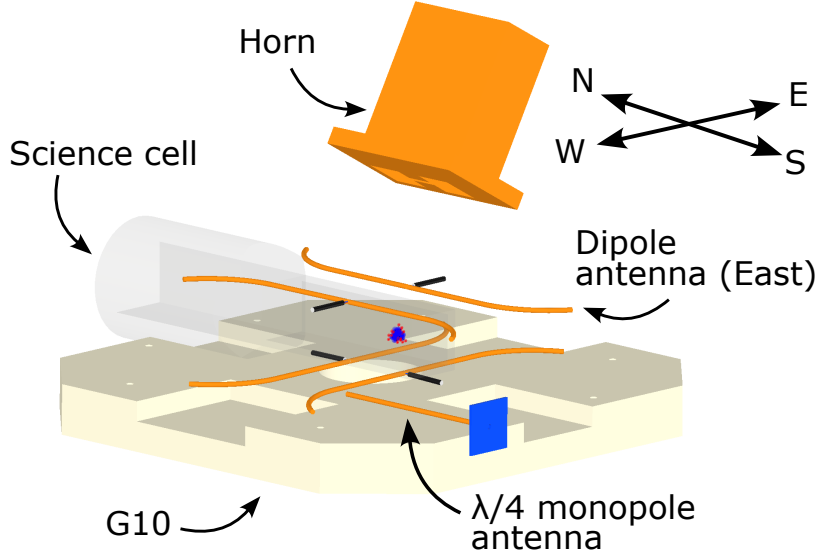


**Figure 3.8:** Microwave sources diagram. Top Tufnol G10 omitted for viewing purposes. Reflective base plate for the  $\lambda/4$  monopole antenna shown in blue. RG174 cables dipole antennae components shown in black.

with well-defined polarisations have been used in ultracold diatomic molecule experiments to enhance the ratio between elastic and inelastic collisions in the sample. This technique is known as “microwave shielding” [158–162].

With the exception of our horn, all microwave sources are housed between the Tufnol coil mounts surrounding the cell <sup>3</sup>. We operate in the near-field regime, where the angular distribution of the microwave field is independent of the distance from the antenna [163]. Additionally, the microwaves interact with the surrounding magnetic field coils and optics near the cell, making testing antennae using a separate “probe” antenna in experiment unreliable [164]. Instead, we determine the polarisation of our microwave sources in-situ by driving  $\sigma^+$ ,  $\sigma^-$  and  $\pi$  rotational transitions in RbCs with the same power and comparing the resulting Rabi frequencies in each case.

When driving a given transition between two quantum states, the Rabi frequency is defined as [165]

$$\Omega_{i,j} = \frac{d_{i,j} \cdot |\vec{E}|}{\hbar}, \quad (3.7)$$

<sup>3</sup>The horn is found to be sufficiently directional for our purposes and thus can reside further from the cell.

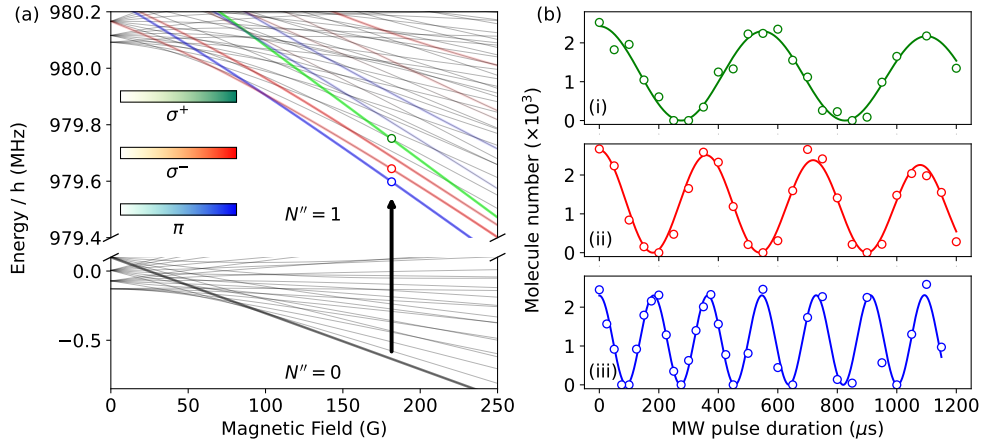


**Figure 3.9:** Example microwave source polarisation determination experiment. (a) Breit-Rabi diagram of the rotational ground state and first rotationally excited state’s hyperfine structure. Darker state in the  $N'' = 0$  subplot denotes our initial state,  $(0, +5)$ . Rotational transitions denoted by the black arrow to the relevant  $N'' = 1$  states shown by the unfilled points. The transition dipole moment for each  $\Delta M_F = 1, -1$  and  $0$  are given by the intensity of green, red and blue colouring respectively. (b) Rabi oscillations driven by our antenna, coupling to (i)  $(1, 6)$ , (ii)  $(1, 4)_0$  and (iii)  $(1, 5)_0$ .

where  $d_{i,j}$  is the transition dipole moment and  $\vec{E}$  the electric field vector. Values of  $d_{i,j}$  are calculated using [141]. For  $X^1\Sigma^+$  state RbCs at 181.5 G, hyperfine states in the low-lying rotational manifolds are separated by  $\sim 100$  kHz. We assume when varying the frequency within this range the change in the amplitude of the electric field vector,  $|\vec{E}|$ , at the molecules is negligible providing the microwave generator power remains constant.

We then perform Rabi oscillations on the transitions  $(0, M_F'') \rightarrow (1, M_F')$  for  $M_F' = M_F'', M_F'' + 1$  and  $M_F'' - 1$  at a fixed power with resonant microwave fields. Particular  $(1, M_F')$  states are chosen by their significant  $d_{i,j}$  values as presented in Fig. 3.9(a). Resulting Rabi oscillations are subsequently fitted with a sinusoidal function to extract their frequencies as illustrated in Fig. 3.9(b).

By comparing Rabi frequencies and their corresponding transition dipole moments, we can construct a polarisation matrix for a given microwave source:

Source	$f$ (MHz)	$\chi_+$	$\chi_0$	$\chi_-$
Linear monopole	$\sim 980$	0.353(13)	0.793(12)	0.496(14)
Horn	$\sim 1960$	0.359(5)	0.918(12)	0.165(7)
Horn	$\sim 2940$	0.454(7)	0.452(14)	0.77(3)
Horn	$\sim 3920$	0.456(7)	0.59(2)	0.67(3)

**Table 3.1:** Polarisation of microwaves produced by  $\lambda/4$  antenna and Horn.

$$\chi = \begin{pmatrix} \chi_+ \\ \chi_- \\ \chi_0 \end{pmatrix}, \quad (3.8)$$

where  $\chi_+$ ,  $\chi_-$  and  $\chi_0$  correspond to the electric field polarisation driving  $\sigma^+$ ,  $\sigma^-$  and  $\pi$  transitions. We normalise  $\chi$  such that  $\chi_+^2 + \chi_-^2 + \chi_0^2 = 1$ .

We can now rewrite equation 3.7 in matrix form using the  $\sigma^+$ ,  $\sigma^-$  and  $\pi$  transition basis:

$$\begin{pmatrix} \Omega_+ \\ \Omega_- \\ \Omega_\pi \end{pmatrix} = \frac{1}{\hbar} \begin{pmatrix} d_+ \\ d_- \\ d_0 \end{pmatrix} \cdot \chi^T |\vec{E}| \quad (3.9)$$

where  $\Omega_{+,-,\pi}$  and  $d_{+,-,\pi}$  denote the Rabi frequency and transition dipole moments of  $\sigma^+$ ,  $\sigma^-$  and  $\pi$  transitions respectively.

We repeat our measurements for our different microwave sources as presented in table 3.1. Uncertainties are dominated by the fittings to Rabi oscillations. Results for higher frequencies involved initialising our molecule population in different  $N''$  states before performing Rabi oscillations. The microwave horn is designed for a 2 to 13 GHz range and was subsequently tested at multiple frequencies. The measurements are of the polarisations of the microwaves at the molecules, not the emitter, given their dependence on their placement with respect to the quantisation axis and the interactions of the emitted microwaves with the surrounding objects.

### 3.6.4 Engineering arbitrary polarisations using phased-arrays

The polarisation of microwaves at our molecular sample emitted by a single antenna at a given frequency cannot be tuned without physically changing the dimensions of the antenna or moving the antennae in the experiment. Neither of which produces reliable results. Instead, using multiple antennae at once causes interference between waves of polarisations that drive a given transition. This allows suppression or amplification of coupling depending on the relative phases of the interfering waves. We perform a proof-of-concept experiment by changing the relative phase of the microwaves emitting from two different sources and observing variations in the Rabi frequency of a given transition.

Our experiment is equipped with four out-of-vacuum U-shaped electrodes positioned above and below the science cell, fixed in Tufnol G10 mounts. Together, they can produce a maximum DC electric field of 1.5 kV/cm across our molecular sample [166]. Electrodes are shown in Fig. 3.10(a) <sup>4</sup>. By connecting function generators to these electrodes, we drive rotational transitions in ground state RbCs.

We resonantly drive  $(0, +5) \rightarrow (1, +5)_0$  transitions using one of the top electrodes, as illustrated in Fig. 3.10(b)(i), using an MXG microwave generator. We then drive the same transition using a bottom electrode with a separate MXG. We tune the power of the signal generator connected to the bottom electrode such that each electrode drives the transition with the same Rabi frequency as shown in Fig. 3.10(b)(ii). Both MXGs are clocked together by daisy-chaining the GPS frequency reference from one to the other. This allows their relative phase relationship to be robust throughout our experiment. We observe no detectable relative phase drift when we connect our signals to an oscilloscope.

We then fix the microwave time to perform a  $\pi/2$ -pulse if we were to drive the transition using a single electrode. Next, we pulse on both electrodes and vary the relative phase of the microwaves. As presented in Fig. 3.10(b)(iii), when we observe a full-contrast variation in ground state population as we change the relative phase of the microwaves. Rabi frequency is minimised when the microwaves are in phase and maximised when out of phase.

---

<sup>4</sup>Images of stopwatch uploaded to WikipediaCommons.org by Videoplasty.com. Image of MXG found on TestWall.com.

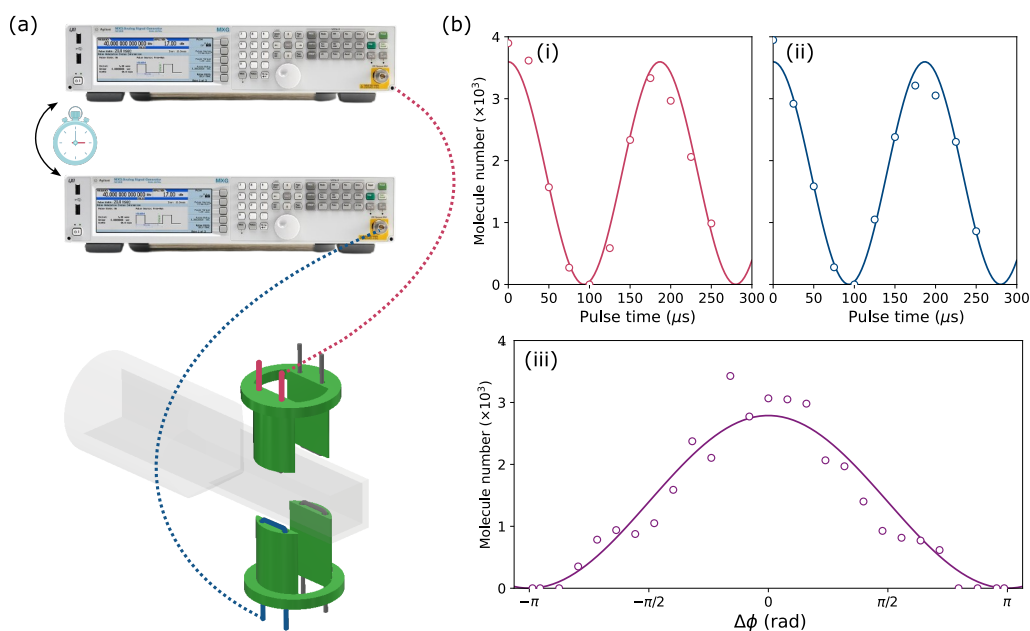


**Figure 3.10:** Electrode relative phase experiment. (a) Experimental setup diagram. (b) Population in the (0, +5) state as a function of pulse time with microwaves resonantly driving the  $(0, +5) \rightarrow (1, +5)_0$  transition using the (i) top and (ii) bottom electrodes. (iii) (0, +5) population as a function of the relative phase of the microwaves at a pulse time of  $40\mu\text{s}$ .

### 3.6.5 Dipole antennae array

Replacing atomic dispensers and the vacuum pump described in section. 3.5 required physically moving the vacuum chambers away from the magnetic coils and surrounding optics. This provided an opportunity for installing an array of four linear dipole antennae arranged in a crossed formation as presented in Fig. 3.8. The symmetry of the array is ideal for engineering arbitrary polarisations and its proximity to the cell is beneficial considering the  $1/r^2$  power relationship.

We produce four identical homemade dipole antennae from 2 mm diameter copper enamel-coated wire. One length of wire is soldered to the inner conductor of a 50 Ohm coaxial cable (RG174) and another to the grounded “screening” of the RG174<sup>5</sup>. Using our Windfreak SynthNV mi-

<sup>5</sup>This array was nicknamed “Plankton” given its similarity in appearance to the Sponge-

microwave generator and a directional coupler (Mini-Circuits ZFDC-10-5-S+), we create a scalar-network analyser setup as presented in Fig. 3.11. We observe dips in the return-loss spectra, signifying frequencies where the antenna emits more power than it reflects. We cut the “arms” of the antenna to the correct length such that a dip in the return-loss spectra exists at  $\sim 1$  GHz.

The antennae are then glued to the inside of the Tufnol coil mounts with fast-set epoxy, creating an antenna array as shown in Fig. 3.8. These antennae are bent into positions to avoid direct contact with the cell whilst maintaining a symmetric array layout. Array antennae are labelled by position furthest along each cardinal direction as illustrated in Fig. 3.8.

We then perform the polarisation characterisation measurement as conducted with the other microwave sources in section 3.6.3. These results are presented in table 3.2. Engineering right-circularly polarised microwaves would involve producing strongly vertically polarised microwaves with each pair of parallel dipole antennae and then implementing a relative phase shift between the two pairs.

---

bob SquarePants<sup>TM</sup> character of the same name.

Source	$f$ (MHz)	$\chi_+$	$\chi_0$	$\chi_-$
North dipole antenna	$\sim 980$	0.234(12)	0.764(5)	0.602(7)
South dipole antenna	$\sim 980$	0.386(14)	0.782(9)	0.49(2)
East dipole antenna	$\sim 980$	0.696(3)	0.676(3)	0.270(2)
West dipole antenna	$\sim 980$	0.1092(10)	0.979(3)	0.170(14)

**Table 3.2:** Polarisation of microwaves produced by different dipole antennae.

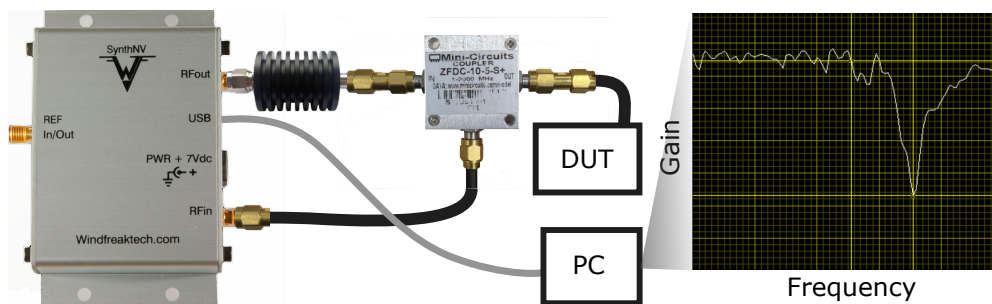


**Figure 3.11:** Antenna scalar-network analyser setup. The output of the Windfreak SynthNV is connected to the output port of the directional coupler via a 50 Ohm attenuator. The device under test (DUT) is attached to the input port of the directional coupler. The coupled port from the directional coupler is connected to the input port of the SynthNV. The SynthNV is connected via a USB to a PC which displays the gain of the input port as the frequency of the output is varied. The SynthNV general user interface is shown on the extreme right-hand side. The curve presents gain as a function of frequency. Vertical/horizontal lines serve as markers.

# Chapter 4

## Magic Spectroscopy

### 4.1 Introduction

Many quantum simulation and computation architectures incorporating neutral atoms and molecules rely on optical trapping for the spatial confinement of particles [6–8, 17, 32–35]. However, trapping induces inhomogeneous differential ac Stark shifts in quantum states, often restricting quantum coherence during experiments. For dipolar molecules, ensuring long coherence times between rotational energy states is essential for making quantum simulation and computation feasible. The solution involves accessing a so-called rotationally ‘magic’ condition whereby the energy of relevant rotational states are shifted equally, eliminating differential effects. Magic trapping schemes have been an invaluable tool for engineering high fidelity atomic and molecular clocks with the magic relating to shifts in electronic and vibrational states respectively [167–169]. However, a rotationally magic condition for diatomic molecules has proved difficult to access.

Although many rotationally magic wavelengths have been identified for different molecules [170, 171], their applicability is often limited by the proximity to electronic transitions. Nearby transitions cause unintended photon scattering in the trap, limiting the states lifetime. Guan *et al.* [172] have identified a magic wavelength condition for RbCs at 181 G which is compatible with long trap lifetimes owing to its existence at a relatively large detuning from nearby electronic states. Moreover, unlike in the case of other molecular magic detunings, an external electric field is not required [47, 170]. This relatively large detuning coupled with the relatively small energy splitting of RbCs rotational states decreases the difference in magic detuning for different rotational states and lays the foundation for a multiply-rotationally

magic trap.

In this chapter, we begin by presenting the relevant theoretical background involved in creating magic wavelengths in RbCs. We then report a comprehensive investigation into the transitions used in accessing magic rotational conditions using high-resolution spectroscopy. Finally, we demonstrate the magic condition is accessed by performing a series of Ramsey experiments with different rotational states.

### 4.1.1 RbCs rotational magic background

Examining the form of Eq. 2.16, it's evident that satisfying the condition of  $\alpha_{\perp} = \alpha_{\parallel}$  causes  $\alpha^{(2)}$  to vanish. This eliminates differential ac Stark shifts between  $N'' = 0$  states and higher rotational states. The values of  $\alpha_{\perp}$  and  $\alpha_{\parallel}$  in free space are given by background polarisabilities,  $\alpha_{\perp}^{\text{bg}}$  and  $\alpha_{\parallel}^{\text{bg}}$  in the molecule frame derived from the contributions from all the far-detuned rovibronic states [173–175].  $\alpha_{\perp}$  and  $\alpha_{\parallel}$  can be approximated as  $\alpha_{\perp}^{\text{bg}}$  and  $\alpha_{\parallel}^{\text{bg}}$  in the presence of light far-detuned from an electronic transition. However, in the presence of light tuned near electronic transitions,  $\alpha_{\perp}$  and  $\alpha_{\parallel}$  are modified according to their detunings to the transitions. For  $\Sigma$  molecules like RbCs in the electronic ground state,  $\alpha_{\parallel}$  is derived from the sum over all allowed  $\Sigma \rightarrow \Sigma$  transitions and  $\alpha_{\perp}$  is derived from the sum over all allowed  $\Sigma \rightarrow \Pi$  transitions.

We can achieve the magic condition for RbCs by tuning our light between nominally forbidden transitions to the  $b^3\Pi_0$  potential [172], as shown in Fig. 4.1(a). These transitions are weakly allowed due to mixing between  $b^3\Pi$  and the nearby  $A^1\Sigma^+$ . Coupling to the  $A^1\Sigma^+$  component allows tuning of  $\alpha_{\parallel}$ , while the  $\alpha_{\perp}$  component remains nearly constant as the nearest transition to a  $^1\Pi$  potential is detuned by over 100 THz [130]. We can therefore find a detuning where  $\alpha_{\parallel} = \alpha_{\perp}$ , leading to  $\alpha^{(2)} = 0$  as illustrated in Fig. 4.1(c). This transition is accessed with laser light of  $\sim 1145$  nm. For spectroscopic experiments, we will refer to the laser providing  $\sim 1145$  nm light as our ‘probe’ laser.

Throughout this chapter, we sometimes refer to  $X \rightarrow b$  using the shorthand  $''$  and  $'$  to negate the need for  $X$  and  $b$ . For example, the  $X^1\Sigma^+(v'' = 0, N'' = 0) \rightarrow b^3\Pi_0(v' = 0, N' = 1)$  transition can be written as  $v'' = 0, N'' = 0 \rightarrow v' = 0, N' = 1$ .

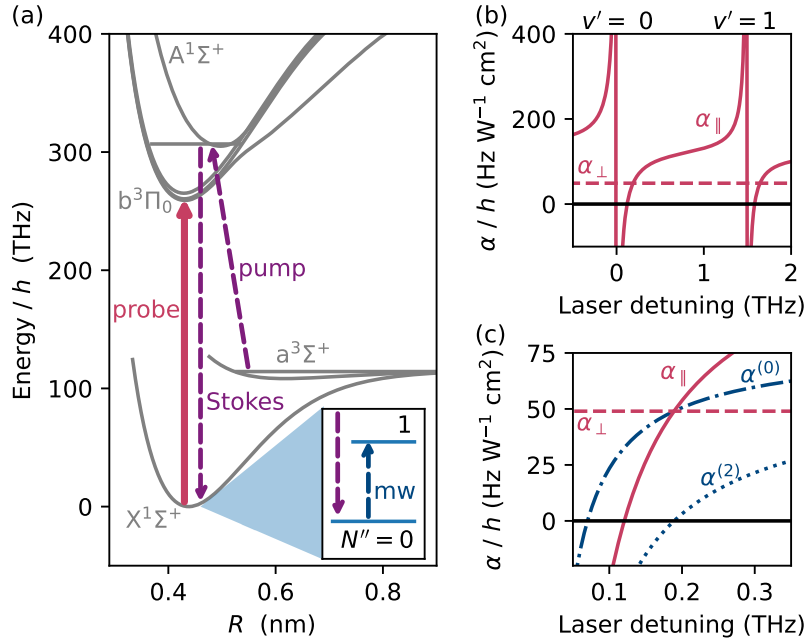


**Figure 4.1:** Relevant RbCs transitions and the scheme for a rotationally magic trap. (a) Electronic potentials of RbCs. The vertical red arrow labelled ‘probe’ indicates the forbidden  $X^1\Sigma^+(v'' = 0) \rightarrow b^3\Pi_0(v' = 0, 1, 2)$  transitions that are the subject of investigation. The dashed purple arrows indicate the pump and Stokes transitions used in the transfer of RbCs to the ground state. The inset illustrates the rotational transitions in the ground state which we drive coherently with microwave (mw) fields. (b) The molecule-frame polarisabilities as a function of the probe laser detuning near the lowest  $X^1\Sigma^+ \rightarrow b^3\Pi_0$  transitions. Solid and dashed lines indicate  $\alpha_{\parallel}$  and  $\alpha_{\perp}$  respectively. (c) Zoom in around the magic detuning region. The blue dot-dash and dotted lines indicate the isotropic ( $\alpha^{(0)}$ ) and anisotropic ( $\alpha^{(2)}$ ) polarisabilities respectively.

### 4.1.2 RbCs rotational magic theory

In the absence of hyperfine interactions, the polarisability near the lowest  $X^1\Sigma^+ \rightarrow b^3\Pi_0$  transitions for molecules in  $X^1\Sigma^+$  with well defined  $N''$ ,  $M''_N$  can in general be approximated by [172]

$$\alpha_{N'', M_{N''}} = \sum_{v'} -\frac{3\pi c^2}{2\omega_{v'}^3} \left[ A_{M_{N''}}^{N''}(\beta) \frac{\hbar\Gamma_{v'}}{\Delta_{v'} + L_{N''}} + B_{M_{N''}}^{N''}(\beta) \frac{\hbar\Gamma_{v'}}{\Delta_{v'} + R_{N''}} \right] + \left[ A_{M_N}^{N''}(\beta) + B_{M_N}^{N''}(\beta) \right] (\alpha_{\parallel}^{\text{bg}} - \alpha_{\perp}^{\text{bg}}) + \alpha_{\perp}^{\text{bg}}, \quad (4.1)$$

where  $c$  and  $\hbar$  are the speed of light in a vacuum and the reduced Planck constant respectively.  $\Delta_{v'}$  is the detuning of the light from the transition, with transition energy  $\hbar\omega_{v'}$  and linewidth  $\Gamma_{v'}$ . The linewidth is related to the transition dipole moment  $\mu_{v'}$  by [25]

$$\Gamma_{v'} = \frac{\omega_{v'}}{3\pi\epsilon_0\hbar c^3} |\mu_{v'}|^2, \quad (4.2)$$

where  $\epsilon_0$  is the vacuum permittivity. This does not include the angular factors that govern the relative decay rates to different rotational states, which are incorporated into  $A_{M_N}^{N''}(\beta)$  and  $B_{M_N}^{N''}(\beta)$ . In this work, we primarily consider stretched states with  $|M_N''| = N''$ . For these states

$$A_{\pm N''}^{N''}(\beta) = \frac{N''}{2(2N'' + 1)} \sin^2 \beta \quad (4.3)$$

and

$$B_{\pm N''}^{N''}(\beta) = \frac{2N''^2 + 3N'' + 2}{2(2N'' + 1)(2N'' + 3)} - \frac{N''(2N'' - 1)}{2(2N'' + 1)(2N'' + 3)} \cos^2 \beta \quad (4.4)$$

where  $\beta$  is the angle between the polarization of the laser with respect to the quantisation axis. Note, that equivalent angular factors for states with  $M_N'' = 0$  are given in [172]. The energies  $L_{N''}$  of the  $N' = N'' - 1$  branch and  $R_{N''}$  of the  $N' = N'' + 1$  branch are

$$L_{N''} = N''(N'' + 1)\tilde{B}_{v''} - [N''(N'' - 1) - 2]\tilde{B}_{v'}, \quad (4.5)$$

and

$$R_{N''} = N''(N'' + 1)\tilde{B}_{v''} - [(N'' + 1)(N'' + 2) - 2]\tilde{B}_{v'}, \quad (4.6)$$

where  $\tilde{B}_{v''}$  and  $\tilde{B}_{v'}$  are rotational constants for the  $X^1\Sigma^+$  and the  $b^3\Pi_0$  states respectively at 181 G. We consider these “effective” rotational constants. In all calculations shown in this work, the sum in Eq. 4.1 includes vibrational states up to  $v' = 3$ . Contributions to Eq. 4.1 are of diminishing magnitude for increasing values of  $v'$  for given values of  $N''$  and  $M_N''$ , primarily owing to decreasing transition linewidths.

The dependence of the polarisability of a given state on  $\beta$  is caused by non-zero  $\alpha^{(2)}$ . Therefore, to find where  $\alpha^{(2)} = 0$  we must find where the polarisability becomes independent of  $\beta$ . We find a simple analytic solution for where this condition is met in the limit of no rotational structure, i.e. setting  $\tilde{B}_{v''} = \tilde{B}_{v'} = 0$  such that  $L_{N''} = R_{N''} = 0$ . By only considering the contribution from a single transition in isolation, calculating the partial derivative of the polarisability with respect to  $\beta$  and setting it to be zero, we find

$$\frac{\partial \alpha_{N'', M_N''}}{\partial \beta} = \left( \frac{\partial A_{\pm N''}^{N''}}{\partial \beta} + \frac{\partial B_{\pm N''}^{N''}}{\partial \beta} \right) \left( \frac{3\pi \hbar c^2 \Gamma_{v'}}{2\omega_{v'}^3 \Delta} - (\alpha_{\parallel} - \alpha_{\perp}) \right) = 0. \quad (4.7)$$

For this condition to be met for all values of  $\beta$ , the right-hand term must be zero, and by rearrangement we can therefore find the approximate magic detuning

$$\Delta = \frac{3\pi \hbar c^2 \Gamma_{v'}}{2\omega_{v'}^3 (\alpha_{\parallel} - \alpha_{\perp})} \quad (4.8)$$

that is independent of  $N''$ ,  $M_N''$ , and  $\beta$ . Note, that an equivalent expression is derived in [172] by taking the first term of a Taylor-expansion of the right-hand side of Eq. 4.1 with respect to  $L_{N''}$  and  $R_{N''}$ . Using our value of  $\Gamma_{v'=0}$  given in this chapter, we determine the magic detuning in the absence of rotational structure given by Eq. 4.8 to be 210(23) GHz. In practice, the true magic detuning is different to that expected from Eq. 4.8 by  $\sim 14\%$ . The largest effect is due to the proximity of neighbouring electronic transitions. However, there are also small effects due to the presence of the rotational structure.

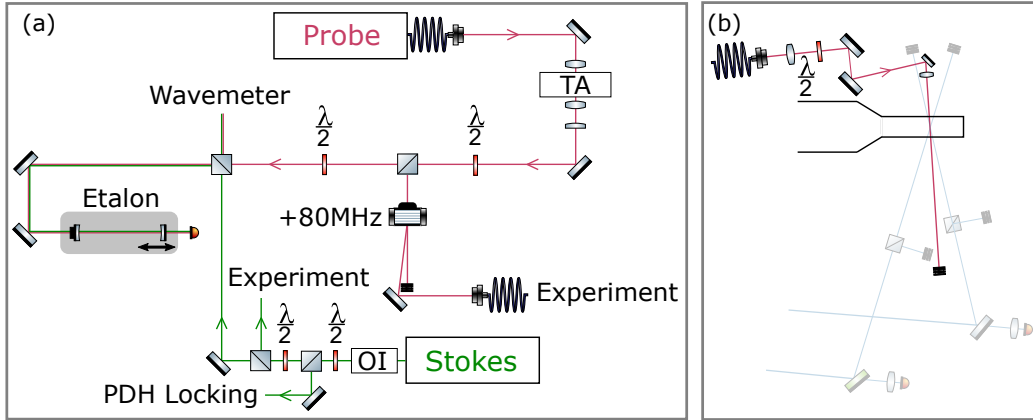


**Figure 4.2:** Homebuilt probe laser setup. (a) Setup for scanning transfer cavity frequency locking and intensity modulation before light is transferred to the experimental table via an optical fibre. Optical isolator denoted by “OI” in Stokes path. (b) Experimental table setup. The position of the final lens before the cell is changed depending on the beam waist we need at the molecules. 1550 nm xODT setup presented faintly for reference.

## 4.2 Experimental setup

We utilise two 1145 nm probe lasers for spectroscopic measurements, a home-built external cavity diode laser and a Toptica DL pro.

The homebuilt laser is based upon an Innolume GC-1180-100-TO-200-B gain chip. This provides light in the range 1129 nm to 1154 nm. The laser can provide up to 20 mW of optical power at the molecules. Where higher powers than this are used, the light from this laser seeds a tapered amplifier, “TA” (Toptica Eagleyard TA-1135-0500-1), that boosts the power at the molecules up to  $\sim 100$  mW, shown in Fig. 4.2(a). Depending on the intensity required, we use beam waists ranging from  $20 \mu\text{m}$  to  $440 \mu\text{m}$  at the molecules. The beam waist is adjusted by varying the position of the final lens before the beam reaches the molecules as illustrated in Fig. 4.2(b). The  $1/e$  radius of the molecule cloud in the plane orthogonal to the laser propagation is  $7 \mu\text{m}$ ; at the smallest beam waists used, there is therefore significant variation of the intensity across the sample. The light is linearly polarised and propagates in the plane parallel or orthogonal to the magnetic bias field that defines the quantisation axis, adjusted using a half-wave plate.

We can tune the frequency of the homebuilt probe laser over a 6.5 THz range with single-mode character by manually adjusting the angle of the feed-

back grating that forms the external cavity. Smaller adjustments to the laser frequency ( $< 10$  GHz) are made by varying the voltage supplied to a piezo that controls the displacement of the grating. When required, we stabilise the laser frequency with reference to the Stokes laser using an Arduino-based scanning transfer cavity lock (STCL) [176] that feeds back to the piezo voltage.

For higher precision spectroscopic measurements, 1145nm light is provided by a Toptica DL pro laser which produces around 30 mW directly out of a fibre-coupled output. About 3% of light is picked off using a beam sampler for frequency-locking as shown in Fig 4.3(a). Locking light is then passed through a fibre EOM before being delivered to the ultra-low-expansion cavity shown in 4.3(b). The rest of the light is delivered to 4.3(c). Here, light is split at a polarising beam splitter (PBS) cube. The reflected path of the PBS cube passes through a variable frequency AOM before being sent via an optical fibre to the main experimental table shown in 4.3(d). Two shutters (SRS - SR474) are implemented to prevent light leaking through the first order of the AOM from providing unwanted ac Stark shifts. On the main table, light is directed towards the molecules using a series of PBS cubes and wave plates. Transmitted light through the glass cell is collected on a photodiode for monitoring. 1.27(13) mW of laser light is applied to the molecules with a beam waist of 1.09(3) mm, providing a peak intensity of  $6.8(7) \times 10^2$  W/m<sup>2</sup>. This beam waist ensures negligible intensity variation across the sample. The AOM is used to pulse the light that illuminates the molecules. We send an 80 MHz signal from our Agilent MXG analogue signal generator which enables pulses of laser light with  $\sim 20$  ns resolution. When necessary, we change between horizontal and vertical probe polarisation, by simply adding or removing the final half-wave plate and PBS cube in the laser path before reaching the molecules in Fig. 4.3(d).

### 4.2.1 Scanning transfer cavity locking

We implement a scanning transfer cavity locking technique to frequency stabilise our home-built probe laser, constructing a setup based on the experimental design described in Subhankar *et.al* [176]. The prime motivation for utilising this technique was the relatively low cost of equipment compared to other locking schemes and a pragmatic approach regarding the degree of frequency stability that was necessary to undertake the planned experiments at the time.

As the name suggests, the locking method involves *transferring* the fre-

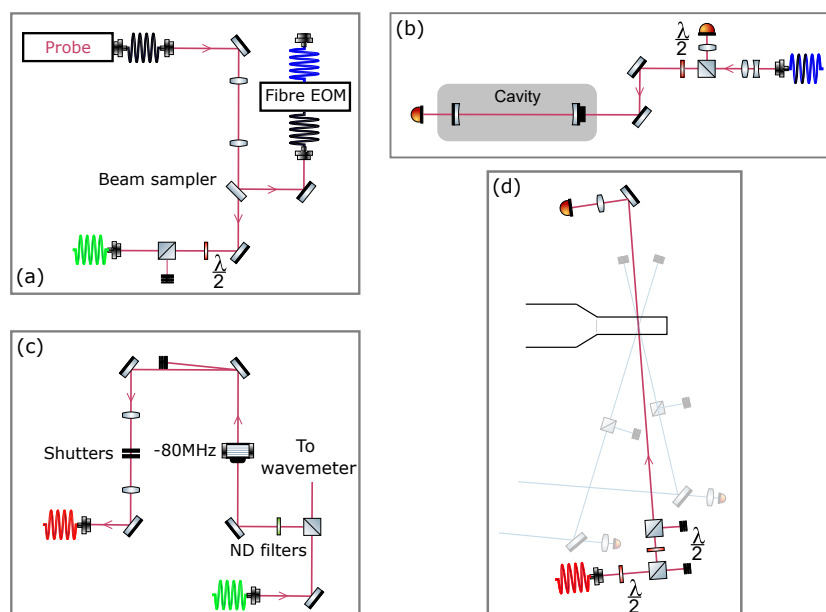


**Figure 4.3:** Experimental layout for spectroscopy measurements. (a) 1145nm Light picked off laser output for PDH locking. (b) PDH locking setup, constructed with the help of Fritz von Gierke (Masters student). (c) The beam split to provide a signal to the wavemeter and then passed through variable frequency AOM. (d) Experimental table setup. 1550 nm xODT setup presented faintly.

quency locking stability from one laser to another using a scanning optical cavity. Light from our Stokes laser is picked off before being transferred to the experimental table. The picked-off light is coupled into a Fabry-Pérot interferometer, or etalon (Toptica FPI 100) as shown in Fig. 4.2. The interferometer receives a saw tooth voltage signal produced by a Toptica MiniScan 102 scan generator, causing the cavity length to scan. We observe uniformly-spaced peaks in the etalon photo-diode signal from our Stokes laser. We then also couple our probe laser into the etalon, producing a second set of peaks. We work in a regime where a single cavity scan yields three peaks, two Stokes peaks with a single probe peak in between.

Given our Stokes laser when locked has a short-term stability of several 100 Hz [155], relative positional drifts we observe in neighbouring Stokes and probe etalon peaks are attributed to variations in the frequency of the probe laser. These relative peak positions form the basis of a proportion-integral-derivative (PID) feedback mechanism to frequency stabilise the probe laser.

The PID feedback is provided by an Arduino Due microcontroller with

an 84 MHz internal clock reference, onto which is uploaded code found at [176] and modified by members of the Fraunhofer Centre for Applied Photonics [177]. Input and output signals connecting to the microcontroller pass via a *shielding board*, a printed circuit board (PCB), components of which we have modified for our setup. Onto the shielding board, Bayonet Neill–Concelman (BNC) connectors are attached.

The microcontroller receives inputs from the saw-tooth scan TTL trigger and etalon photodiode signal. The rising edge of the TTL triggers an acquisition step. Referencing the TTL rising edge, the microcontroller acquires the time-position of the first three peaks from the etalon photodiode through its 12-bit analogue-to-digital converter.

The arrival time of a given etalon peak is simply given by

$$t_i = \frac{L_i}{\alpha}, \quad (4.9)$$

where  $L_i$  is length of the cavity and  $\alpha$  is the speed of the cavity scan. We can infer the relative frequency deviation of our probe laser by using the stable free spectral range (FSR) of the Stokes laser as a reference. Stokes and probe peak relative positions can be represented by the ratio

$$r = \frac{t_S - t_p}{t_{S'} - t_S} = \frac{L_S - L_p}{L_{S'} - L_S}, \quad (4.10)$$

where subscripts  $S$ ,  $S'$  and  $p$  refer to the first and second Stokes peaks and the probe peak detected by the microcontroller respectively. Forming this ratio eliminates any  $\alpha$  dependence. The servo loop acts to maintain a given value of  $r$ .

Outputs of the microcontroller are 3.3 V DAC pins with 12-bit resolution of which two are used in locking. One output provides the voltage to stabilise the value of  $r$  by adjusting the piezo frequency controller of our probe laser. The second is sent to the cavity piezo scan controller, producing an offset to the scan in an effort to prevent etalon peaks from drifting beyond our scan range due to environmental variations.

### 4.2.2 STCL testing

To test the efficacy of our STCL system, we perform a beat note measurement. We are unable to conduct a beat measurement using our the Stokes

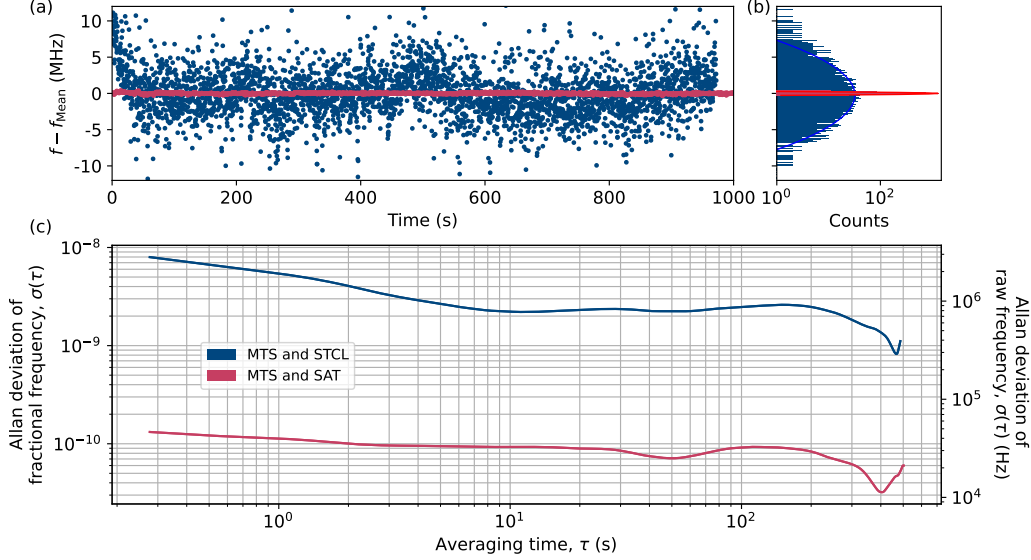


**Figure 4.4:** Beat note analysis. Blue and red data sets correspond to the MTS and STCL beat and the MTS and SAT beat respectively. (a) Frequency of beat minus mean frequency as a function of time observed on the frequency counter. (b) Histogram of the data in (a). (c) Allan deviation plot of the data in (a).

and probe lasers considering the relatively large difference in frequency. Instead, we use two  $\sim 852$  nm lasers that are used to provide the repump and cooling light for the Cs MOT. The cooling laser is locked using modulation transfer spectroscopy (MTS) [178] and the repump is locked using saturated absorption spectroscopy (SAT) [179] in typical experimental protocols. We replace the SAT locking scheme for the repump laser with STCL. Light from both lasers is coupled into the same fibre before being transferred to the experimental table. Reflected light off a PBS cube at the output of this fibre is then collected onto an EOT ET-3000 InGaAs photodiode, providing a beat signal.

A beat signal of  $\sim 30$  MHz is sent to a frequency counter (Tektronix FCA3003) with a frequency resolution of  $\sim 3 \times 10^{-5}$  Hz. We measure the beat frequency over a  $\sim 16$  minute period for both the SAT and STCL combinations. Results are presented in Fig. 4.4. When the repump laser is unlocked and the cooling is locked, we observe a drift in the beat signal of  $100.0(10)$  kHz a second (data not shown).

Fitting the resulting histograms in Fig. 4.4(b) with a Gaussian function,

we can extract an estimate of the short-term linewidths for the locks. The full-width half maxima (FWHM) are 0.101(4) MHz and 3.97(4) MHz for the MTS and SAT and MTS and STCL beats respectively. The Allan deviation of each data set are presented in Fig. 4.4(c).

After this beat measurement, we improve the STCL for experiments presented in chapter 5 by introducing a low-pass filter in the path between the etalon photodiode and the Arduino. This prevents noise in our photodiode signal causing false-positive detections of peaks. These unwanted detections inadvertently prompted the Arduino to output an incorrect signal to the laser piezo controller, causing jumps in laser frequency. We also optimise the voltage input to the laser from the Arduino by attenuating the Arduino's output. This increases the resolution of frequency adjustment to the laser that the Arduino is capable of performing.

We modify the Arduino code used in the STCL, inherited from the Fraunhofer Centre for Applied Photonics by exporting the positions of the peaks detected to a .csv file. The relative positions of the peaks are then converted into the frequency deviation of the laser. We produce a histogram of Vexum trapping laser frequency (discussed in chapter 5) over a  $\sim 12$  minute period. The standard deviation of the resulting histogram is 0.761(10) MHz.

### 4.2.3 PDH locking

Our Toptica 1145 nm laser frequency is referenced to an ultra-low expansion (ULE) cavity. This setup is presented in Fig 4.3(a) and (b). The locking scheme is similar to that which frequency stabilises the STIRAP lasers described in chapter 3 [155]. The experimental setup was constructed and optimised with the help of Fritz von Gierke (Masters student).

During high-resolution spectroscopy, we ascertain relative detunings of spectroscopic features by referencing to cavity modes. The cavity has a free spectral range at 1145nm of 1496.7551729(9) MHz and a line width of 40.490(5) kHz. Previous work on the equivalent STIRAP setup showed a 24-hour stability of the lasers on the order of  $\sim 100$  Hz [155]. We estimate a short-term linewidth of  $\sim 5$  kHz by analysing the error signal used for locking.

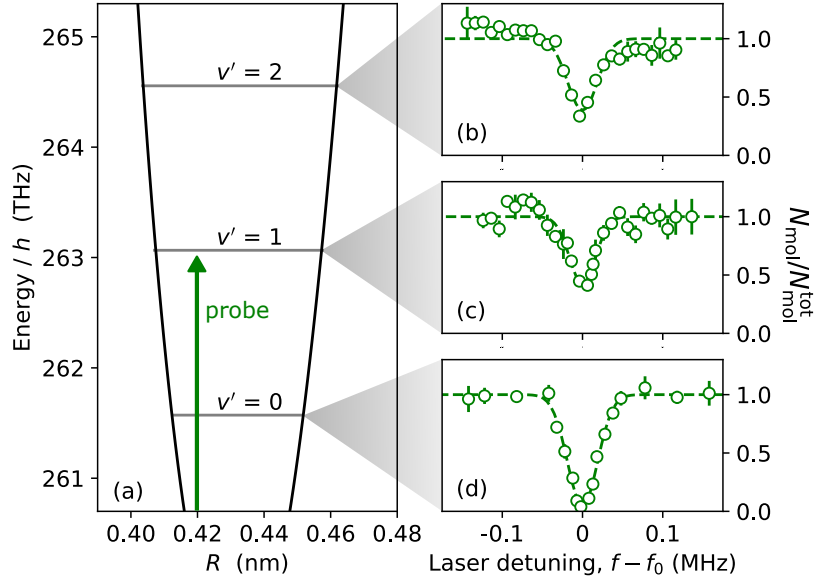


**Figure 4.5:** Vibrational structure of  $b^3\Pi_0$ . (a) Diagram of low-lying vibrational states of  $b^3\Pi_0$ . Data for plot provided by Jeremy Hutson’s group [180]. (b) Spectroscopy of  $X^1\Sigma^+(v'' = 0, N'' = 1) \rightarrow b^3\Pi_0(v' = 2, N' = 0)$ , (c)  $b^3\Pi_0(v' = 1, N' = 0)$  and (d)  $b^3\Pi_0(v' = 0, N' = 0)$  transitions from the spin-stretched  $N'' = 1$  state using horizontally polarised probe light. Horizontal axis given with respect to the centre of the fitting.

### 4.3 $b^3\Pi_0$ vibrational structure at 181.5 G

We investigate the low-lying vibrational states of the  $b^3\Pi_0$  potential by performing spectroscopy on the  $X^1\Sigma(v'' = 0, N'' = 1) \rightarrow b^3\Pi_0(v' = 0, 1, 2, N' = 0)$  transitions from the  $X^1\Sigma^+$  spin-stretched state, ( $N'' = 1, M_F'' = +6$ ). This transition is rotationally closed; there is only one allowed transition to  $b^3\Pi_0$  for each vibrational state given the selection rules  $\Delta N = \pm 1$  and  $\Delta M_F = \pm 1$ . First, we apply a resonant  $\sim 50 \mu\text{s}$   $\pi$ -pulse using our 1 GHz monopole antenna, coherently transferring our molecules from  $(0, +5)$  to  $(0, +6)$ . We illuminate our molecular sample with a  $500 \mu\text{s}$  square pulse of probe light from the laser locked to the ULE cavity. Light is polarised orthogonal to the quantisation axis with a peak intensity of  $6.8(7) \times 10^2 \text{ W/m}^2$  at the molecules. The natural linewidth of the  $b^3\Pi_0(v' = 0)$  state is expected to be  $\sim 20 \text{ kHz}$  [181] and the partial linewidth of the  $X^1\Sigma(v'' = 0, N'' = 1) \rightarrow b^3\Pi_0(v' = 0, N' = 0)$  transition is expected to be  $\sim 15.5 \text{ kHz}$  [172]. Converting the partial linewidth into a transition dipole moment using Eq. 4.2, we expect a Rabi frequency on the order of a few MHz with our peak intensity. A  $500 \mu\text{s}$  probe pulse on

$v'$	$f$ (GHz)
1	261570.03(6)
2	263063.77(6)
3	264553.72(6)

**Table 4.1:** Absolute  $X^1\Sigma^+(v'' = 0, N'' = 1) \rightarrow b^3\Pi_0(v', N' = 0)$  transition frequencies.

resonance should cause the molecule population to decrease to zero as the molecules decay to unobservable states.

After the probe pulse, we perform a second identical microwave  $\pi$ -pulse, transferring the population to  $(0, +5)$  and measure it. We then vary the probe laser frequency, observing a decrease in population as we resonantly couple to an excited state due to the effects of photon scattering. At this beam intensity, the resulting feature is power broadened. Therefore, we decrease the power by placing non-discriminant (ND) filters in the beam path as indicated in Fig. 4.3(c) and perform a subsequent spectroscopic measurement over the width of the feature observed at higher power. We then repeat this process until we are in a regime where features can be resolved but do not saturate. Results from this spectroscopy are presented in Fig. 4.5.

The absolute transition frequencies are presented in table. 4.1. Uncertainty is dominated by the uncertainty of our wavemeter. We determine the vibrational splitting to a greater precision by using the ULE cavity modes as a frequency reference. The energy splittings between  $v' = 0$  and  $v' = 1$  states and between  $v' = 1$  and  $v' = 2$  states are 1493.78241(3) GHz and 1489.96082(3) GHz respectively.

## 4.4 $b^3\Pi_0$ rotational structure at 181.5 G

We determine the effective rotational constant of the  $b^3\Pi_0(v' = 0, 1)$  states,  $\tilde{B}_{v'}$ , by performing the same sequence described in sec. 4.3 using vertically polarised probe light. Omitting or including the microwave pulses described in sec. 4.3 allows the  $N'' = 0 \rightarrow N' = 1$  or  $N'' = 1 \rightarrow N' = 2$  transitions to be accessed. Results of the spectroscopies of transitions coupling to the  $b^3\Pi_0(v' = 0)$  states are presented in Fig. 4.6.

By examining Eq. 2.3 <sup>1</sup>, we can use the relative frequencies of the transitions to determine  $\tilde{B}_{v'}$ . Splittings between rotational transitions are presented by the black double-headed arrows in Fig. 4.6(d). We can calculate the rotational constant of the excited state using <sup>2</sup>

$$\tilde{B}_{v'} = \frac{f_{1 \rightarrow 2} - f_{1 \rightarrow 0}}{6}, \quad (4.11)$$

where  $f_{1 \rightarrow 2}$  and  $f_{1 \rightarrow 0}$  are the transition frequencies for  $N'' = 1 \rightarrow N' = 2$  and  $N'' = 1 \rightarrow N' = 0$  respectively. To calculate an accurate value of the *true* rotational constant, we require a model of the hyperfine structure of  $b^3\Pi_0$  which is not currently understood.

As an estimate of the effective rotational constant, we can consider the mean position of the hyperfine features presented in Fig. 4.6. The uncertainty in  $\tilde{B}_{v'}$  is dominated by the hyperfine splitting. We find that  $\tilde{B}_{v'=0} = 516.4(12)$  MHz and  $\tilde{B}_{v'=1} = 515.5(9)$  MHz respectively. This agrees well with the  $\tilde{B}_{v'=0} = 510$  MHz rotational constant predicted in [172].

#### 4.4.1 Zeeman shifts of the excited state

We investigate Zeeman shifts in the excited state by performing spectroscopy of transitions as a function of magnetic field, utilising the same experimental procedure conducted in section 4.3. Results are presented in Fig. 4.7. We assume at this magnetic field regime, the Zeeman shifts are linear.

Using our extensive knowledge of the  $X^1\Sigma^+$  hyperfine structure and their respective Zeeman shifts from equation 2.8, we extract  $b^3\Pi_0$  state magnetic moments,  $\mu$ , by comparing ground state Zeeman shifts to shifts in transition frequencies as a function of magnetic field. These results are presented in tables 4.2, 4.3 and 4.4. We note that the  $b^3\Pi_0(v' = 0, 1, 2, N'' = 0)$  states possess the same magnetic moment within uncertainty.

#### 4.4.2 HF structure overview

We perform a comprehensive investigation of the hyperfine structure of  $b^3\Pi_0(v' = 0, 1, 2)$  at 181.5 G by implementing the same procedure described in section 4.3 for probe light polarised both vertically and horizontally at the

<sup>1</sup>We ignore the centrifugal distortion as we are investigating low-lying rotational states.

<sup>2</sup>The rotational constant can also be extracted in other manners, however this method yields the smallest uncertainty. Other calculations of rotational constant agree within error.

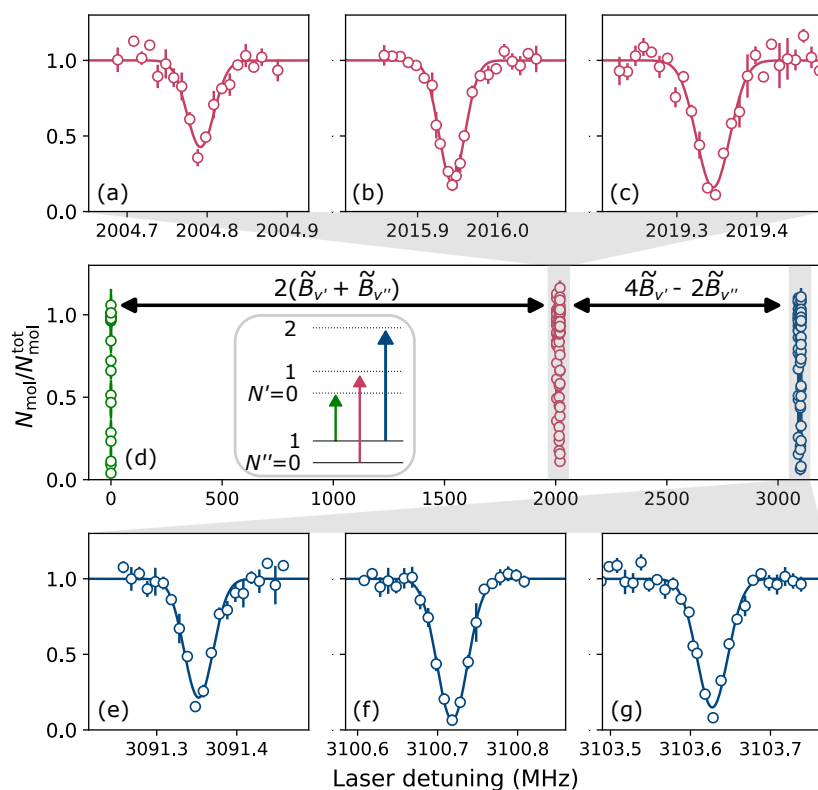


**Figure 4.6:** Rotational structure of  $b^3\Pi_0(v' = 0)$ . Laser detuning given with respect to the  $N'' = 1 \rightarrow 0$  transition. (a-c) Spectroscopy of  $N'' = 0 \rightarrow N' = 1$  and (e-g)  $N'' = 1 \rightarrow N' = 2$  transitions using vertically polarised light. (d) Overview of rotational structure of  $b^3\Pi_0(v' = 0)$ . Green, red and blue data correspond to  $N'' = 1 \rightarrow N' = 0$ ,  $N'' = 0 \rightarrow N' = 1$  and  $N'' = 1 \rightarrow N' = 2$  transition respectively. Green data presented in Fig. 4.5(d). Energy splitting between rotational transitions presented as black double-headed arrows. Inset presents relevant rotational energy levels.

molecules.

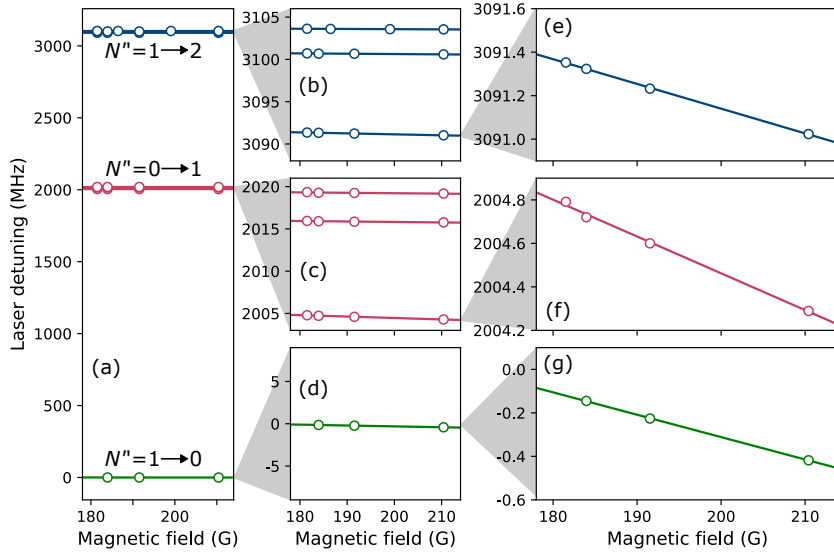


**Figure 4.7:** Zeeman shifts in  $X^1\Sigma^+(v'' = 0) \rightarrow b^3\Pi_0(v' = 0)$  transitions shown in Fig. 4.6. Green, red and blue lines correspond to transition frequencies of  $N'' = 1 \rightarrow N' = 0$ ,  $0 \rightarrow 1$  and  $1 \rightarrow 2$  respectively. Laser detuning given relative to the  $N'' = 1 \rightarrow N' = 0$  transition frequency at 181.5 G. Zeeman shifts show for different plot laser detuning ranges, (a) 3500 MHz, (b-d) 18 MHz and (e-g) 0.7 MHz.

The narrowest feature we were able to observe was  $\sim 13$  kHz, although all widths of features fell into the a 13 to 20 kHz range. Considering the  $\sim 5$  kHz short-term linewidth of the PDH locking scheme, we can attribute these widths to molecular transition linewidths.

In tables 4.2, 4.3 and 4.4, we also give the peak intensity of probe light used in each instance. We attribute the power difference in obtaining spectroscopies for different transitions to relative transition strengths.

We performed spectroscopy using both horizontal and vertically polarised probe light for  $X^1\Sigma^+(v'' = 0, N'' = 0, 1) \rightarrow b^3\Pi_0(v' = 0, N' = 0, 1, 2)$  transitions. However, we only performed spectroscopy on the  $X^1\Sigma^+(v'' = 0, N'' = 0, 1) \rightarrow b^3\Pi_0(v' = 1, 2)$  transitions using vertically polarised light and only investigated the  $X^1\Sigma^+(v'' = 0, N'' = 1) \rightarrow b^3\Pi_0(v' = 2)$  transition for  $v' = 2$ . These transitions are useful for modelling the structure  $b^3\Pi_0$  and for possibly informing the rotational magic detunings outlined in [172].

$$v' = 0$$

$N'' \rightarrow N'$	$\theta$ ( $^\circ$ )	$\Delta f$ (MHz)	$I_{\text{Peak}}$ (mW/m <sup>2</sup> )	$Z$ (kHz/G)	$\mu$ ( $\mu_N$ )
1 $\rightarrow$ 0	90	0	2.9(2)	-10.29(12)	-18.82(16)
0 $\rightarrow$ 1	0	2004.7916(18)	0.70(5)	-16.33(14)	-26.7(2)
0 $\rightarrow$ 1	0	2015.9430(9)	7.0(5)	-5.05(5)	-11.9(7)
0 $\rightarrow$ 1	0	2019.345(2)	$2.3(2) \times 10^3$	-3.58(12)	-10.01(16)
1 $\rightarrow$ 2	0	3091.3523(14)	7.5(5)	-11.37(16)	-20.2(2)
1 $\rightarrow$ 2	0	3100.7183(8)	7.5(5)	-3.8(6)	-10.3(7)
1 $\rightarrow$ 2	0	3103.6272(11)	$7.5(5) \times 10^2$	-2.4(3)	-8.4(3)
0 $\rightarrow$ 1	90	2005.606(9)	$4.3(4) \times 10^3$	-	-
0 $\rightarrow$ 1	90	2011.7140(15)	$1.36(14) \times 10^4$	-	-
0 $\rightarrow$ 1	90	2015.607(3)	7.7(8)	-	-
0 $\rightarrow$ 1	90	2015.789(2)	7.7(8)	-	-
0 $\rightarrow$ 1	90	2022.7573(11)	1.28(13)	-	-
1 $\rightarrow$ 2	90	3089.983(4)	$4.3(4) \times 10^3$	-	-
1 $\rightarrow$ 2	90	3092.062(10)	$1.36(14) \times 10^3$	-	-
1 $\rightarrow$ 2	90	3093.774(5)	$4.3(4) \times 10^5$	-	-
1 $\rightarrow$ 2	90	3095.149(10)	$4.3(4) \times 10^5$	-	-
1 $\rightarrow$ 2	90	3096.695(10)	$1.00(10) \times 10^5$	-	-
1 $\rightarrow$ 2	90	3097.027(8)	$1.00(10) \times 10^5$	-	-
1 $\rightarrow$ 2	90	3100.674(2)	1.36(14)	-	-

**Table 4.2:** Features identified in spectroscopy of  $X^1\Sigma^+(v'' = 0) \rightarrow b^3\Pi_0(v' = 0)$  transitions. Frequency is given with respect to the  $N'' = 1 \rightarrow N' = 0$  transition.  $I_{\text{Peak}}$  is the peak intensity used to perform the spectroscopy on the transition in each case.  $Z$  is the Zeeman shift of the transition and  $\mu$  is the corresponding magnetic moment of the excited state derived from the Zeeman shift.

## 4.5 Linewidths

### 4.5.1 Partial linewidths

We characterise the transition dipole moments (TDMs) for the  $v'' = 0, N'' = 0 \rightarrow v' = 0, 1, 2, N' = 1$  transitions by measuring the off-resonant light shifts in the  $v'' = 0, N'' = 0$  state. The change in energy of the  $v'' = 0, N'' = 0$  state illuminated by probe of intensity  $I$  is given by [182]

$$v' = 1$$

$N'' \rightarrow N'$	$\theta$ ( $^\circ$ )	$\Delta f$ (MHz)	$I_{\text{Peak}}$ (mW/m $^2$ )	$Z$ (kHz/G)	$\mu$ ( $\mu_N$ )
1 $\rightarrow$ 0	90	0	2.83(8)	-10.3(2)	-18.8(3)
0 $\rightarrow$ 1	0	2003.596(2)	3.7(2)	-15.68(8)	-25.88(10)
0 $\rightarrow$ 1	0	2014.197(2)	$1.13(11) \times 10^3$	-6.37(8)	-13.67(10)
0 $\rightarrow$ 1	0	2014.465(2)	14.3(3)	-4.5(2)	-11.3(2)
1 $\rightarrow$ 2	0	3087.249(2)	118(5)	-11.16(13)	-19.96(17)
1 $\rightarrow$ 2	0	3096.148(2)	$3.7(2) \times 10^2$	-4.6(2)	-11.3(2)
1 $\rightarrow$ 2	0	3096.370(2)	3.7(2)	-3.26(5)	-9.60(6)

**Table 4.3:** Features identified in spectroscopy of  $X^1\Sigma^+(v'' = 0) \rightarrow b^3\Pi_0(v' = 1)$  transitions. Frequency given with respect to the  $N'' = 1 \rightarrow N' = 0$  transition.  $I_{\text{Peak}}$  is the peak intensity used to perform the spectroscopy on the transition in each case.  $Z$  is the Zeeman shift of the transition and  $\mu$  is the corresponding magnetic moment of the excited state derived from the Zeeman shift.

$$v' = 2$$

$N'' \rightarrow N'$	$\theta$ ( $^\circ$ )	$\Delta f$ (MHz)	$I_{\text{Peak}}$ (mW/m $^2$ )	$Z$ (kHz/G)	$\mu$ ( $\mu_N$ )
1 $\rightarrow$ 0	90	0	12.9(5)	-10.0(2)	-18.4(3)

**Table 4.4:**  $X^1\Sigma^+(v'' = 0, N'' = 1) \rightarrow b^3\Pi_0(v' = 2, N'' = 0)$  transition.  $I_{\text{Peak}}$  is the peak intensity used to perform the spectroscopy.  $Z$  is the Zeeman shift of the transition and  $\mu$  is the corresponding magnetic moment of the excited state derived from the Zeeman shift.

$$\delta E_{v''=0, N''=0} = \frac{3\pi c^2 \Gamma_{v'}}{2\omega_0^3 \Delta} I, \quad (4.12)$$

where  $\Delta$  is the laser detuning with respect to the transition. By measuring light shifts in proximity to each transition we can determine the partial linewidth and corresponding TDM using Eq. 4.2.

We examine light shifts in the  $v'' = 0, N'' = 0$  state,  $\delta E_{v''=0, N''=0}$ , using the STIRAP two-photon transfer sequence described in section 3.3. We assume shifts in transition frequency only arise from shifts in energy of the  $v'' = 0, N'' = 0$  state, noting that the probe light is far detuned from transitions from the excited or Feshbach states. We set the intensity of the light to

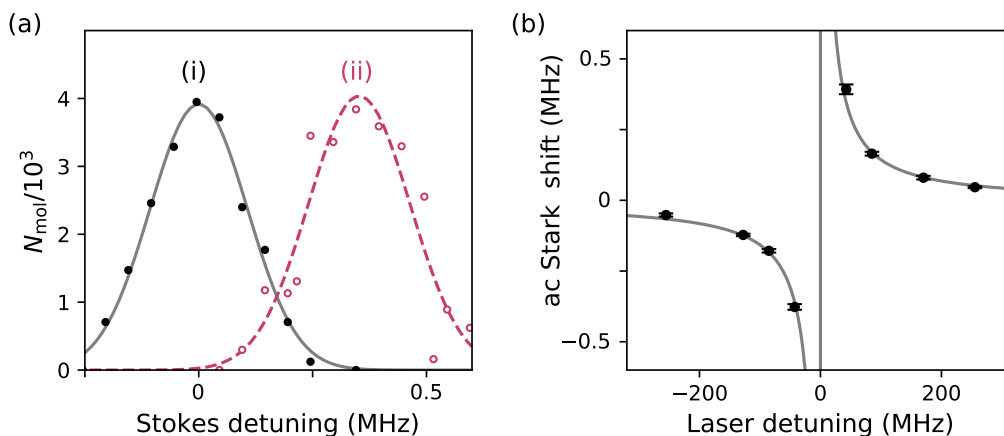


**Figure 4.8:** Determining the transition dipole moment of electronic transitions. (a) Effect of ac Stark shifts on the  $v'' = 0, N'' = 0$  state. Spectroscopy using Stokes laser (i) in free space and (ii) in the presence of probe light +30 MHz detuned from the  $v'' = 0, N'' = 0 \rightarrow v' = 0, N' = 1$  transition. (b) Light shifts in  $v'' = 0, N'' = 0$  as a function of probe laser detuning with respect to the  $v'' = 0, N'' = 0 \rightarrow v' = 0, N' = 1$  transition.

be  $3.5(4) \times 10^4 \text{ W m}^{-2}$  using 1.5(1) mW, focused to a 168(5)  $\mu\text{m}$  waist such that the light shifts are significant and measurable over a frequency range of  $\sim 100$  MHz. The homebuilt probe laser is used for this measurement and is frequency-stabilised using STCL. Probe light is only applied during the second STIRAP sequence used in the detection stage of our experiments and is horizontally polarised at the molecules.

We perform spectroscopy of the Stokes transition by scanning the frequency of the Stokes laser and measuring molecule population. Peaks in the molecule population correspond to the Stokes laser becoming resonant with the transition are shown in Fig 4.8(a)(i). Data is fitted with a Gaussian function and the centre of the fit is extracted with a  $\sim 10$  kHz uncertainty.

In the presence of probe light, we observe shifts in the Stokes transition as shown in Fig. 4.8(a)(ii). Light shifts become greater the closer in proximity the probe frequency is to a  $X \rightarrow b$  transition as shown in Eq. 4.12. We repeat the spectroscopy for various probe laser detunings, producing the data presented in Fig. 4.8(b). The difference in noise between data sets shown in Fig. 4.8(a)(i) and Fig. 4.8(a)(ii) is attributed to inhomogeneous intensity of probe light across the molecular population. This effect is exacerbated at smaller laser detunings. Data is then fitted with Eq. 4.12, with specific

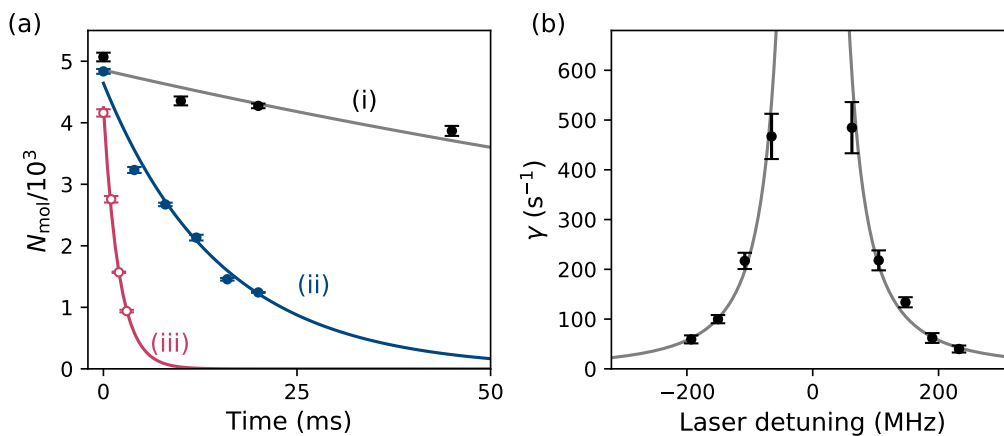


**Figure 4.9:** Characterising total linewidths. (a) Lifetime of  $v'' = 0, N'' = 0$  molecules in the 1550 nm xODT (i) without probe light, (ii) illuminated by probe light +90 MHz and (iii) +75 MHz detuned from the  $v'' = 0, N'' = 0 \rightarrow v' = 0, N' = 1$  transition. (b)  $v'' = 0, N'' = 0$  molecule loss rate in the presence of probe light as a function of detuning from the  $v'' = 0, N'' = 0 \rightarrow v' = 0, N' = 1$  transition.

details of the fitting procedure given in section 4.9. Similar methods are used to determine partial linewidths of the  $v'' = 0, N'' = 0 \rightarrow v' = 1, N' = 1$  and  $v'' = 0, N'' = 0 \rightarrow v' = 2, N' = 1$  transitions. Our best estimates of the linewidths are  $\Gamma_0 = 11.1(1.2)$  kHz,  $\Gamma_1 = 7.2(9)$  kHz and  $\Gamma_2 = 2.2(2)$  kHz. These correspond to transition dipole moments of  $\mu_0 = 0.58(3)$ ,  $\mu_1 = 0.46(3)$  and  $\mu_2 = 0.253(14)$  Debye respectively.

## 4.5.2 Total linewidths

The excited state linewidth  $\Gamma_v^e$ , depends on all available decay pathways from the excited state, and so will, in general, be greater than the partial linewidth measured in section. 4.5.1. We investigate the transition  $v'' = 0, N'' = 0 \rightarrow v' = 0, 1, N' = 1$ . This transition is not rotationally closed. Molecules that are excited to  $v' = 0, N' = 1$  can decay to either  $N'' = 0$  or  $N'' = 2$  states in  $X^1\Sigma^+$ . Moreover,  $M_N$  may not be conserved, giving only a one-third probability of decay to  $N'' = 0$  without considering possible decay to other vibrational states or the  $a^3\Sigma$  electronic state. We ignore the decay channels to the  $a^3\Sigma$  state as they account for <1% of decays from the low-lying vibrational states of  $b^3\Pi_0$  [183].

We determine the excited state linewidth,  $\Gamma_0^e$ , of the  $v' = 0, N' = 1$  state by observing the effects of photon scattering near the  $v'' = 0, N'' = 0 \rightarrow$

$v' = 0, N' = 1$  transition using ground state molecules confined to the xODT. First, we observe the population of  $v'' = 0, N'' = 0$  molecules confined in the xODT as a function of time. In the absence of probe light, molecules in the dipole trap are lost owing to collisional processes [184, 185]. This yields a background loss rate in our experiment presented by the data in Fig. 4.9(a)(i).

Maintaining the same probe laser parameters used in section 4.5.1, we apply horizontally polarised probe light to molecules in the xODT and investigate the lifetime of molecules for a range of probe laser detunings. The probe laser increases the loss rate in molecule population due to photon-scattering of probe light when the laser is tuned close to the  $v'' = 0, N'' = 0 \rightarrow v' = 0, N' = 1$  transition. This effect becomes greater at smaller laser detunings as shown in Fig. 4.9(a)(ii) and (iii). Using  $\Gamma_0$  obtained from section 4.5.1, we fit the photon scattering rate as a function of laser detuning shown in Fig. 4.9(b) with [45]

$$\gamma_{\text{sc}} = \frac{3\pi c^2}{2\hbar\omega_0^3} \frac{\Gamma_{v'}\Gamma_{v'}^e}{\Delta^2} I \quad (4.13)$$

and obtain an excited state linewidth,  $\Gamma_0^e = 20(3)$  kHz. We repeat the experiment for the  $v'' = 0, N'' = 0 \rightarrow v' = 1, N' = 1$  transition which yields  $\Gamma_1^e = 103(15)$  kHz.

## 4.6 Finding the rotationally magic detuning

Using spectroscopy of microwave transitions between different  $X^1\Sigma^+(v'' = 0)$  rotational states, we coarsely map out the differential ac Stark shifts between pairs of  $X^1\Sigma^+(v'' = 0)$  rotational states in the presence of light tuned between  $X \rightarrow b$  electronic transitions. We then increase the probe beam intensity and concentrate our efforts around the regions where the ac Stark shift in rotational transitions is eliminated, identifying rotationally magic detunings.

### 4.6.1 Coarse spectroscopy

We choose to interrogate the transition  $(N'' = 0, M_F'' = +5) \rightarrow (1, +6)$  so that all spins remain stretched such that  $M_N''$  is a good quantum number for both states<sup>3</sup>. For states that are not spin-stretched, the only good quantum

<sup>3</sup>At the 181.5 G magnetic field used in our experiments,  $m_{\text{Rb}}''$  and  $m_{\text{Cs}}''$  are not generally good quantum numbers as the magnetic field is not high enough to fully decouple the nuclear spins.

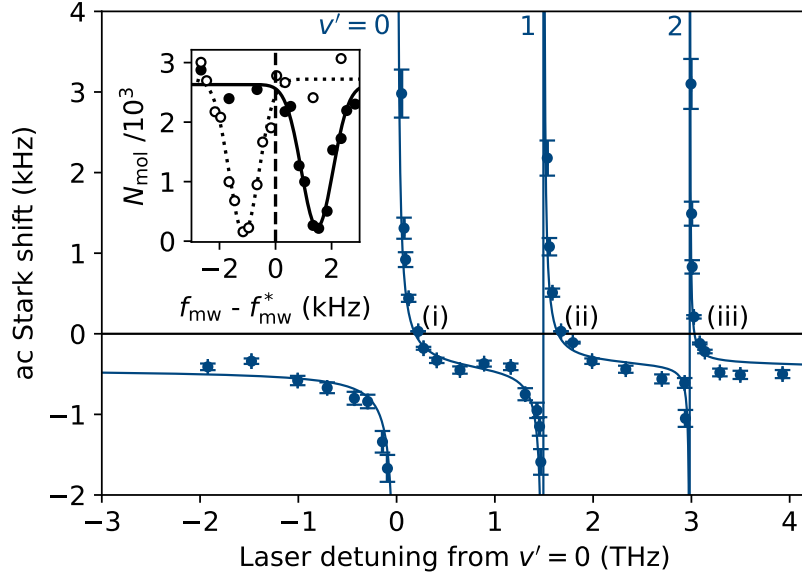


**Figure 4.10:** Coarse spectroscopy. (a) ac Stark shift of the  $(N''=0, M_N''=+5) \rightarrow (1, +6)$  transition as a function of probe laser detuning. The solid line indicates the expectation from Eq. 4.1 with constants fixed at the values found in section 4.9. Inset, example spectroscopy of the rotational transition, observed as variation in the molecule number  $N_{\text{mol}}$  as a function of microwave frequency  $f_{\text{mw}}$ , for a negative (empty circles) and positive (filled circles) ac Stark shift. Here, the microwave frequency axis is plotted with respect to the transition frequency measured in the absence of probe light,  $f_{\text{mw}}^* = 980.38566(3)$  MHz.

numbers are  $N''$  and  $M_F'' = M_N'' + m_{\text{Rb}}'' + m_{\text{Cs}}''$  [136].

To perform spectroscopy, we pulse on microwaves for 1 ms, with the microwave power set to approximately perform a  $\pi$  pulse when tuned to resonance. This causes an apparent loss of molecules as the population is coherently transferred into the rotationally excited state where they can no longer be detected. We then measure the number of molecules remaining as a function of the microwave frequency and fit the result with a Gaussian function to extract the centre of the loss feature. Typical uncertainties in the centre of the loss features are  $<100$  Hz.

To measure the ac Stark shift we compare the transition energy measured with and without the probe light. The probe light is produced by the home-built laser and horizontally polarised at the molecules with a peak intensity of  $\sim 10^6 \text{ W m}^{-2}$  (approximately 10 mW of laser power focused to an  $80 \mu\text{m}$

waist). At this stage, we do not actively stabilise the frequency of the probe laser, and we estimate a passive stability of  $\pm 100$  MHz during this measurement.

The observed ac Stark shift is shown as a function of the probe laser detuning in Fig. 4.10. We observe poles where the differential polarisability changes sign indicating the locations of transitions to  $v' = 0, 1, 2$ . Magic detunings for the  $(0,+5) \rightarrow (1,+6)$  transition are found where the ac Stark shift becomes zero. This occurs three times over the frequency range we have investigated at detunings marked with (i), (ii) and (iii) in Fig. 4.10.

## 4.6.2 High-resolution spectroscopy

To more precisely determine the rotationally magic laser frequencies we increase the intensity of the probe light to maximise the effects of ac Stark shifts. Here, we set the intensity to be  $\sim 10^7$  W m $^{-2}$  by reducing the waist to 20  $\mu$ m.

In Fig. 4.11(a), we present ac Stark shift measurements around the magic condition closest to  $v' = 0$  for the three rotational transitions that connect the spin-stretched states  $(0,+5)$  and  $(3,+8)$ . In addition, we have also measured ac Stark shifts for the non-spin stretched transition from the stretched  $N'' = 0$  state to the lowest energy  $N'' = 1, M_F'' = 5$  state. This is composed of an admixture of spins in the  $|N'', M_N'', m_{\text{Rb}}'', m_{\text{Cs}}''\rangle$  basis

$$0.924 |1, 0, \frac{3}{2}, \frac{7}{2}\rangle - 0.370 |1, 1, \frac{1}{2}, \frac{7}{2}\rangle + 0.091 |1, 1, \frac{3}{2}, \frac{5}{2}\rangle,$$

and is therefore predominantly  $M_N'' = 0$  in character.

For each transition, we show the ac Stark shift as a function of the probe laser frequency for light polarised either parallel or perpendicular to the quantisation axis. The results for each combination of transition and polarisation are fitted with a straight line to determine where the ac Stark shift becomes zero. For the measurements presented here, at 188(4) GHz the differential ac Stark shift between each pair of rotational states is zero, presented in Fig. 4.11(a) as the detuning at which all lines cross. As such, we do not resolve a dependence of the magic condition on the states or laser polarisation in this work. However, we note that in chapter 5 where we perform Ramsey interferometry using trapped samples, we were able to resolve small varia-

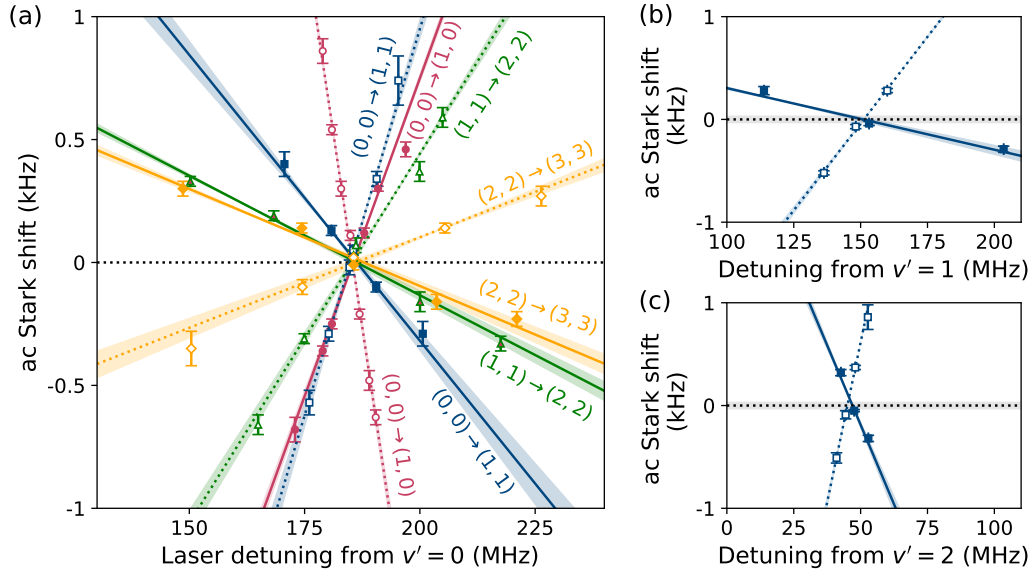


**Figure 4.11:** ac Stark shifts in  $X^1\Sigma^+$  microwave transitions as a function of probe light detuning around magic detunings. (a) ac Stark shifts for various transitions labelled by the dominant  $(N'', M_N'')$  components around the magic detuning close to the  $X^1\Sigma^+(v' = 0) \rightarrow b^3\Pi_0(v' = 0)$  transition. In each case, empty (filled) circles indicate measurements with vertically (horizontally) polarised light. Each data set is fit with a linear function with uncertainties given as the shaded regions. (b,c) Equivalent measurements focusing only on the  $N'' = 0, M_N'' = 0 \rightarrow N'' = 1, M_N'' = 1$  transition around the magic conditions closest to transitions to  $b^3\Pi_0(v' = 1, 2)$ . Smaller detuning ranges are investigated compared to Fig. 4.10 due to larger intensity of probe light.

tions in magic detunings depending on the target transition.

We have also examined the magic conditions near transitions to the  $v' = 1, 2$  states as illustrated in Fig. 4.11(b) and (c). We present the ac Stark shift in the  $(0,+5) \rightarrow (1,+6)$  transition as a function of probe detuning with vertical and horizontal laser polarisation. In each case, we reference the probe detuning to the closest vibrational transition. We observe that the magic condition is satisfied at lower detunings from higher vibrational transitions. This corresponds to magic trapping potentials that are more sensitive to noise in trap light frequency.

## 4.7 Ramsey interferometry at rotationally magic detuning

To confirm coherence between different rotational states is maximised at the magic detuning, we perform Ramsey interferometry in the presence of probe light. For this, we use the magic condition closest to the  $X^1\Sigma^+(v'' = 0) \rightarrow b^3\Pi_0(v' = 0)$  transition. We keep the intensity of the light at  $10^7 \text{ W cm}^{-2}$  and set the polarisation to be horizontal. To perform Ramsey interferometry, we first apply a resonant  $\pi/2$  pulse (Rabi frequency of 4.3(1) kHz) in free space, creating an equal superposition of (0,+5) and (1,+6) states. We then switch on the probe light, which is frequency-stabilised with the STCL. The state is allowed to freely evolve for 1 ms, before the light is switched off and a second  $\pi/2$  pulse is applied with a variable phase relative to the first pulse. We observe a Ramsey fringe in the number of molecules detected in the  $N'' = 0$  state as a function of the phase of the second microwave pulse. The sequence is repeated for various probe laser detunings. The contrast of the Ramsey fringes reaches a maximum when the light is tuned to magic, as shown in Fig. 4.12(a).

By fixing the  $\pi/2$  pulses in phase, we also observe Ramsey fringes as oscillations in the number of molecules in  $N'' = 0$  as a function of evolution time,  $T$ , in the presence of probe light. The frequency of these oscillations is equal to the detuning of the microwaves from resonance. We increase the Rabi frequency of the microwaves to 8.1(1) kHz to enable transfer with high fidelity with the microwave frequency detuned by  $\sim 3$  kHz. We show the time evolution of the Ramsey fringes in Fig. 4.12 when (c) -47.1 GHz detuned from the rotationally magic detuning, and (d) at magic. In each plot, the dotted line indicates the number of molecules remaining without the Ramsey sequence; we observe loss of molecules over time as they fall out the detection region due to gravity. When detuned from the rotationally magic detuning by -47.1 GHz, we observe a coherence time of 0.37(5) ms. When the light is tuned to magic, however, the coherence time is significantly enhanced with no discernible loss of coherence over the 2.8 ms interrogation time.

## 4.8 STIRAP magic

Tuning the laser frequency between transitions to the  $b^3\Pi_0$  potential allows us to set the polarisability of a single rotational state in the  $X^1\Sigma^+$  potential to an arbitrary value. As an example, we show how differential ac Stark shifts between the  $N'' = 0$  state and the weakly-bound state to which it is

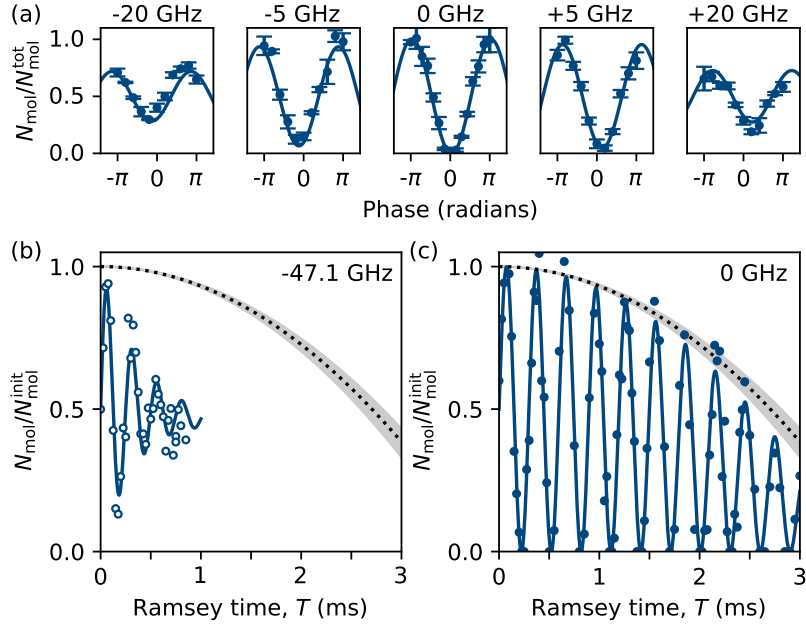


**Figure 4.12:** Ramsey interferometry in the probe light. The probe intensity is  $\sim 10^7 \text{ W cm}^{-2}$  and the light is linearly polarised perpendicular to the magnetic field. (a) Interferometry using a superposition of the  $N'' = 0, M_N'' = 0$  and  $N'' = 1, M_N'' = 1$  states for various probe laser frequencies. The Ramsey time is fixed at  $T = 1 \text{ ms}$ . Ramsey fringes are observed as a variation in the molecule number  $N_{\text{mol}}$  as a function of the phase difference between the  $\pi/2$  pulses.  $N_{\text{mol}}$  is plotted as a fraction of the total number  $N_{\text{mol}}^{\text{tot}}$ . The detuning of the probe laser from magic is given above each panel. (b,c) Ramsey fringes observed as oscillations in  $N_{\text{mol}}$  as a function of time with the probe (b) detuned from magic by  $-47.1 \text{ GHz}$  and (c) at magic. Here,  $N_{\text{mol}}$  is plotted as a fraction of the molecule number at  $T = 0$ ,  $N_{\text{mol}}^{\text{init}}$ . Black dotted lines show the loss of molecules over the Ramsey time due to untrapped molecules leaving the detection region.

coupled during STIRAP can be eliminated. Such ac Stark shifts can otherwise drastically reduce the efficiency of the STIRAP [115]. The polarisability of this weakly-bound state is  $\alpha' = h \times 68.5 \text{ Hz W}^{-1} \text{ cm}^2$ , simply given by the sum of the atomic polarisabilities. We assume that this is independent of the laser frequency as the light is far detuned from nearby transitions from this state. Our goal therefore is to set the laser frequency at a detuning where the  $N'' = 0$  polarisability is equal to this value.

We measure the light shift between these states using STIRAP in the presence of probe light with a peak intensity of  $\sim 10^8 \text{ W m}^{-2}$ , achieved using

a  $34\ \mu\text{m}$  waist in combination with a tapered amplifier. We keep the frequency of the pump laser constant, vary the Stokes laser, and observe a peak in the molecule number when the STIRAP efficiency is maximised.

We measure the optimum Stokes detuning with and without the probe light to determine the light shift of the ground state relative to the weakly-bound Feshbach state. We fit each set of results using Eq. 4.1 with the linewidths of the neighboring transitions and the background polarisabilities as free parameters. This yields an estimate of the STIRAP magic detunings between the first and second lowest-energy pairs of adjacent electronic transitions as  $+0.45(12)$  THz and  $+0.6(3)$  THz respectively.

## 4.9 Analysis of results

We judiciously combine our experimental results in a way to accurately calculate transition linewidths and background polarisabilities. First, using our rotational and STIRAP magic detuning results as fixed parameters, we fit the coarse rotational transition light shift results presented in Fig. 4.10 with equation 4.1. This fitting allows for the extraction of the ratio of transition linewidths which dictate the magic detunings. The absolute values of the transition linewidths are calculated by fitting all the ac Stark shift and photon scattering data sets for each transition simultaneously, fixing the ratio of the partial linewidths. This fitting procedure is the source of the linewidths quoted in 4.5.1 and 4.5.2. Finally, we refit the the coarse rotational transition light shift results with the magic detunings and the linewidths as fixed parameters. Values of the parallel and perpendicular background polarisabilities of  $\alpha_{\perp}^{\text{bg}} = 49(7)\ \text{HzW}^{-1}\text{cm}^2$  and  $\alpha_{\parallel}^{\text{bg}} = 125(9)\ \text{HzW}^{-1}\text{cm}^2$  respectively are then extracted from this fitting. These background polarisability values agree very well with the predicted  $\alpha_{\perp}^{\text{bg}} = 34\ \text{HzW}^{-1}\text{cm}^2$  and  $\alpha_{\parallel}^{\text{bg}} = 127\ \text{HzW}^{-1}\text{cm}^2$  [172]. Results from our fittings are presented in table 4.5.

Relative gradients of light shift spectroscopy of magic conditions as presented in Fig. 4.11(b-c) are not consistent with expectation. The light shift should have a greater sensitivity to detuning for magic conditions at higher absolute probe laser frequencies owing to smaller relative detuning positions. We attribute this inconsistency to day-to-day drifts in laser intensity over the course of our measurements.

$v'$	Theory		This work		
	$f$ (THz)	$\Gamma_{v'}$ (kHz)	$f$ (THz)	$\Gamma_{v'}$ (kHz)	$\Gamma_{v'}^e$ (kHz)
0	261.533	15.5	261.571 87(6)	11.1(1.2)	20(3)
1	263.036	6.9	263.065 63(6)	7.2(9)	103(15)
2	264.533	1.5	264.555 60(6)	2.2(2)	-

**Table 4.5:** Transition frequencies, partial linewidths and total linewidths. Theoretical predictions taken from [172].

## 4.10 Summary

To summarise, we have performed high-resolution spectroscopy of the  $X^1\Sigma^+ \rightarrow b^3\Pi_0(v' = 0, 1, 2)$  transitions, resolving hyperfine states in the  $b^3\Pi_0$  potential. We identified the absolute frequencies of the electronic transitions to different  $v'$  states and, using the locking ultra-low expansion cavity as a frequency reference, determined relative transition frequencies to  $\sim 30$  kHz precision.

Using our relative transition frequencies, we determined the rotational energy splittings for the low-lying vibrational states of the  $b^3\Pi_0$  potential. We extract effective rotational constants for  $v' = 0$  and  $v' = 1$  as 516.4(12) MHz and 515.5(9) MHz respectively. We have determined the partial linewidths for the  $X^1\Sigma^+(v'' = 0, N'' = 0) \rightarrow b^3\Pi(v' = 0, 1, 2, N' = 1)$  transitions and total linewidths of the  $b^3\Pi(v' = 0, 1, 2, N' = 1)$  states by observing ac Stark shifts in the  $X^1\Sigma^+(v'' = 0, N'' = 0)$  state and the effects of photon scattering in the presence of probe light respectively. The rotationally magic and magic STIRAP detunings have been identified between the low-lying vibrational states of  $b^3\Pi_0$ .

We have proved that using the rotationally magic detuning engineers long-lived coherence times between different rotational states by performing a series of Ramsey sequences, providing a fantastic outlook for utilising this detuning for optical trapping of RbCs in quantum science architecture.

# Chapter 5

## Magic Trapping and Dipole-Dipole Interactions

### 5.1 Introduction

Accessing and controlling dipole-dipole interactions between diatomic molecules are key to realising their prospects as platforms for encoding and entangling qubits [95–97, 186], qudits [120], psuedo-spins [17, 32, 33, 36, 38, 88, 187, 188] and synthetic dimensions [189–191]. So far, dipolar interactions have been harnessed to investigate spin-1/2 XY models in a range of geometries [43, 44, 85, 192, 193] and to engineer iSWAP gates that prepare pairs of tweezer-confined molecules in maximally-entangled Bell states [192, 193]. The energy scales associated with dipolar interactions are of order  $\sim 1$  kHz given typical experimental parameters, meaning quantum states must remain coherent over many milliseconds in order to resolve the dipolar physics. The duration of coherence times in experiments is typically limited by spatially varying and state-dependent light shifts from the optical trapping potential. Utilising rotationally magic wavelength traps eliminates differential ac Stark shifts between different rotational states, allowing for observations of interactions at these small energy scales.

Recently, experiments using  $^{23}\text{Na}^{87}\text{Rb}$  molecules in a near-magic optical lattice reported rotational coherence times of 56(2) ms [44]. Various other methods of extending rotational coherence times such as modifying the polarisation [45–48] or the intensity of the trapping light [49]. To date, the longest rotational coherence time reported without rephasing is 93(7) ms for single CaF molecules confined to optical tweezers with the polarisation set to a magic angle; this was extended to 470(40) ms using a spin-echo se-

quence [47]. In an effort to prolong coherence times between different rotational states of RbCs and access dipolar interactions, we utilise the rotational magic detuning region between transitions to the  $v' = 0$  and  $v' = 1$  states identified in chapter 4.

In this chapter, we report world-record coherence times between different rotational states of dipolar molecules. We begin by giving a brief summary of magic wavelengths in the context of trapping potentials as well as introducing the rotational states we utilise throughout this chapter. Next, we present our experimental setup and characterise the lifetimes of molecular samples in our trap, demonstrating our methods are compatible with long lifetimes. We then introduce a procedure of using Ramsey sequences to identify magic detunings for different pairs of rotational states. Using Ramsey sequences, we show that trapping with the light tuned to the magic detuning produces a trapping potential that supports long coherence times. These coherence times are chiefly limited by dipole-dipole interactions in the case of dipolar mixtures. Finally, we investigate tuning the strengths of interactions dipolar-mixtures by preparing different superpositions of rotational states in the trap.

## 5.2 Magic trapping overview

We concentrate our efforts on the rotationally magic detuning that exists between transitions to the  $b^3\Pi_0(v' = 0)$  and  $b^3\Pi_0(v' = 1)$  state, presented in Fig. 5.1(a). The magic detuning between the  $v' = 0$  and  $v' = 1$  transitions exists at the largest detuning relative to the nearest electronic transition as illustrated in Fig. 4.11. This yields the magic condition most favorable for engineering long coherence times as the differential polarisability between states is least sensitive to variations in laser detuning. Moreover, the larger detuning decreases the effects of photon scattering which limits lifetimes in the trap.

In Fig. 5.1(b-c), we illustrate the effect of laser detuning on the trapping potential experienced by the  $(N'' = 0, M''_N = 0)$  and  $(N'' = 1, M''_N = 0)$  states, which we label as  $|0\rangle$  and  $|1\rangle$  respectively. At magic, we access the condition where the polarisabilities associated with  $|0\rangle$  and  $|1\rangle$  ( $\alpha_{|0\rangle}$  and  $\alpha_{|1\rangle}$ ) are equal, producing a trap where the difference in trapping potential experienced by each state is independent of the beam intensity sampled.

In this chapter, we utilise states that experience similar Zeeman shifts,

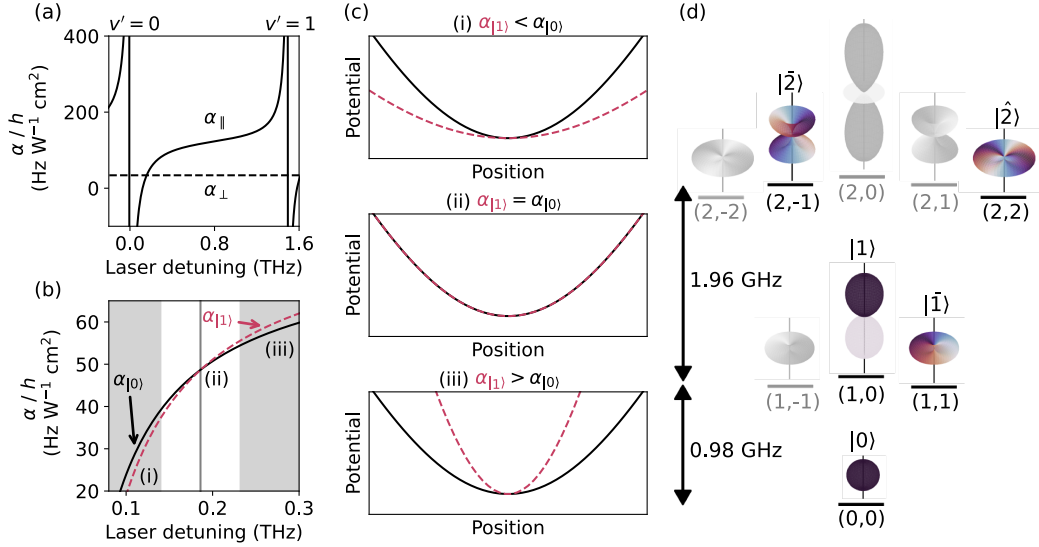


**Figure 5.1:** Magic trapping overview. (a) Reminder of parallel and perpendicular polarisability variation as we tune the laser between transitions to  $v' = 0$  and  $v' = 1$  vibrational levels of the  $b^3\Pi$  potential. (b) Polarisability for states  $|0\rangle$  and  $|1\rangle$  as a function of laser detuning from the transition to  $b^3\Pi(v' = 0)$ . At a detuning of  $\sim 0.186$  THz, the trap is rotationally magic and the polarisability for both states is the same. (c) Schematic of the relative trap potential for laser detunings such that (i)  $\alpha_{|1\rangle} < \alpha_{|0\rangle}$ , (ii)  $\alpha_{|1\rangle} = \alpha_{|0\rangle}$ , (iii)  $\alpha_{|1\rangle} > \alpha_{|0\rangle}$ . (d) Relevant rotational states in this work labelled by  $(N'', M_N'')$ . Wavefunctions for each state are shown with phase information for the states used in this work represented by the colour.

minimising decoherence associated with magnetic field noise. The largest contribution to the magnetic moment is generally provided by the nuclear spins, and so we choose states that have the same nuclear spin projections  $m_{\text{Rb}}'' = 3/2$ ,  $m_{\text{Cs}}'' = 7/2$ . Full composition of the states used in this chapter, calculated using [141] and given in the uncoupled basis  $(N'', M_N'', m_{\text{Rb}}'', m_{\text{Cs}}'')$  are

$$\begin{aligned}
|0\rangle &\equiv \mathbf{1.000} |0, 0, 3/2, 7/2\rangle \\
|1\rangle &\equiv \mathbf{0.924} |1, 0, 3/2, 7/2\rangle - 0.370 |1, 1, 1/2, 7/2\rangle \\
&\quad + 0.091 |1, 1, 3/2, 5/2\rangle \\
|\bar{1}\rangle &\equiv \mathbf{1.000} |1, 1, 3/2, 7/2\rangle \\
|\bar{2}\rangle &\equiv \mathbf{0.934} |2, -1, 3/2, 7/2\rangle - 0.220 |2, 1, -1/2, 7/2\rangle \\
&\quad - 0.207 |2, 0, 3/2, 5/2\rangle + 0.168 |2, 0, 1/2, 7/2\rangle \\
&\quad - 0.056 |2, 2, -3/2, 7/2\rangle + 0.055 |2, 1, 1/2, 5/2\rangle \\
&\quad + 0.039 |2, 2, -1/2, 5/2\rangle - 0.005 |2, 2, 1/2, 3/2\rangle \\
&\quad - 0.001 |2, 1, 3/2, 3/2\rangle - 0.001 |2, 2, 3/2, 1/2\rangle \\
|\hat{2}\rangle &\equiv \mathbf{1.000} |2, 2, 3/2, 7/2\rangle .
\end{aligned}$$

The coefficients are each given to 3 decimal places. State wavefunctions are presented as the coloured plots in Fig. 5.1(d).

### 5.3 Magic trapping setup

Magic trapping light is produced by a Vexlum Valo SF laser. It produces up to 4 W of light at the magic frequency for  $N'' = 0$  and  $N'' = 1$  states between transitions to  $v' = 0$  and  $v' = 1$ . We can tune the laser within  $\pm 20$  GHz of this frequency without any appreciable difference in output power or beam quality. We lock the Vexlum using the scanning transfer cavity lock (STCL, see chapter 4), with the Stokes laser as the reference. The STCL stabilising feedback signal is connected to the piezo offset input at the rear of the Vexlum. We estimate the stability of the laser frequency to be  $\pm 0.761(10)$  MHz over the course of each measurement conducted in this chapter.

The Vexlum output light is split into three paths, two paths lead to the experiment and form the beams of the trap. Light from the other path is coupled to the wavemeter and etalon for absolute frequency referencing and frequency locking. The Vexlum setup is presented in Fig. 5.2(a). The paths are created using a series of PBS cubes and half-wave plates. The two beams (B1 and B2) that are transferred to the experiment are passed through separate AOMs. B1 passes through an AOM driven by a fixed-frequency driver at 80 MHz whereas B2 passes through an AOM driven at 90 MHz. This prevents lattice effects from the beams crossing at the molecules with the same polarisation. The beams are then delivered to the experiment via optical fibres (standard Thorlabs APC patch cables). We limit the coupling of  $\sim 1$  W of light into each of B1 and B2 fibres to avoid fibre input port damage.

On the experimental side, the outputs of B1 and B2 are transmitted through separate PBS cubes, ensuring light from both beams is horizontally polarised at the molecules as presented in Fig. 5.2(b). The beams are directed towards the molecules using two launching mirrors. Leaked light through the mirrors are collected on photodiodes for power monitoring. The beams are not actively stabilised but are passively stable to  $<5\%$  variation over the course of each measurement. Light from B1 after traversing through the cell is then collected on a second photodiode for experimental troubleshooting purposes. The beams have a waist of  $50\ \mu\text{m}$  at the molecules and cross at an angle of  $20^\circ$ . For ground state molecules, the trap frequency experienced at the magic frequency is  $[\omega_x, \omega_y, \omega_z] = [29(1), 144(5), 147(5)]$  Hz for a peak laser intensity of  $14\ \text{kW}/\text{cm}^2$ .

With the exception of results in Fig. 5.3(b), molecules are transferred to the magic trap by ramping the power in the 1145 nm light for over 30 ms, and then the power in the 1550 nm trap off over a further 5 ms. We then briefly turn the magic trapping light off while we transfer to the  $|0\rangle$  state using STIRAP to avoid spatially varying ac Stark shifts. For the measurements in Fig. 5.3(b), we increased the power in the 1550 nm trap after the removal of atoms with Stern-Gerlach separation and transferred to the magic trap following ground-state transfer.

### 5.3.1 Lifetimes in the magic trap

We characterise the lifetimes of molecular samples in our magic trap by observing the population of molecules as a function of hold time, demonstrating our procedure is compatible with long trap lifetimes. The magic detuning exists only  $\sim 186$  GHz from the  $v' = 0$  transition, prompting concerns of loss of molecules due to photon scattering. We then compare results to a trap of 1064 nm light that is delivered down the same paths as the magic trap. The 1064 nm trap intensity is such that in both the magic and 1064 nm traps, the molecules experience the same trap frequencies.

We begin the measurement after a hold time in the trap of 0.4 s to lower the density of molecules and therefore reduce collisional losses [185, 194]. We measure the population of molecules in state  $|0\rangle$  as a function of time in each trap, producing the data presented in Fig. 5.3(b). Data is fitted with the exponential function  $N_{\text{mol}} = N_{\text{mol}}^{\text{init}} e^{-kt}$  where  $N_{\text{mol}}^{\text{init}}$  is the molecular population at time  $t = 0$  and  $k$  characterises the loss rate from the trap. We extract a loss rate of  $k_{1145} = 0.61(5)\ \text{s}^{-1}$  with 1145 nm light, and  $k_{1064} = 0.56(7)\ \text{s}^{-1}$

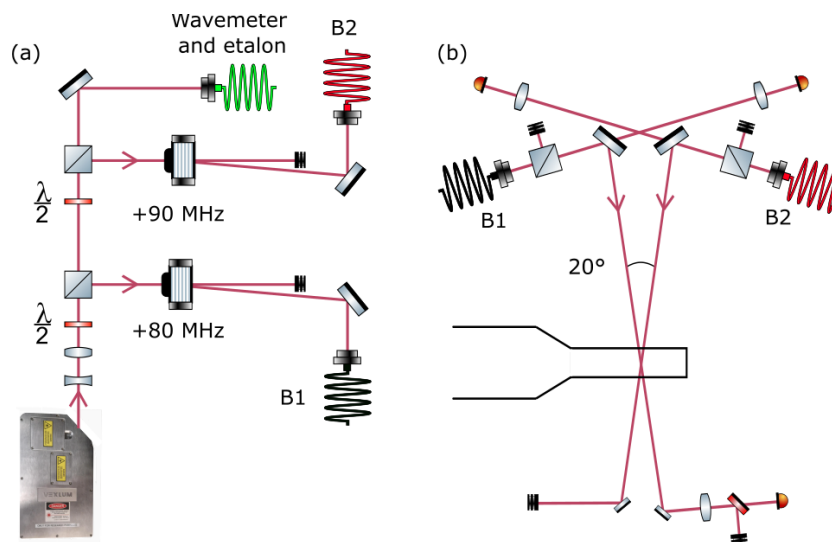


**Figure 5.2:** Magic trap setup. (a) Vexlum laser split into three beams. B1 and B2 are relatively detuned by 10 MHz after passing through two different AOMs and are transferred by optical fibres to the experiment. The third beam is delivered to the wavemeter and etalon through a third fibre. (b) Experimental-side dipole trap configuration. B1 and B2 are transmitted through separate PBS cubes and launched off mirrors towards the molecules. Photodiodes used for power monitoring purposes.

with 1064 nm light. This is consistent with the hypothesis that the rate of loss is not dependent on the wavelength.

To estimate the upper limit to the photon rate, we calculate the difference in these scattering rates  $k_{1145} - k_{1064} = 0.05(9) \text{ s}^{-1}$ , assuming no correlation in the uncertainty of the two measurements. We construct confidence intervals using the approach of Feldman and Cousins [195] assuming that  $k_{1145} \geq k_{1064}$ . At the 95% confidence level, this indicates that the difference in loss rate must be below  $0.23 \text{ s}^{-1}$ . This is broadly consistent with the expected single photon scattering rate which we calculate to be  $0.4(1) \text{ s}^{-1}$  from the linewidths found in chapter 4.

When molecules are prepared in superpositions of rotational states connected by dipole-allowed transitions, they exhibit an oscillating dipole moment in the laboratory frame. The resulting dipole-dipole interactions significantly affect the collisional loss rate [185]. We compare loss from the magic trap for molecules prepared in either  $|0\rangle$ ,  $|\bar{1}\rangle$  or in the superposition  $\frac{1}{\sqrt{2}} (|0\rangle + |\bar{1}\rangle)$  as illustrated in Fig. 5.3(c). For the dipolar superposition,

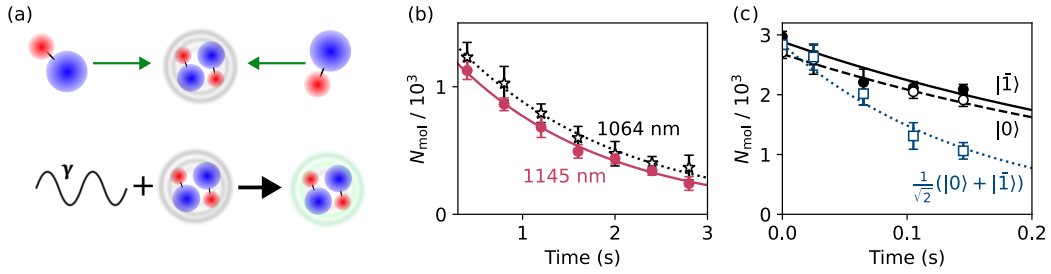


**Figure 5.3:** Lifetime of molecules in the trap. (a) Cartoon showing loss mechanism for molecules in the trap. Colliding molecules forming the collisional complex  $(\text{RbCs})_2$ . The complex is then excited by a photon from the trapping light,  $\gamma$ . The excited state then decays to undetectable atom/molecule combinations. (b) Comparison of molecule loss in the magic trap (filled squares) compared to an equivalent trap using 1064 nm light (empty stars). (c) Comparison of loss from the 1145 nm trap for molecules prepared in either  $|0\rangle$ ,  $|\bar{1}\rangle$  or in the superposition  $\frac{1}{\sqrt{2}}(|0\rangle + |\bar{1}\rangle)$ . Exponential fits are shown for all results.

we observed a loss rate that is 2.5 times greater than for molecules in either  $|0\rangle$  or  $|\bar{1}\rangle$ . Therefore, the interrogation time available for dipolar samples is much shorter than for non-interacting samples.

## 5.4 Identifying the rotationally magic detuning with Ramsey

To identify the magic detuning for different pairs of rotational states, we perform a Ramsey experiment visualised as the Bloch spheres in Fig. 5.4(a) with molecular samples trapped using different frequencies of light. In the example shown, a  $\pi/2$  pulse of resonant microwaves first prepares the molecules in an equal superposition of states  $\frac{1}{\sqrt{2}}(|0\rangle + |1\rangle)$ . This is then allowed to freely evolve for a time,  $T$ , during which the Bloch vector precesses around the equator at a rate proportional to the detuning of the microwaves from resonance. Finally, a second  $\pi/2$  pulse with variable phase  $\Phi$  is used to project back onto the state  $|0\rangle$  for detection. We implement a different sequence of microwave pulses depending on the superposition of rotational states and whether a spin-echo pulse is necessary as illustrated in Fig. 5.4(b).

For a given pair of states, we fix the Ramsey time and measure the contrast of Ramsey fringes as a function of the laser detuning. Fringe contrasts and associated uncertainties are calculated using the Bootstrap method [196, 197]. We observe maximum fringe contrast when the trap light

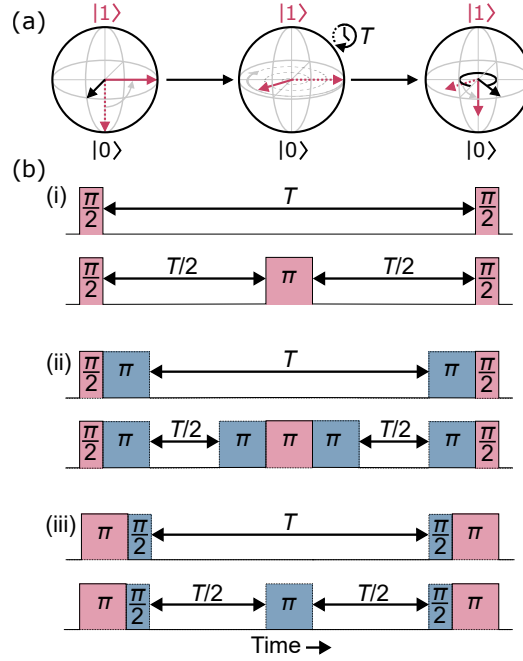


**Figure 5.4:** Bloch spheres and pulse sequences. (a) Bloch sphere representation of the Ramsey interferometry sequence. For each step, the dotted and solid red arrows represent the initial and final Bloch vector respectively. Solid black arrows indicate the axis about which the Bloch vector is rotated using coherent  $\pi/2$  pulses performed on microwave transitions between the neighbouring rotational states. In the example shown, a  $\pi/2$  pulse first prepares the molecules in an equal superposition of states  $\frac{1}{\sqrt{2}}(|0\rangle + |1\rangle)$ . This is then allowed to freely evolve for a time,  $T$ . Finally, a second  $\pi/2$  pulse with variable phase  $\Phi$  is used to project back onto the state  $|0\rangle$  for detection. Ramsey fringes are observed as a variation in molecule number  $N_{\text{mol}}$  in state  $|0\rangle$  as a function of  $\Phi$ . (b) Pulse sequences used in Ramsey interferometry. The solid line with red fill indicates microwave transitions driven between  $N'' = 0$  and 1 rotational states, and the dotted line with blue fill indicates transitions driven between  $N'' = 1$  and 2. Sequences are used for the combinations (i)  $\frac{1}{\sqrt{2}}(|0\rangle + |1\rangle)$ ,  $\frac{1}{\sqrt{2}}(|0\rangle + |\bar{1}\rangle)$ , (ii)  $\frac{1}{\sqrt{2}}(|0\rangle + |\hat{2}\rangle)$  and (iii)  $\frac{1}{\sqrt{2}}(|1\rangle + |\bar{2}\rangle)$ . In each case the top (bottom) sequence shows the sequence without (with) a spin-echo pulse. To measure a Ramsey fringe, the phase of the last  $\pi/2$  pulse is varied

is tuned to the magic detuning as shown in Fig. 5.5(a), indicating that the coherence time for that combination of states has been maximised.

We repeat for multiple combinations of states, presented in Fig. 5.5(b). Microwave pulses used for each combination of states are presented in Fig. 5.4(b) as the sequences without spin-echo pulses. The frequency on the

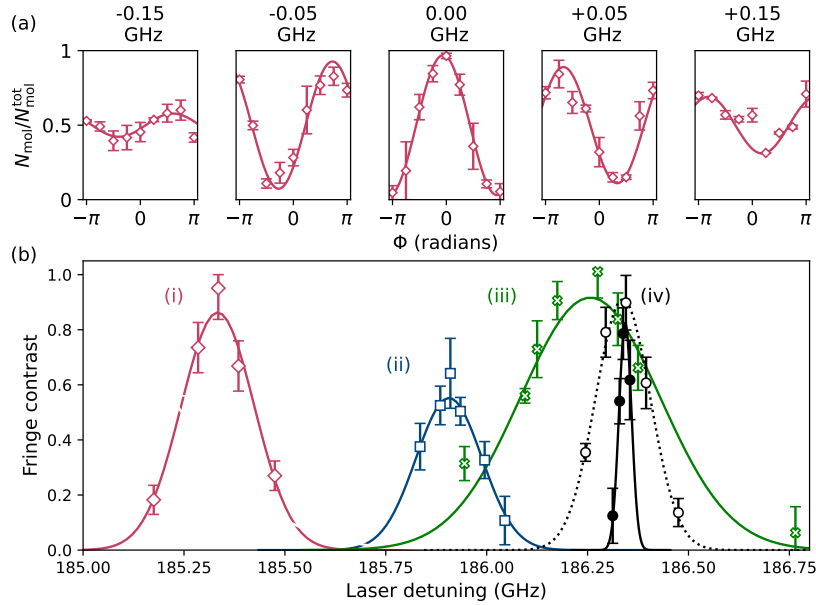


**Figure 5.5:** (a) Example Ramsey fringes for case (i); the molecule number detected in state  $|0\rangle$  is plotted as a fraction of the total number  $N_{\text{mol}}^{\text{tot}}$ . The detuning of trapping light with respect to magic is given above each subplot. (b) Fringe contrast as a function of trap laser detuning from the transition to  $b^3\Pi(v' = 0)$  for state combinations and Ramsey times (i)  $\frac{1}{\sqrt{2}}(|0\rangle + |1\rangle)$ ,  $T = 20$  ms; (ii)  $\frac{1}{\sqrt{2}}(|0\rangle + |\bar{1}\rangle)$ ,  $T = 30$  ms; (iii)  $\frac{1}{\sqrt{2}}(|1\rangle + |2\rangle)$ ,  $T = 30$  ms. Results for the combination (iv)  $\frac{1}{\sqrt{2}}(|0\rangle + |\hat{2}\rangle)$  are shown for Ramsey times of  $T = 40$  ms (empty circles) and  $T = 175$  ms (filled circles). The lines show Gaussian fits to each of the results to identify the magic detuning.

horizontal axis is the average frequency of the two trapping beams. There is a small  $\sim 1$  GHz variation in the magic detuning that depends upon the states chosen; this is due to coupling to different rotational levels of the excited vibrational states [172]. The width of the feature depends on the sensitivity of the light shifts to the laser frequency and is inversely proportional to the Ramsey time. We frequency stabilise the trapping light to the centre of the relevant feature in Fig. 5.5(b) for maximum coherence times.

## 5.5 Long coherence times

We first measure the coherence time for a non-interacting sample of molecules by examining the coherence between  $|0\rangle$  and  $|\hat{2}\rangle$ ; these are two states not

linked by an electric dipole-allowed transition. We use a pulse sequence composed of one-photon  $\pi/2$  and  $\pi$  pulses on the electric dipole-allowed transitions  $|0\rangle \leftrightarrow |\bar{1}\rangle$  and  $|\bar{1}\rangle \leftrightarrow |\hat{2}\rangle$  as illustrated in Fig. 5.4(b). We measure the contrast of the Ramsey fringes as a function of time, normalised to the number of molecules remaining in the sample, as shown by the empty circles in Fig. 5.6. We fit the results with a Gaussian model for decoherence, where the fringe contrast  $C(t) = \exp[-(T/T_2^*)^2]$ , and find a coherence time  $T_2^* = 0.78(4)$  s.

We remove most of the decoherence effects limiting the coherence time by introducing a single spin-echo pulse halfway through the Ramsey time; this is an effective  $\pi$  pulse between  $|0\rangle$  and  $|\hat{2}\rangle$  that reverses the direction of precession around the Bloch sphere, thereby cancelling out single particle dephasing from static inhomogeneities. We discuss sources of decoherence later in this chapter. The result is shown by the filled circles in Fig. 5.6. We now observe no loss of fringe contrast over 0.7 s. We do not measure for longer times as molecule loss diminishes the signal-to-noise ratio; for all measurements shown at least 500 molecules are detected at the maximum of the Ramsey fringe.

We fit our results using the Gaussian model, with confidence intervals defined using the Feldman and Cousins approach, to estimate a minimum coherence time consistent with our results to be  $T_2 > 1.4$  s at the 95% confidence level. This represents the suppression of all decoherence at the detectable precision of our experiment.

## 5.6 Observation of dipole-dipole interactions

For superpositions of states that lead to oscillating dipoles, dipolar interactions also cause dynamics of Ramsey contrast and therefore introduce an additional source of decoherence. The dipole-dipole interactions in the system are described by Eq. 2.22.

We examine the coherence between  $|0\rangle$  and  $|\bar{1}\rangle$ . An equal superposition of these states produces a dipole that rotates around the quantisation axis with magnitude given by the transition dipole moment  $d_0/\sqrt{3}$ . However, due to the factor of 2 in the denominator of the final term of Eq. 2.22, this contributes an effective dipole  $d = d_0/\sqrt{6} = 0.5D$  in the lab frame. At the peak densities in our experiments, this corresponds to an interaction strength of  $\sim h \times 2$  Hz. The fringe contrast measured as a function

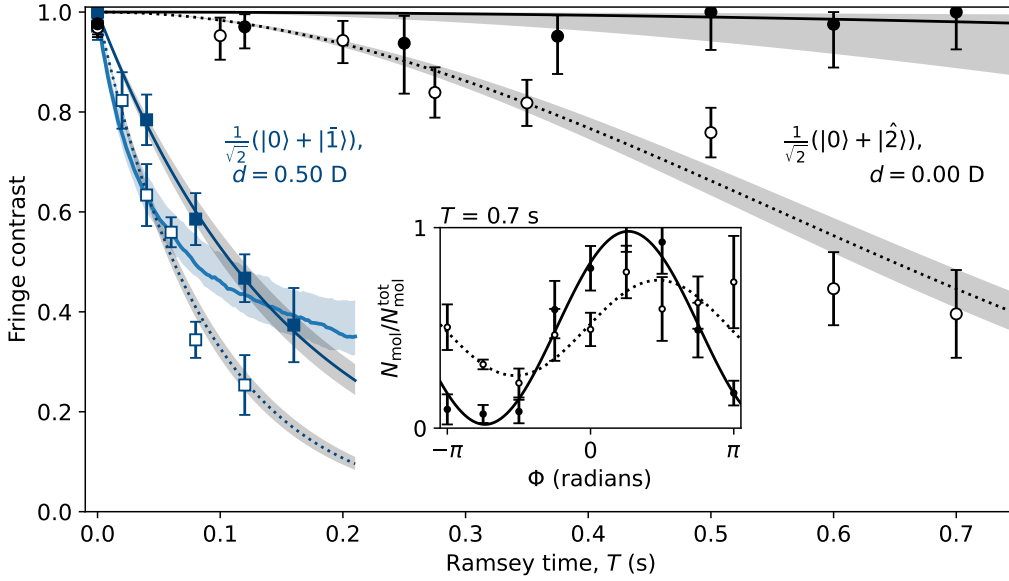


**Figure 5.6:** Second-scale coherence between different rotational states. (a) Fringe contrast as a function of the Ramsey time for non-interacting  $\frac{1}{\sqrt{2}}(|0\rangle + |\hat{1}\rangle)$  (black circles) and dipolar  $\frac{1}{\sqrt{2}}(|0\rangle + |\hat{1}\rangle)$  (blue squares) superpositions. Empty markers indicate measurements using a standard Ramsey sequence, and filled markers indicate measurements performed with the addition of a single spin-echo pulse. The non-interacting results are fitted using a Gaussian model for decoherence, and the dipolar results are fitted assuming an exponential decay in fringe contrast. The blue lines indicate the decay in fringe contrast from MACE simulations [121, 198]. Uncertainties in the fits and simulations are shown by the shaded regions. The fringes observed for  $\frac{1}{\sqrt{2}}(|0\rangle + |\hat{2}\rangle)$  with and without spin echo at  $T = 0.7$  s are shown in the inset.

of time is shown in Fig. 5.6 by the blue squares, with (filled) and without (empty) a spin-echo pulse. We see a dramatic reduction in the coherence time measured using either sequence when compared to the non-interacting case. Moreover, the results are no longer well described by the Gaussian model. Instead, we fit the results assuming an exponential decay of fringe contrast  $C(t) = \exp(-T/T_2^{\text{DDI}})$ .

We find a  $1/e$  coherence time of 89(5) ms without spin echo and  $T_2^{\text{DDI}}=157(14)$  ms with spin echo using the sequence presented in Fig. 5.4(b)(i). The residual ac Stark shifts that affect the results without spin echo vary depending on the combination of states; we expect that the uncertainty in the magic detuning is dominant for this dipolar combination as collisional

losses and dipolar decoherence limit the Ramsey time used during the optimisation. However, the difference in coherence time between dipolar and non-interacting samples that is observed with the spin-echo pulse can be attributed to dipole-dipole interactions alone.

Dipole-dipole interactions in our sample are modelled by K. R. A. Hazzard *et al.* using moving-average cluster expansion (MACE) simulations [121, 198] as presented as the blue lines in Fig. 5.6. For their calculations, molecules are in fixed positions in space, possibly attributing to the disagreement in decoherence rate with respect to the experiment, especially at earlier Ramsey times.

## 5.7 Spin echo efficacy

We characterise the efficacy of the spin echo pulse by performing a spin echo sequence with  $\frac{1}{\sqrt{2}}(|0\rangle + |\hat{2}\rangle)$  at a fixed hold time and vary the trapping laser detuning. We fix the hold time to 200 ms which corresponds to  $\sim 20\%$  longer than the longest Ramsey time we probe our dipolar mixture. Observing maximum fringe contrast at 200 ms using a spin echo sequence with  $\frac{1}{\sqrt{2}}(|0\rangle + |\hat{2}\rangle)$  corresponds to a trapping wavelength sufficiently close to magic that differential ac Stark shifts from trapping light are negligible.

We observe Ramsey fringe contrast at 200 ms as a function of laser detuning, producing the data presented in Fig. 5.7(a). The resulting data is then fitted with a Gaussian function. We extract a  $1\sigma$  width from the Gaussian fitting of 46(3) MHz. We therefore consider differential ac Stark shifts from trapping light to be a negligible source of decoherence for measurements up to 200 ms provided that we stabilise our trapping light to within  $\sim 15$  MHz of the magic detuning.

## 5.8 Phase slip in Ramsey fringes

We observe a variation in the phase of the Ramsey fringes of spin echo sequences with  $\frac{1}{\sqrt{2}}(|0\rangle + |\hat{2}\rangle)$  as a function of time. The relative phase with respect to the phase of the Ramsey fringe at Ramsey time  $T = 0$  is presented in Fig. 5.7(b). We fit the relative phase as a function of time with the quadratic function  $\Delta\Phi = aT^2$ . The fitted value of  $a$  is -3.76(5) rad/s<sup>2</sup>.

This relative phase slip does not lead to any appreciable loss of coherence,

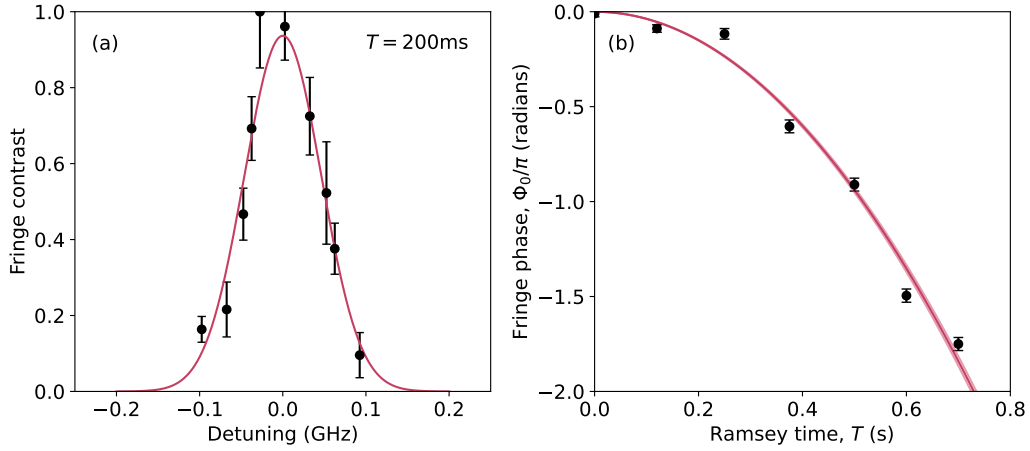


**Figure 5.7:** Spin echo efficacy and phase slip. (a) Fringe contrast as a function of laser detuning for spin echo sequence with  $\frac{1}{\sqrt{2}}(|0\rangle + |\hat{2}\rangle)$  at 200 ms. (b) Fringe phase for spin echo sequence with  $\frac{1}{\sqrt{2}}(|0\rangle + |\hat{2}\rangle)$  as a function of Ramsey time. Quadratic fit to guide the eye.

though it indicates a time-varying shift in the energies of the states, causing a different phase to accrue over the two halves of the spin-echo sequence. At the longest Ramsey time we investigate (0.7 seconds), we observe a phase shift of  $-1.75(3)$  rad, corresponding to a mean shift in the energies between the two halves of the spin-echo sequence of  $0.88(2)$  Hz.

## 5.9 Tuning dipole-dipole interactions

We tune the strength of the dipole-dipole interactions by creating superpositions using different combinations of different states. In Fig. 5.8(a) we show the coherence time measured with a single spin echo pulse as the effective dipole moment is varied from 0.31 D to 0.65 D. The laser frequency is set to maximise the coherence time for each state combination.

As expected, we see that the coherence time is inversely proportional to the magnitude of the interaction strength  $U_{ij} \propto d^2$ , which confirms that dipolar interactions are dominant as presented in Fig. 5.8(a). Dipole oscillations for each dipolar superposition are presented in Fig. 5.8(b).

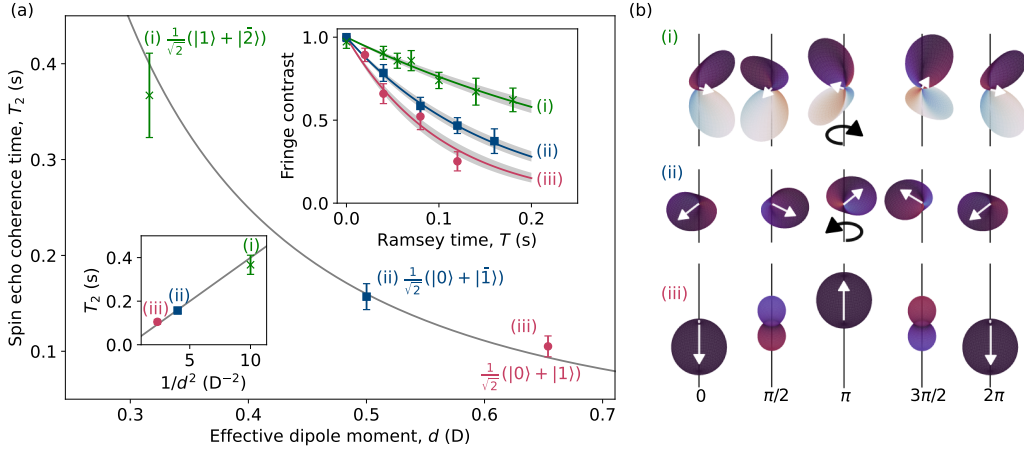


**Figure 5.8:** Tuning dipole-dipole interactions in the magic trap. (a) Coherence time in the presence of dipole-dipole interactions for superpositions of different states. We plot the  $1/e$  coherence time measured with spin echo as a function of the effective lab-frame dipole moment. The combinations used are (i)  $\frac{1}{\sqrt{2}}(|1\rangle + |\hat{2}\rangle)$ ; (ii)  $\frac{1}{\sqrt{2}}(|0\rangle + |\hat{1}\rangle)$ ; (iii)  $\frac{1}{\sqrt{2}}(|0\rangle + |1\rangle)$ . The fringe contrast as a function of time for each state combination is shown in the top right inset. The bottom left inset shows the coherence time plotted as a function of  $1/d^2$ . (b) Wavefunctions for dipolar superpositions as a function of time (phase,  $\phi$ ). The resultant dipoles are illustrated as white arrows with (i) and (ii) yielding dipoles rotating around the quantisation axis, and (iii) resulting in a dipole that oscillates up and down at a frequency proportional to the difference in energy between the states.

## 5.10 Sources of non-dipolar decoherence

We characterise sources of decoherence in our trap in the absence of dipolar interactions. These effects are most-evident in Fig. 5.6 as the non-spin echo data points for the superposition  $\frac{1}{\sqrt{2}}(|0\rangle + |\hat{2}\rangle)$ , owing to the lack of dipolar interactions in this mixture. Here, the coherence time,  $T_2^*$  is limited by the variation in the energy between the two-state,  $\Delta E$

$$T_2^* = \frac{h}{\Delta E}, \quad (5.1)$$

where  $h$  is the Planck constant. For our calculations, we assume  $\Delta E$  is the  $2\sigma$  variation in transition energy.

### 5.10.1 Instability in trap laser frequency

We directly measure the coefficient relating the light shift to the change in laser frequency for the  $|0\rangle$  and  $|2\rangle$  states to be  $6.0(2) \times 10^{-7}$ . This was accom-

plished by measuring the Ramsey oscillation rate when the sample is trapped using different frequencies. The short-term linewidth of our laser stabilised using the STCL is 0.761(10) MHz. The  $2\sigma$  variation in the laser frequency therefore corresponds to  $2 \times 6.0(2) \times 10^{-7} \times 0.761(10) \text{ MHz} = 0.91(3) \text{ Hz}$  which we assume equal to  $\Delta E/h$ , yielding a limit on  $T_2^*$  of 1.10(4) s.

### 5.10.2 Uncertainty in magic from Ramsey optimisation

We measure the magic detuning for a given state combination as shown in Fig. 5.5(b). For the states  $|0\rangle$  and  $|\hat{2}\rangle$ , our most precise measurement of the magic detuning is found using a Ramsey time of  $T = 175 \text{ ms}$ , which has  $1\sigma$  uncertainty of 3 MHz. A systematic detuning of 3 MHz leads to an average light shift experienced by the molecules of  $6 \times 10^{-7} \times 3 \text{ MHz} = 1.8 \text{ Hz}$ . Spatial variation in this light shift causes decoherence. We estimate this variation from the known geometry of the trap beam and assume a thermal cloud of molecules at equilibrium at a temperature of  $\sim 1 \mu\text{K}$ . From this, the  $2\sigma$  variation in the light shift experienced will be 13% of the average, i.e. there is spatial variation in the light shift of  $0.13 \times 1.8 = 0.234 \text{ Hz}$ . This puts a limit on  $T_2^*$  of 4.3 s.

### 5.10.3 10 MHz difference in trapping beams

There is a 10 MHz frequency difference between the two beams that form the magic trap to eliminate interference effects. When set symmetrically about the magic frequency, there will be a light shift of  $6 \times 10^{-7} \times \pm 5 \text{ MHz} = \pm 3 \text{ Hz}$ . The effects from each beam are broadly cancelled as the intensities are set to be the same. However, variation in the relative intensities of the beams will vary as molecules move around the trap. We estimate from the known geometry of the trap beams and assuming a thermal cloud of molecules at equilibrium that the  $2\sigma$  variation in the beam balance is only 2%. This leads to a variation in the light shift of 0.12 Hz that corresponds to a limit on  $T_2^*$  of 8.3 s.

### 5.10.4 Magnetic field instability and total coherence limit

Additionally, a small differential magnetic moment between the states of  $0.0124 \mu_N$  limits the coherence time to 10.6 s associated with magnetic field

noise ( $\sim 10$  mG).

Combining all contributions provides an expected limit on the coherence time of 0.74 s ( $1/(1/1.1 + 1/4.3 + 1/8.3 + 1/10.6)$ ), in excellent agreement with our observations.

## 5.11 Summary

In conclusion, we have demonstrated the efficacy of utilising magic wavelengths to extend coherence times between different rotational states in RbCs. We set up a sufficiently high-intensity crossed-optical dipole trap at the  $N'' = 0$  and  $N'' = 1$  rotational magic frequency between transitions to  $v' = 0$  and  $v' = 1$ . We then characterised the lifetime of molecules that were confined to the trap and observed a decrease in the lifetime when molecules were prepared in a dipolar superposition, consistent with results presented in [185].

We presented a method of identifying the magic detuning for different pairs of rotational states by optimising the fringe contrast observed when performing a Ramsey sequence. After identifying the relevant magic detunings, we prepared our molecules in  $\frac{1}{\sqrt{2}}(|0\rangle + |\hat{2}\rangle)$  and trapped them with light at the magic frequency for states  $|0\rangle$  and  $|\hat{2}\rangle$ . We observe a coherence time of  $T_2^* = 0.78(4)$  s which was extended to  $T_2 > 1.4$  s at the 95% confidence level using a single spin-echo pulse.

When preparing our molecular sample in a dipolar superposition of states, we observed a significant reduction in coherence time. We coarsely tuned the strength of dipole-dipole interactions in our sample by preparing different superpositions of states. We observed a linear relationship between the spin-echo coherence time and the reciprocal of the effective dipole moment squared for a given superposition, confirming that dipolar interactions were the dominant cause of limiting coherence times.

Finally, we characterised other sources of decoherence in our setup. Combining all contributions provides an expected limit on coherence time without any spin-echo pulses of 0.74 s which is in excellent agreement with the  $\frac{1}{\sqrt{2}}(|0\rangle + |\hat{2}\rangle)$  coherence time results. Our results demonstrate an important milestone in realising RbCs molecules for use in quantum science experiments. Unlocking dipolar interactions paves the way for producing effective quantum computation and quantum simulation architecture.

# Chapter 6

## Towards Molecules in Lattices

### 6.1 Introduction

For many quantum science applications using diatomic polar molecules, arrays of single ground state molecules are required [32, 34, 199–202]. Optical lattice potentials provide the confinement, but reliably loading the lattice with a high percentage of single-site occupancy has proved difficult [43, 44, 203].

In 2017, Reichsöllner and Schindewolf *et. al* [50] at the University of Innsbruck demonstrated a procedure for efficiently loading atom pairs into individual optical lattice sites using dual-species Mott-insulator states of Rb and Cs atoms. These atom pairs were then associated to form RbCs Feshbach molecules with single-site occupancy using a Feshbach resonance at 352.74 G. However, a pathway to the electronic ground state was not experimentally explored as they did not have a functioning STIRAP system. The STIRAP transitions at 181.5 G we utilise in other chapters are not available at this magnetic field as we associate using a different resonance.

In this chapter, we establish a method for transferring RbCs molecules into the ground state that is compatible with the Innsbruck method for producing molecules in lattices. First, we outline the procedure demonstrated in Innsbruck and present the corresponding route to ground state RbCs. We then associate molecules using the relevant Feshbach resonances and perform spectroscopy of the pump transition as a function of magnetic field until we occupy an appropriate state for STIRAP. We present a method of accessing the appropriate state using RF-assisted jumping over an avoided crossing before directly measuring the STIRAP transition frequencies and coupling

strengths via spectroscopy and Rabi oscillations.

## 6.2 Innsbruck Method

In [50], the process begins with two spatially-separated Bose–Einstein condensates (BECs) of Rb and Cs in separate optical potentials. Making molecules from two BECs requires that the BECs are miscible. In a quantum degenerate mixture of atomic gases of Rb and Cs, the miscibility of the BECs is governed by the parameter [204, 205]

$$\Delta \sim \frac{a_{\text{RbCs}}}{\sqrt{a_{\text{RbRb}}a_{\text{CsCs}}}}, \quad (6.1)$$

where  $a_{\text{RbCs}}$ ,  $a_{\text{RbRb}}$  and  $a_{\text{CsCs}}$  are the intraspecies and interspecies scattering lengths for Rb and Cs respectively. If  $\Delta < 1$  ( $\Delta > 1$ ), the BECs are miscible (immiscible). However, if  $\Delta < -1$ , the mixture is miscible but unstable against collapse. Fortunately, we can use an interspecies Feshbach resonance to tune  $a_{\text{RbCs}}$ . A wider resonance is favourable as it gives more control over  $a_{\text{RbCs}}$ .

Both species are in their spin-stretched hyperfine ground state at a magnetic field of  $B \sim 21$  G. Here, the scattering lengths are  $a_{\text{RbCs}} \sim 650 a_0$ ,  $a_{\text{RbRb}} \sim 100 a_0$  and  $a_{\text{CsCs}} \sim 220 a_0$  as shown in Fig. 6.1(a). This renders the species immiscible. An optical lattice potential of 1064 nm light is then ramped on over both clouds to an intensity whereby the Cs cloud crosses the superfluid (SF) to Mott-insulator (MI) transition and the Rb remains a superfluid <sup>1</sup>. Now that the Cs is in an MI state, three-body Cs-Cs-Cs losses are eliminated due to suppression of tunnelling between sites, allowing the magnetic field to be varied without worrying about  $a_{\text{CsCs}}$  values. Next, the Rb is pushed towards the Cs so that it spatially overlaps. As this happens, the magnetic field is increased to a zero-point crossing of the interspecies scattering length at 354.95 G, near a wide (width = 2.70(47) G [71]) interspecies Feshbach resonance at 352.74 G. Access to this wide Feshbach resonance allows for reliable tuning of the interspecies scattering length around the zero-point crossing. The gradient of  $a_{\text{RbCs}}$  at the zero-point crossing near the 352.74 G resonance is  $\sim 0.3 a_0/\text{mG}$  whereas for the resonance at 197 G it is  $\sim 9 a_0/\text{mG}$ .

---

<sup>1</sup>Rb requires a greater intensity of trapping light to enter the MI regime due to the interplay between on-site interaction strength and the inter-site hopping parameter [206].

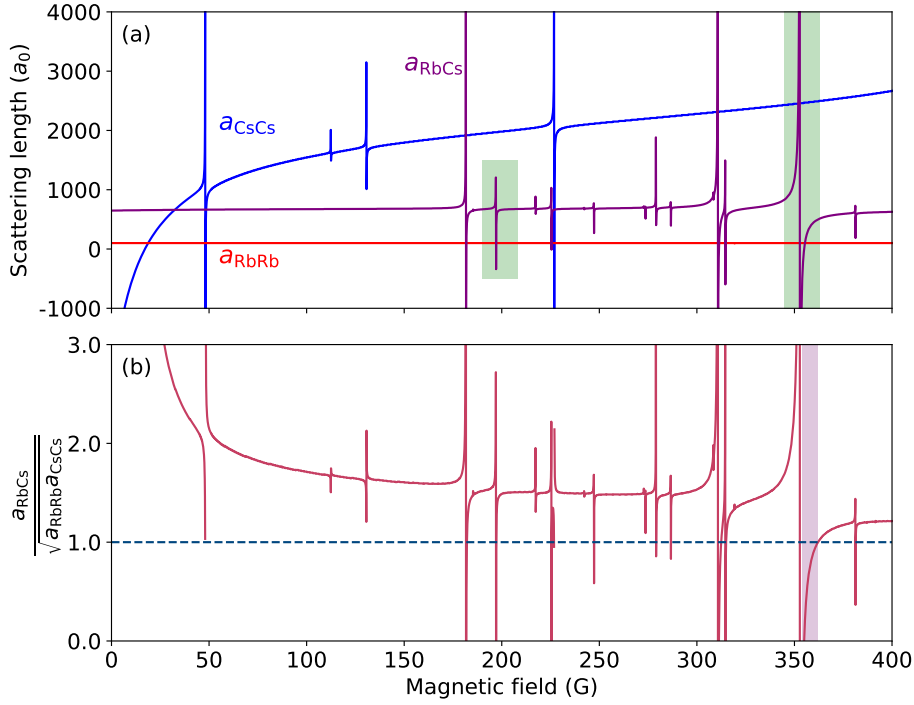


**Figure 6.1:** Scattering lengths and miscibility using calculations from Jeremy Hutson’s group [180]. (a) Inter and intra-species scattering lengths of  $^{87}\text{Rb}$  and  $^{133}\text{Cs}$  in their respective hyperfine ground states. The green boxes at 191.7 G and 352.74 G mark the Feshbach resonance we usually use to associate Rb and Cs atoms and the resonance used in the Innsbruck method respectively. (b) Eq. 6.1 as a function of magnetic field. Below the horizontal dashed line, the species are miscible. Purple shaded region shows the miscible and stable region relevant to the Innsbruck method.

In the region of  $-501 a_0 < a_{\text{RbCs}} < 499 a_0$  ( $354.0 \text{ G} < B < 362.1 \text{ G}$ ), the quantum degenerate mixtures are miscible and stable, illustrated in Fig. 6.1(b) as the purple region. This allows the Rb SF and Cs MI to overlap while three-body losses are suppressed. The depth of the optical potential is then increased by increasing the power of the lattice beams, causing Rb to also cross the SF to MI state transition. This produces a sample with a pair of atoms confined to each lattice site. Finally, the interspecies Feshbach resonance at 352.74 G is ramped over to associate the pairs of atoms into molecules, creating one molecule per lattice site with near 100% efficiency. Innsbruck demonstrated that greater than 30% of atoms in the initial BEC are converted into molecules using this method. Efficiency is limited by Cs MOT insulator loading, Cs intraspecies losses and 3-body interspecies loss

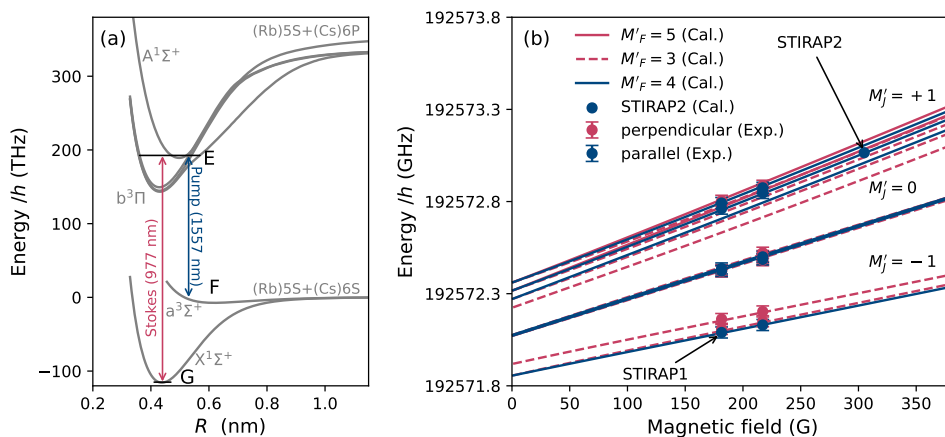


**Figure 6.2:** (a) STIRAP scheme showing relevant electronic state potentials. (b) Zeeman structure of the excited state. Theory fitted to experimental spectroscopy of pump transitions at 181.5 G and 217 G obtained by the University of Innsbruck. STIRAP1 and STIRAP2 are the STIRAP pump transitions for 181.5 G and 305 G respectively. Figure based on theory produced by Dr. Arpita Das at Innsbruck [123].

mechanisms.

### 6.3 Theoretical calculations

Theoretical calculations combined with experimental investigation provided an appropriate pump transition for STIRAP [123] at  $\sim 305$  G, presented as “STIRAP2” in Fig. 6.2(b). At this field, a Feshbach state with a dominant s-wave character exists which is beneficial for excited state coupling. We utilise the same rovibrational excited state for STIRAP at 305 G as for STIRAP at 181.5 G,  $b^3\Pi_1(v' = 29, N' = 1)$ . This state is chosen for its optimum singlet-triplet mixing with  $A^1\Sigma^+$  that is required for transferring to  $X^1\Sigma^+$  [153].

However, the excited state at the different magnetic fields comprises different nuclear spin projections. At 181.5 G we use an excited state with nuclear spins  $m'_{i_{\text{Rb}}} = 3/2$ ,  $m'_{i_{\text{Cs}}} = 7/2$ , whereas at 305 G we propose using a state with  $m'_{i_{\text{Rb}}} = 1/2$ ,  $m'_{i_{\text{Cs}}} = 5/2$ . The excited state at 305 G does not have desirable nuclear spin projections for coupling to the absolute ground state of RbCs. Instead, we will transfer to a  $(0, +4)$  state of  $X^1\Sigma^+$ .

## 6.4 Shorthand state notation

In this chapter, we find it useful to adopt shorthand notation for labelling bound states using  $L$  and the absolute value of the  $n$  quantum numbers. For instance, we label  $(-6(2,4)s(1,3))$  state as “s6”. In cases of states with mixed character, we give both angular momenta but with the dominant character wave is given first. A state with a mix of s and d wave characters but a dominant d wave character would be given the label “ds6”.

When we wish to denote a state in magnetic field regions above and below an avoided crossing, we use  $'$  to distinguish between the two. ds6' is at a lower magnetic field compared to ds6. The state predicted to be appropriate for STIRAP is the sd6 state at 305 G.

## 6.5 Associating at $\sim 352.74$ G

We search for the Feshbach resonance at 352.74 G by varying the magnetic field and observing the effects of three-body loss rates of our dual-species atomic sample in the xODT.

The interspecies scattering length near an interspecies Feshbach resonance is described by

$$a(B) = a_{\text{bg}} \left( 1 - \frac{\Delta}{B - B_0} \right), \quad (6.2)$$

where  $a_{\text{bg}}$  is the background interspecies scattering length,  $\Delta$  is the width of the resonance feature and  $B_0$  is the magnetic field at the centre of the resonance [72]. It's clear from the form of Eq. 6.2 that as we approach a resonance, the scattering length approaches  $\pm\infty$ . This is shown by the poles in Fig. 6.3(b). The three-body loss rate scales as  $a^4$  [207], leading to a dramatic increase in three-body loss rate from the trap as we approach an interspecies resonance.

After the atom evaporation step, we jump the magnetic field from 21 G to a magnetic field near the interspecies Feshbach resonance positions [146] and hold for 5 seconds in the xODT. We then repeat for various magnetic fields during the 5-second hold time and measure the Cs population. Cs is considered the “probe” species as the relative Cs and Rb populations make Cs more sensitive to 3-body losses [72]. Results of this measurement are

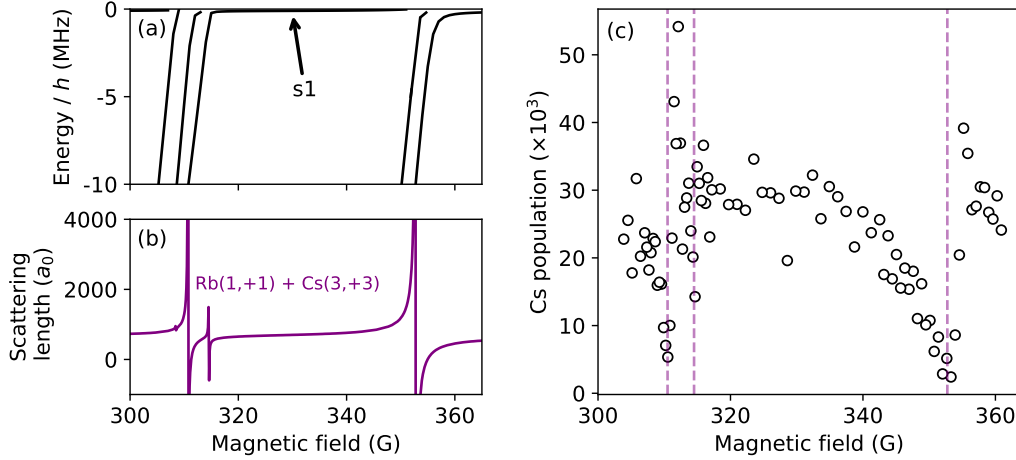


**Figure 6.3:** Feshbach resonance search. (a) Theoretical calculations of the binding energy of bound states as a function of magnetic field. (b) RbCs interspecies scattering length as a function of magnetic field. (c) Cs population as a function of holding magnetic field. Purple vertical dashed lines correspond to the positions of features in (b). Data for plots (a) and (b) are provided by Jeremy Hutson's group.

presented in Fig. 6.3(c). Other resonances around 310 G are also observed.

By sweeping down across the resonance at 352.74 G at a rate of  $\sim 2.5$  G/ms, we associate atoms into molecules occupying the weakly-bound s1 state that runs approximately parallel to the free-atomic energy, presented in Fig. 6.3(a).  $\sim 8000$  molecules are produced in this process based on previous experimental calibrations.

We ramp down the magnetic field after association so that we find an appropriate region for Stern-Gerlach separation. The avoided crossing between the g2 and the ds6 state, shown in Fig. 6.4(b), allows us to tune the magnetic moment of the molecule between  $+1.1 \mu_B$  and  $-1.4 \mu_B$ . We decrease the xODT intensity and tune the magnetic moment to around  $-0.9 \mu_B$  and apply a 32 G/cm magnetic field gradient, exactly levitating the molecules and removing the atoms from the trap in 15 ms.

We then increase the xODT intensity, transferring the molecules into a purely optical potential and typically lose about half the molecules through heating, collisional and photon-scattering processes. To detect molecules, we ramp the magnetic field back over the Feshbach resonance at 352.74 G to

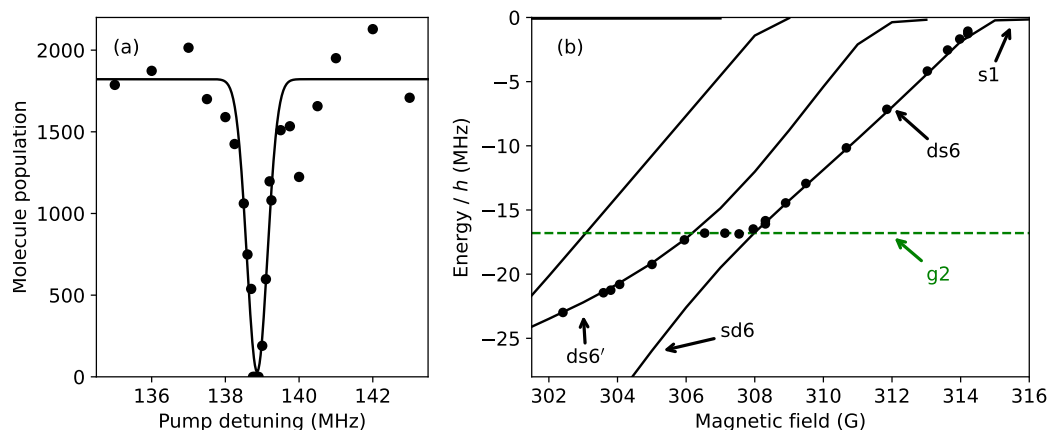


**Figure 6.4:** Mapping bound states of RbCs after association at 352.74 G. (a) Example pump spectroscopy using  $500 \mu\text{s}$  square pulse. (b) Experimental data overlaying theoretical mapping of bound molecular states only included  $L \leq 2$ . g-state with  $L = 4$  binding energy presented as green dotted line at  $\sim 16.8$  MHz.

dissociate and image the resulting atoms.

## 6.6 Searching for strong STIRAP transitions

We perform spectroscopy of the pump transition as a function of magnetic field, mapping out a path to sd6 for STIRAP. Following Stern-Gerlach separation, the magnetic field is ramped to a given set point in 2 ms. A subsequent 1 ms hold time is then employed to allow the magnetic field to stabilise. The molecules are then released from the xODT and a square pulse of vertically polarised pump light is applied for  $500 \mu\text{s}$ . We repeat for different values of pump detuning, observing a decrease in molecule population as we become resonant with the transition. The resulting loss feature is fitted with a Gaussian function and the centre of the loss feature is extracted as presented in Fig. 6.4(a). Typically, we determine the centre of the fit to  $< 160$  kHz. We then repeat for different magnetic fields as illustrated in Fig. 6.4(b). At  $\sim 308$  G, the molecules follow the avoided crossing between the g2 and ds6 states as the magnetic field is ramped down.

## 6.7 RF-assisted avoided crossing jumping

To access the sd6 state, we must devise a method of jumping the avoided crossing between g2 and ds6. This could be achieved with microwave  $\pi$  pulses

or fast magnetic field ramps. In our experiment however, we chose to adopt the hybrid-transfer procedure developed by Lang *et. al* [208], as it had been previously demonstrated and should be relatively robust to noise in the microwave power/frequency and the magnetic field.

The transfer scheme relies on the preparation of RF-dressed states. We begin with two molecular energy states,  $|u\rangle$  and  $|l\rangle$ . In the absence of interactions between  $|u\rangle$  and  $|l\rangle$ , they would cross at a magnetic field  $B_0$ . The system is described by the Hamiltonian

$$\hat{H}_{\text{Free}} = \hbar \begin{pmatrix} 0 & V_{|u\rangle|l\rangle}/2 \\ V_{|u\rangle|l\rangle}/2 & \Delta\mu_{|u\rangle|l\rangle} \Delta B \end{pmatrix}, \quad (6.3)$$

where  $\Delta B = |B_0 - B|$  with  $B$  being the applied magnetic field and  $\Delta\mu_{|u\rangle|l\rangle}$  is the difference in magnetic moment of  $|u\rangle$  and  $|l\rangle$ . The analytic solutions for the eigenenergies of eigenstates  $|u\rangle$  and  $|l\rangle$  are

$$E_{|u\rangle} = \frac{\hbar}{2} \left( (\mu_{|u\rangle} + \mu_{|l\rangle}) \Delta B + \sqrt{\Delta\mu_{|u\rangle|l\rangle}^2 \Delta B^2 + V_{|u\rangle|l\rangle}^2} \right) \quad (6.4)$$

$$E_{|l\rangle} = \frac{\hbar}{2} \left( (\mu_{|u\rangle} + \mu_{|l\rangle}) \Delta B - \sqrt{\Delta\mu_{|u\rangle|l\rangle}^2 \Delta B^2 + V_{|u\rangle|l\rangle}^2} \right), \quad (6.5)$$

respectfully. These eigenenergies are shown by the grey lines in Fig. 6.5(a).

Consider the addition of a blue-detuned RF-photon that couples the two states  $|u\rangle$  and  $|l\rangle$ . When extending this model to include an RF field, it's beneficial to adopt a dressed-state formalism whereby we can consider the energies of the states associated with  $\hat{H}_{\text{Free}}$  being perturbed by an integer multiple of the energy of a photon [209]. Using the rotating wave approximation by assuming small photon detuning, we arrive at a new dressed-state Hamiltonian

$$\hat{H}_{\text{Dress}} = \begin{pmatrix} E_{|u\rangle} & \hbar\Omega_{\text{RF}}/2 \\ \hbar\Omega_{\text{RF}}/2 & E_{|l\rangle} + \gamma_{\text{RF}} \end{pmatrix}. \quad (6.6)$$

$\Omega_{\text{RF}}$  is the Rabi frequency of the coupling between states  $|u\rangle$  and  $|l\rangle$  caused by our RF-photon and  $\gamma_{\text{RF}}$  is the energy of the RF photon. The Hamiltonian is not time-dependent as we are sufficiently detuned to prevent Rabi oscillations between  $|u\rangle$  and  $|l\rangle$ .

Here, we have perturbed the eigenstate of  $|l\rangle$  by the energy of a photon while  $|u\rangle$  remains unperturbed. The presence of RF coupling between

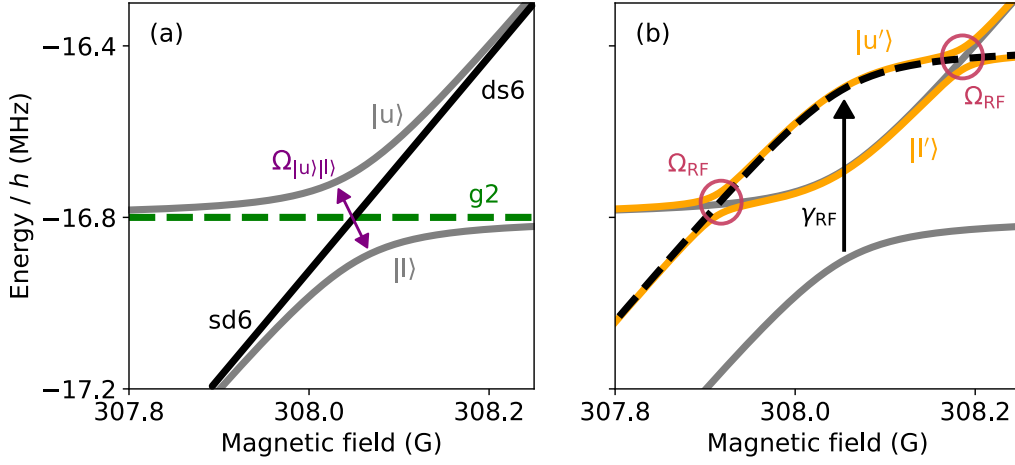


**Figure 6.5:** Avoided crossing and transfer scheme. (a) Diagram of avoided crossing between ds6/sd6 (black solid line) and the g2 state (green dashed line). Resulting avoided crossing coupled eigenvalues of  $|u\rangle$  and  $|l\rangle$  states presented as grey solid lines.  $\Omega_{|u\rangle|l\rangle}$ , indicated by the purple arrow is the Rabi frequency associated with the coupling between states  $|u\rangle$  and  $|l\rangle$ . (b) RF-assisted dressed-state scheme used to facilitate jumping. Orange solid lines denote the RF-dressed states.  $\gamma_{\text{RF}}$  is the energy of the RF photon.  $\Omega_{\text{RF}}$  is the Rabi frequency associated with the coupling between  $|u'\rangle$  and  $|l'\rangle$  at the circled avoided crossings.

states shown by the off-diagonal elements in the  $\hat{H}_{\text{Dress}}$  Hamiltonian creates new avoided crossings between the  $E_{|u\rangle}$  and  $E_{|l\rangle} + \gamma_{\text{RF}}$  states, presented in Fig. 6.5(b) as the orange lines. These new dressed states with RF-coupling are denoted as  $|u'\rangle$  and  $|l'\rangle$ .

In the experiment, we implement a transfer scheme using an RF field with a frequency of 400 kHz and a Rabi frequency of  $\sim 38$  kHz<sup>2</sup>, provided by a copper coil placed directly below the cell and driven with a sinusoidal pulse from an arbitrary function generator. The transfer scheme comprises three distinct steps as illustrated in Fig. 6.6(a):

- (i) With the RF-field on, we ramp the magnetic field from high to low so that the initial state follows the dressed state projection  $|u'\rangle$  to the centre of the avoided crossing in  $30 \mu\text{s}$  with the xODT off.
- (ii) We switch off the RF field, projecting the dressed-state Hamiltonian eigenstate  $|u'\rangle$  onto the bare Hamiltonian state  $|l\rangle$  and recapture the molecules in the xODT.

<sup>2</sup>This was determined by performing Rabi oscillations on the  $|u\rangle$  and  $|l\rangle$  states.

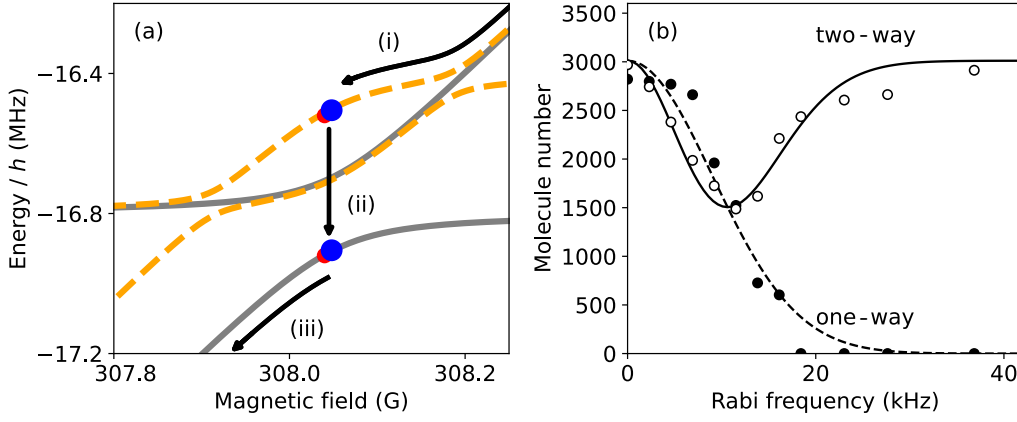


**Figure 6.6:** RF transfer scheme and one and two-way transfer population. (a) RF transfer scheme showing dressed-state (dashed orange lines) and bare (solid grey lines) energies of molecular states near ds6/g2 avoided crossing region. (b) Detected molecule population as a function of Rabi frequency of avoided crossing coupling for one-way and two-way transfer.

(iii) We continue the magnetic field ramp away from the avoided crossing.

We can assess the efficiency of our hybrid transfer method by observing the detected population after we jump the avoided crossing once or twice in succession. The probability of a molecule does not traverse the avoided crossing is given by the Landau-Zener probability model [210]

$$P_{\text{Once}} = \exp\left(-\frac{2\pi\Omega_{\text{RF}}^2}{\dot{B}\Delta\dot{\mu}_{|u\rangle|l\rangle}}\right), \quad (6.7)$$

where  $\dot{B}$  is the rate of change of the magnetic field and  $\Delta\dot{\mu}_{|u\rangle|l\rangle}$  is the rate of change of the difference in magnetic moment of  $|u\rangle$  and  $|l\rangle$ . It therefore follows that the probability of a molecule being observed after two successive avoided crossing ramps is

$$P_{\text{Twice}} = \left(1 - \exp\left(-\frac{2\pi\Omega_{\text{RF}}^2}{\dot{B}\Delta\dot{\mu}_{|u\rangle|l\rangle}}\right)\right)^2 + \exp\left(-\frac{4\pi\Omega_{\text{RF}}^2}{\dot{B}\Delta\dot{\mu}_{|u\rangle|l\rangle}}\right). \quad (6.8)$$

We repeat the experiment with varying powers of RF Rabi frequency and fit the data to the Landau-Zener probability model as shown in Fig. 6.5(b). We extract a value of  $\Delta\dot{\mu}_{|u\rangle|l\rangle} = 6.8(4) \times 10^4$  J/G/s by considering a constant magnetic field change of  $1.5 \times 10^4$  G/s during traversal.

## 6.8 Continued pump spectroscopy and pump Rabi oscillations

We perform pump spectroscopy after RF-assisted transfer to confirm the occupation of the sd6 state. We adapt the sequence described in Sec. 6.6 with the addition of two jumps over the avoided crossing between g2 and ds6 states, one before and one after the pump pulse. These results are presented in Fig. 6.7(a) as the unfilled data points.

We decrease the magnetic field by  $\sim 3$  G and perform STIRAP at 305 G where the absolute pump transition frequency is 192573.4(1) GHz. Uncertainty is limited by the precision of the wavemeter. The Zeeman shift of the transition is 3.090(14) MHz/G.

We directly measure the off-diagonal elements of the STIRAP Hamiltonian by observing a Rabi oscillation on the pump transition with our pump laser locked to 192573.4(1) GHz. After transferring the molecules to sd6 at 305 G, we release the molecules from the xODT. The molecules are then illuminated by the pump light for a fixed time before being recaptured in the dipole trap and reversing the state transfer and association sequence to measure the molecule population. We repeat this process for varying pump light pulse times. Results of this measurement are presented in Fig. 6.7(b). Error bars are the standard error of three repeated sequences.

Results from the Rabi oscillation are fitted with a damped sinusoidal function in order to extract a frequency. The extracted Rabi frequency is 632(16) kHz. This corresponds to an intensity normalised Rabi frequency of 0.8(1) kHz  $\sqrt{I_p}/(\text{mWcm}^{-2})$ . Dephasing of the oscillation is caused by inhomogeneous intensity sampling of our molecules across the cloud [154] and loss in molecular population as a function of pulse time is attributed to the existence of decay channels from the excited state to other states that we don't detect. This coupling strength is the same within uncertainty as the corresponding pump transition used for STIRAP at 181.5 G.

## 6.9 Stokes Spectroscopy at 305 G

We implement the same STIRAP pulse sequence described in chapter 3.3, transferring the population to a rovibrational ground state of the  $X^1\Sigma^+$  potential. The sequence is then reversed after  $5\mu\text{s}$  of pump light exposure and the molecule population is measured. If the Stokes light becomes resonant

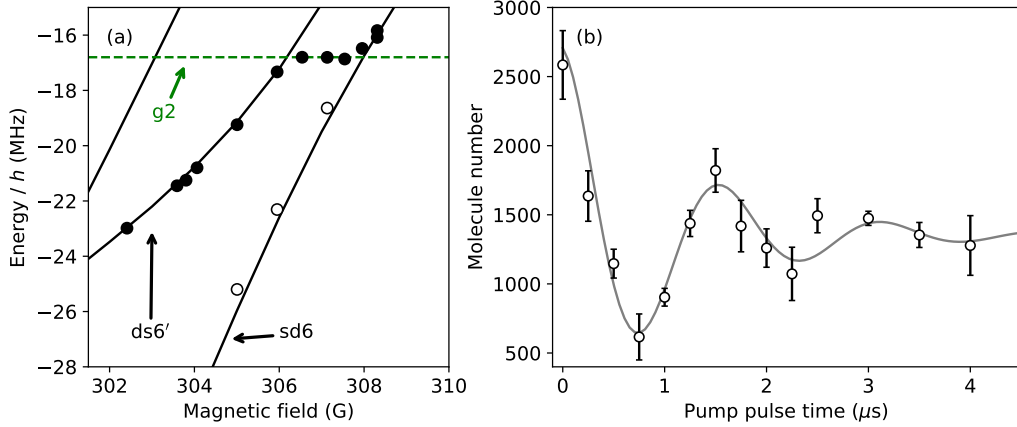


**Figure 6.7:** Continued pump spectroscopy and Rabi oscillation of pump transition. (a) Pump spectroscopy of sd6 state accessed by jumping avoided crossing using RF-photon assistance. (b) Pump Rabi oscillation at 305 G showing Feshbach molecule population as a function of pulse time. Inset shows the pump pulse sequence used.

with a transition, the molecules will complete a return transfer back to the Feshbach state and we will observe a peak in population. If the Stokes light is off-resonant with a transition, the pump leg of the STIRAP sequence will transfer molecules from the Feshbach state to the excited state but they will not return. The pump duration is sufficient that all Feshbach molecules are removed, leading to no observed molecule population when the Stokes is off-resonant with a transition.

Angular momentum selection rules limit the accessible  $X^1\Sigma^+$  states we can access. Our excited state in the STIRAP scheme at 305 G has  $M_F' = +4$ , therefore we can only transfer to  $X^1\Sigma^+$  states with total angular momenta projections  $M_F'' = +3, +4$  or  $+5$ .  $M_F'' = +3$ , and  $+5$  are accessed by light polarised orthogonal to the quantisation axis whereas  $M_F'' = +4$  is accessed by light polarised parallel to the quantisation axis. We can modify the polarisation of light by simply inserting a half-wave plate in the Stokes path before the light is transported to the experimental table via a polarisation-maintaining fibre.

We measure the population of molecules as a function of Stokes laser frequency for light polarised both parallel and orthogonal to the quantisation axis as presented in Fig. 6.8. Experimental data in Fig. 6.8(a) (Fig. 6.8(b)) are fit with a Gaussian function (the sum of multiple Gaussian functions).

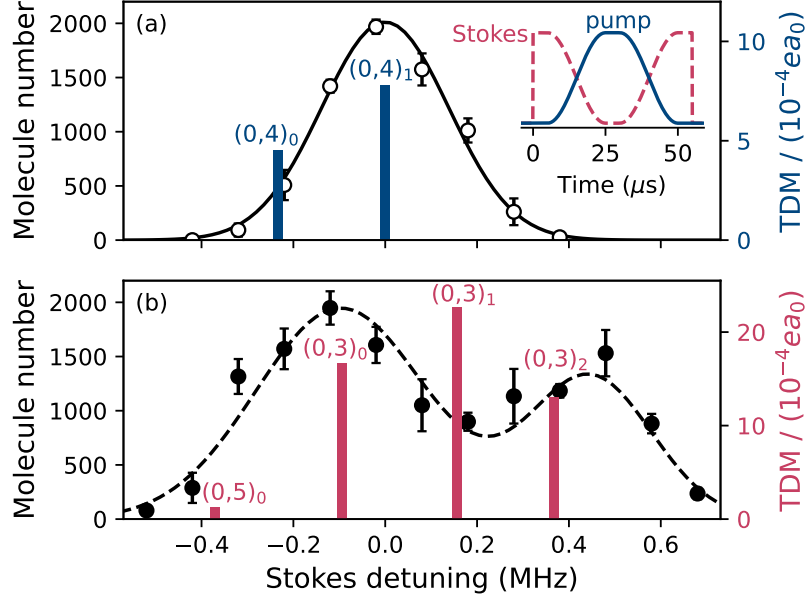


**Figure 6.8:** Stokes spectroscopy at 305 G. Population of ground state molecules as a function of Stokes detuning with respect to the transition to the  $(0,4)_1$  state with Stokes light polarised (a) parallel and (b) orthogonal to the magnetic field. The detuning is given with respect to the  $b^3\Pi_1(v' = 29, N' = 1) \rightarrow X^1\Sigma^+(v'' = 0, N'' = 0, M_F = +4, k = 1)$  transition. Theoretical calculations for TDMs of each transition are presented as vertical lines at their respective frequencies, calculated by Arpita Das *et. al* [123]. Inset in (a) presents a diagram of the pulse sequence used.

Theoretically predicted transition dipole moments are also presented for each of the transitions in the frequency range as vertical bars overlaying the experimental data.

The absolute value of the Stokes frequency for transition to the rotational ground state of the  $X^1\Sigma^+$  potential is 306831.2(1) GHz. By observing the number of molecules we detect after a round-trip STIRAP sequence with the Stokes light fixed to the centre of the feature in Fig. 6.8(a) and comparing to the initial population, we calculate the maximum one-way transfer efficiencies of 85(4)% and 92(7)% for parallel and perpendicular polarisation respectively.

## 6.10 Identifying ground state occupancy with MW spectroscopy

We confirm the quantum numbers of the  $X^1\Sigma^+$  states we access using microwave spectroscopy of rotational transitions, extracting transition frequencies and comparing them to the transition frequencies predicted by theory [141].

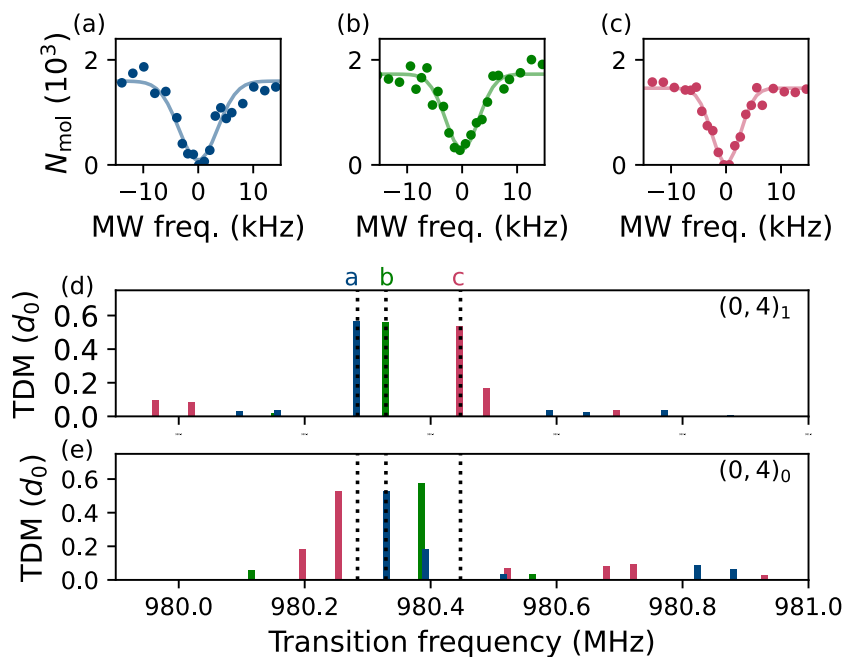


**Figure 6.9:** Ground state occupation after STIRAP transfer. (a-c) Microwave spectroscopy of the strongest three transitions between  $N'' = 0$  and  $N' = 1$ . Microwave frequencies given relative to the centre frequency of fitting. (d) and (e) present TDMs for each available transition from (d)  $(0, +4)_1$  and (e)  $(0, +4)_0$  states in units of molecule-frame dipole moment, calculated using [141]. Centre frequencies of (a-c) spectra are indicated by vertical dotted lines.  $\sigma^-$ ,  $\sigma^+$ , and  $\pi$  transitions from  $(0, +4)_1$  are coloured blue, red and green respectively.

After the STIRAP pulse sequence at 305 G using Stokes light polarised parallel to the quantisation axis tuned to the centre of the feature in Fig. 6.8(a), we apply an approximate  $\pi$  pulse in  $100 \mu\text{s}$  using our monopole antenna at frequencies around the strongest three rotational transitions and measure the molecular population. We repeat the process for different microwave frequencies. When microwaves are tuned on resonance with a transition, we observe a decrease in population as presented in Fig. 6.9(a-c). We

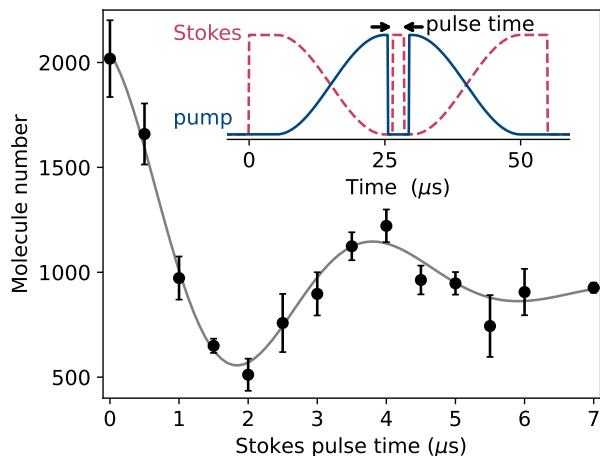


**Figure 6.10:** Rabi oscillation on Stokes transition at 305 G. Error bars are the result of the standard error of 3 repeat measurements. Inset presents the pulse sequence used.

fit each data with a Gaussian function and extract resonant frequencies of the transitions.

Given the polarisation of the Stokes light, we should be occupying an  $M_F = +4$  state after STIRAP transfer. Considering the good agreement with the theoretical transition frequencies shown in table 6.1, we can confirm our occupation of the  $(0, 4)_1$  state after STIRAP.

Using our results from microwave spectroscopy, we reference the Stokes detuning in Fig. 6.8 to the resonant frequency of the transition to the  $(0, 4)_1$  state. Despite the broad agreement with the relative detunings of the transitions, given the substantial transition dipole moments of transitions to other hyperfine states shown by the vertical lines in both Fig. 6.8(a) and (b), we expected to observe more features in our detuning range. We attribute the lack of features to the effects of interference between different STIRAP transfer channels [123, 211]. This can modify STIRAP efficiency and make spectroscopy features narrower. It's possible that our 100 kHz spacing in data collection is too large to resolve the narrower features that interference could cause.

$N'' = 1$ state, $(N'', M_F)_k$	$f_{\text{Theory}}$ (MHz)	$f_{\text{Exp}}$ (MHz)
$(1, 5)_2$	980.328	980.329(2)
$(1, 4)_3$	980.446	980.4474(13)
$(1, 3)_2$	980.282	980.2839(3)

**Table 6.1:** Rotational transition frequencies from  $(0, 4)_1$ .  $f_{\text{Theory}}$  and  $f_{\text{Exp}}$  correspond to the theoretical and experimental transition frequencies respectively.

$ \mathbf{B} /\text{G}$	Transition	Initial/final state	Excited state	$\text{Exp}_{\text{TDM}}$ ( $10^{-4}ea_0$ )
181.5	pump	$a^3\Sigma^+(-6(2,4) \text{ d}(2,4))$	$b^3\Pi_1(-1,3/2,7/2)$	8.1(1) [154]
	Stokes	$X^1\Sigma^+(0, 5)_0$		28.0(3) [154]
305	pump	$a^3\Sigma^+(-6(2,4) \text{ d}(1,3))$	$b^3\Pi_1(+1,1/2,5/2)$	7.2(1)
	Stokes	$X^1\Sigma^+(0, 4)_1$		5.1(6)

**Table 6.2:** Measured Transition dipole moments for STIRAP transitions at 181.5 and 305 G. Excited states are labelled by  $(M'_N, m'_{i_{\text{RB}}}, m'_{i_{\text{CS}}})$ .  $\text{Exp}_{\text{TDM}}$  is the transition dipole moment measured in experiment.

## 6.11 Stokes Rabi oscillation at 305 G

Finally, to fully characterise the STIRAP process at 305 G, we measure Rabi oscillations on the Stokes transition coupling to the  $(0, 4)_1$  state. To do this, we apply a square pulse of Stokes laser light between STIRAP pulses for various pulse times with the Stokes frequency locked to the centre of the feature in Fig. 6.8(a). We fit a Rabi frequency 250(7) kHz to the resulting oscillation presented in Fig. 6.10. This corresponds to an intensity normalised Rabi frequency of 0.40(5) kHz  $\sqrt{I_p / (\text{mWcm}^{-2})}$ .

Collating our results in table 6.2, we can see that our pump transition at 305 G has similar coupling strength to that used at 181.5 G however the Stokes transition is about a factor of 5 weaker. We attribute this to hyperfine state composition. The excited and ground states associated with the 305 G Stokes transition are not spin-stretched, leading to weaker coupling.

## 6.12 Summary

In summary, we have explored and characterised a procedure for RbCs ground state transfer that is compatible with the Innsbruck method for efficiently

mixing Rb and Cs BECs in an optical lattice. We have identified a route for accessing a bound state at 305 G which has desirable characteristics for high STIRAP ground state transfer efficiency. In accessing the appropriate bound state, we have developed a method to jump over an avoided crossing between the  $g_2$  and  $sd_6$  states at  $\sim 308$  G. We employed an RF-assisted avoided crossing protocol which traverses the avoid crossing with near 100% efficiency.

After we access a region where strong STIRAP coupling exists, we observe one-way transfer efficiencies of 85(4)% and 92(7)% for parallel and orthogonal Stokes polarisations respectively. To confirm the particular electronic and rovibrational ground state we occupy after STIRAP transfer, we performed microwave spectroscopy of the strongest available rotational transitions. Results of which coincide very well with our theoretical predictions of transition frequencies from  $(0, 4)_1$ , confirming our  $X^1\Sigma^+$  state occupancy. We directly measured the TDMs of both of the STIRAP transitions which are comparable to TDMs of the STIRAP transitions 181.5 G. This work lays the foundation for future experiments to load ground state RbCs into optical lattices efficiently.

# Chapter 7

## Synthetic Dimensions in RbCs

### 7.1 Introduction

Synthetic dimensions have become a burgeoning field of research in recent years due to their potential as a powerful tool for simulating models in condensed matter physics [212–214]. Moreover, combining real dimensional space with synthetic dimensions offers an exploration into higher-dimensional physics [94, 215, 216]. The concept simply put is using the internal quantum states of a system as a method of simulating real spatial dimensions, whereby each real dimension lattice site is mapped onto a quantum state. By coupling multiple states together, arbitrary geometries with a unique level of tunability are realised. Tuning the tunnelling rates in the real dimension can be simulated by adjusting the strengths of coupling between adjacent energy states. Additionally, on-site potentials can be controlled by adjusting the detunings of coupling fields. The ability to generate arbitrary structures in the synthetic dimension has sparked investigations in constructing complex and non-trivial topological arrangements [89, 92, 217–220].

Dipolar molecules offer a fantastic platform for creating synthetic dimensions in which rotational states are mapped to real dimensional sites. Rotational spacing is anharmonic, leading to specific addressing of couplings between rotational states with ease. The multitude of hyperfine states allows for the creation of topological structures with different dimensions [189].

In this chapter, we lay the groundwork for exploring synthetic dimensions in RbCs. We begin by giving an overview of the structure of RbCs in the context of realising synthetic dimensions. We discuss the complications that arise from off-resonant hyperfine state coupling in our experiment. Next, we

present results in controlling the relative site depth in the synthetic dimension by realising a two-level structure and changing the detuning of the coupling microwave field. We then demonstrate our control over hopping amplitudes in the synthetic dimension by adjusting the power of microwaves in a three-level system. Finally, we attempt to realise more complicated structures that exhibit non-trivial topological properties. These latter efforts ultimately fall short due to experimental complications.

## 7.2 Synthetic dimensions in RbCs

We utilise RbCs rotational energy levels as a platform for synthetic dimensions. Each rotational state is mapped onto discrete spatial positions of the analogous real dimension, for example, sites in an optical lattice as illustrated in Fig. 7.1. The lattice potential landscape can be described using two sets of parameters, the site-to-site hopping amplitudes and relative site depths.

For our model, we consider the sites to be degenerate in energy in the absence of detunings. The hopping parameters,  $t_{i,j}$  where  $i$  and  $j$  are site labels, are mapped onto the Rabi frequencies  $\Omega_{i,j}$  in the synthetic dimension. Likewise, the relative site depths in the real dimension  $V_i$  are controlled in the synthetic dimension by adjusting the detunings of microwaves that couple neighbouring rotational states. This is made evident by examining the Hamiltonians describing the real and synthetic dimensions. The Hamiltonians that describe four different synthetic lattice sites/rotational states in the bases  $\{|1\rangle, |2\rangle, |3\rangle, |4\rangle\}$  and  $\{|N'' = 1\rangle, |N'' = 2\rangle, |N'' = 3\rangle, |N'' = 4\rangle\}$  respectively are

$$\hat{H}_{\text{Lattice}} = \begin{pmatrix} V_1 & t_{12} & 0 & 0 \\ t_{12} & V_2 & t_{23} & 0 \\ 0 & t_{23} & V_3 & t_{34} \\ 0 & 0 & t_{34} & V_4 \end{pmatrix} \quad (7.1)$$

$$\hat{H}_{\text{Synth}} = \frac{\hbar}{2} \begin{pmatrix} 0 & \Omega_{12} & 0 & 0 \\ \Omega_{12} & -2\Delta_{12} & \Omega_{23} & 0 \\ 0 & \Omega_{23} & -2(\Delta_{12} + \Delta_{23}) & \Omega_{34} \\ 0 & 0 & \Omega_{34} & -2(\Delta_{12} + \Delta_{23} + \Delta_{34}) \end{pmatrix}, \quad (7.2)$$

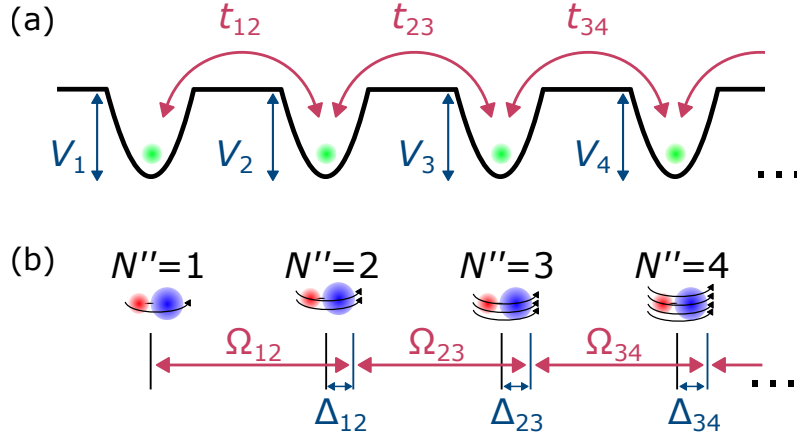


**Figure 7.1:** Synthetic dimension mapping. (a) Real spatial dimension of a 1-dimensional lattice potential.  $t_{i,j}$  and  $V_i$  correspond to hopping amplitudes between synthetic sites  $i$  and  $j$  and the site depth of  $i$  respectively. (b) Synthetic dimension of rotational states of RbCs.  $\Omega_{i,j}$  denotes the Rabi frequency coupling states  $i$  and  $j$ .  $\Delta_{i,j}$  is the relative detuning of the photon coupling states  $i$  and  $j$ .

where  $\hat{H}_{\text{Lattice}}$  and  $\hat{H}_{\text{Synth}}$  are the lattice and synthetic dimensional Hamiltonians respectively. Eigenvalues and eigenstates for  $\hat{H}_{\text{Synth}}$  are presented analytically in chapter 9 for systems of up to 4 synthetic lattice sites in the absence of detunings.

However, the complex hyperfine structure of RbCs complicates the synthetic dimension framework. When coupling between different rotational states, we resolve the hyperfine structure, leading to off-resonant coupling to nearby hyperfine states. We build our synthetic dimension using spin-stretched states (“target” states). The nearest states we can off-resonantly couple to are presented in Fig. 7.2. Owing to a microwave source with poorly defined polarisation, discussed in chapter 3, we have the possibility of coupling to various hyperfine states. However, target states are typically 10 kHz to 100 kHz from neighbouring hyperfine states and the transition dipole moments (TDMs) of the target transitions are substantially larger than transitions to other states, making this problem negligible for the majority of the experiments performed in this chapter.

When constructing our synthetic dimensions, we determine the resonant frequencies of transitions by performing microwave spectroscopy for each transition in isolation using 1 ms square microwave pulses. The transition frequency is typically known to  $<100$  Hz. We then calibrate Rabi frequencies by performing a series of Rabi oscillations on the respective transitions in

isolation for different microwave powers.

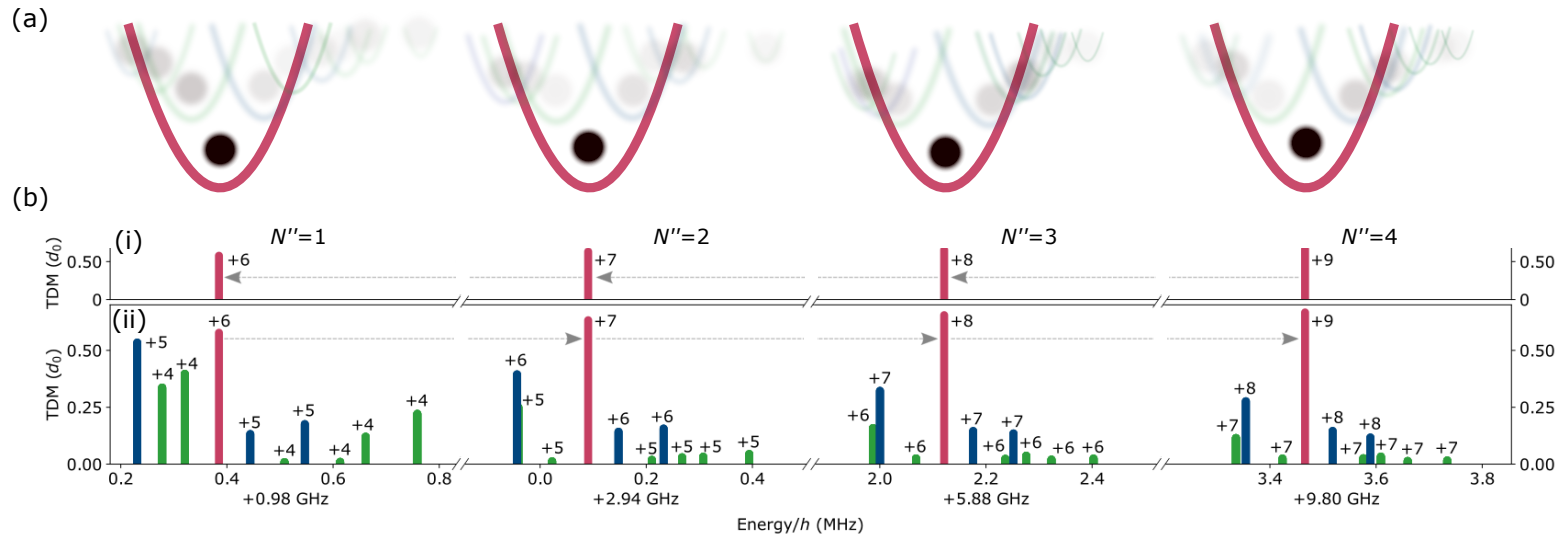


**Figure 7.2:** Rotational synthetic dimension map in RbCs. (a) Real dimension hopping analogue to our rotational synthetic dimension. Our target sites are presented as the red potentials. However, off-resonant coupling to neighbouring hyperfine states leads to the occupation of other sites, shown as the faint blue and green parabolas. Relative detuning and coupling in the synthetic dimension with respect to the target state are presented as relative depths of sites and opacity respectively. (b) Available hyperfine states in our synthetic dimension, going (i) down and (ii) up in rotational quantum number at 181.5 G. States are presented as vertical lines with their relative heights of each line denoting their TDM when coupling to an  $\Delta N = \pm 1$  target states in units of the molecule’s lab frame dipole moment ( $d_0 = 1.23$  D). Red lines are the spin-stretched target states of each rotational energy level. Grey arrows link the spin-stretched states and indicate the direction of transition. Blue and green lines in each  $N''$  section represent  $\pi$  and  $\sigma_-$  transitions from the  $N''-1$  rotational energy level respectively. Each line is labelled by the  $M_F''$  quantum number.

### 7.3 Controlling relative synthetic lattice site depths

We control the relative site depths in our synthetic dimension by tuning the frequency of the microwaves that couple adjacent rotational states. We create a synthetic dimension using the spin-stretched states ( $N'' = 1$ ,  $M_F'' = 6$ ) and (2,7). The synthetic dimension is then ‘probed’ using the (0,5)  $\rightarrow$  (1,6) transition with Rabi frequency  $\Omega_p$ . We occupy the regime where  $\Omega_p \ll \Omega_{i,j}$  for all combinations of  $i$  and  $j$  so that we consider (0,5) to be isolated from the synthetic dimension. By varying the detuning of the probe transition  $\Delta_p$  and measuring the population of the (0,5) state, we observe features corresponding to eigenenergies of the synthetic dimension.

We connect the MXG signal generator to the monopole antenna to produce microwaves that drive the (0,5)  $\rightarrow$  (1,6) transition with the MXG power set that  $\Omega_p \sim 0.5$  kHz when on resonant. An output of a WindfreakV2 is connected to the microwave horn which drives the (1,6)  $\rightarrow$  (2,7) transition. We fix the value of  $\Omega_{12}$  to  $\sim 2.2$  kHz, the exact values of  $\Omega_p$  and  $\Omega_{12}$  are extracted from the fitting of the data set.

We begin by fixing the frequency of the microwaves driving the (1,6)  $\rightarrow$  (2,7) transition to 2.5 kHz above the resonant frequency ( $\Delta_{12} = +2.5$  kHz). We then perform a square pulse of both microwaves for 1 ms in free space. Next, we vary the value of  $\Delta_p$  in 0.375 kHz steps and measure the ground state population for three repeats, producing the spectroscopy represented by the bottom row in Fig. 7.3(b). We then repeat the process for different values of  $\Delta_{12}$ . The data presented in (b) is then fitted simultaneously extracting  $\Omega_p = 0.52(2)$  kHz and  $\Omega_{12} = 2.14(2)$  kHz. These fitting parameters are then used to produce the theory plot presented in Fig. 7.3(a).

By considering the eigenvectors of our two-level system, given in chapter. 9, we can relate our results to the real dimensional analogue. As we vary  $\Delta_{12}$ , we are effectively changing on-site potentials in our synthetic dimension. If we vary  $\Delta_{12}$  from far red (blue) detuning regime to blue (red), a particle in the real dimension exchanges most probable site occupancy.

### 7.4 Controlling synthetic lattice site hopping

We control the hopping amplitudes in our synthetic dimension by changing the Rabi frequency of the coupling between adjacent rotational states.

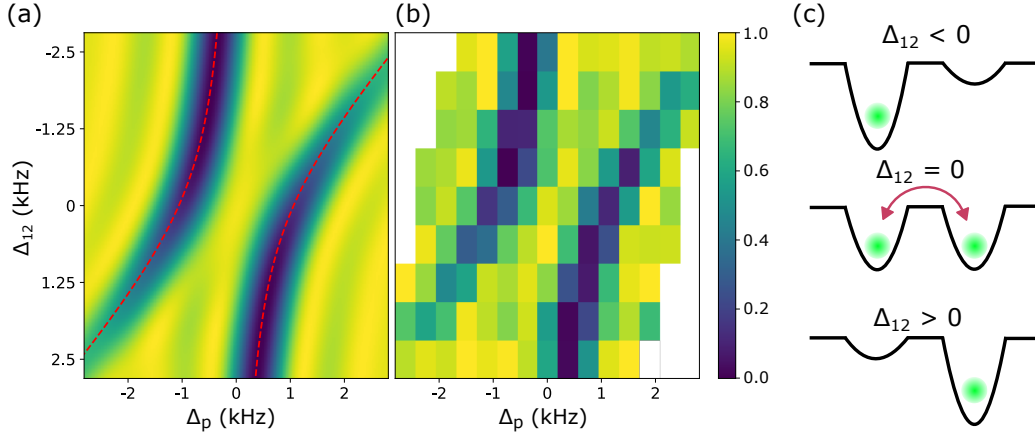


**Figure 7.3:** Controlling relative site depths in a two-site synthetic dimension. (a) Theoretical modelling and (b) experimental results of ground state population  $N_{\text{pop}}/N_{\text{pop}}^{\text{tot}}$  represented by colour as a function of  $\Delta_p$  and  $\Delta_{12}$ . Red dotted lines in (a) indicate the eigenvalues of each eigenvector. (c) Cartoon of analogous real dimension. As the value of  $\Delta_{12}$  varies from red (blue) detuning regime to blue (red), a particle changes most probable site occupation.

This is accomplished by simply tuning the power of the microwave generators. We create a synthetic dimension that comprises (1,6), (2,7) and (3,8) spin-stretched states. As in section 7.3, we employ a probe microwave field, coupling (0,5) and (1,6) states with a Rabi frequency  $\sim 0.625$  kHz when on resonance. This value was chosen to increase the depth of the spectroscopic features we expect to observe. Both outputs of a WindfreakV2 microwave generator are combined using a power splitter (Mini-circuits ZFRSC-183-S+) which is subsequently connected to the microwave horn that drives the (1,6)  $\rightarrow$  (2,7) and (2,7)  $\rightarrow$  (3,8) transitions.

We fix the value of  $\Omega_{12}$  to  $\sim 2.2$  kHz and set the  $\Omega_{23}$  to 0 kHz by having the microwaves coupling the (2,7) and (3,8) states off. We perform a 1 ms square pulse of both microwaves in free space and measure the ground state population for different values of  $\Delta_p$ . With  $\Omega_{23} = 0$  kHz, we revert to a two-level Autler-Townes splitting as observed in Fig. 7.3.

We then apply microwaves resonant with the (2,7) $\rightarrow$ (3,8) transition during the 1 ms microwave pulse and repeat for various WindfreakV2 powers, producing the spectra presented in Fig. 7.4(b).  $\Omega_{23}$  is varied linearly up to an expected  $\Omega_{23}/\Omega_{12}$  ratio of 2. We then fit all spectra simultaneously, extracting values of  $\Omega_p = 0.588(10)$  kHz,  $\Omega_{12} = 2.32(2)$  kHz and  $\Omega_{23}^{\text{Max}} = 4.44(10)$  kHz.  $\Omega_{23}^{\text{Max}}$  is the maximum value of  $\Omega_{23}$  we obtain. From these fitted values, we

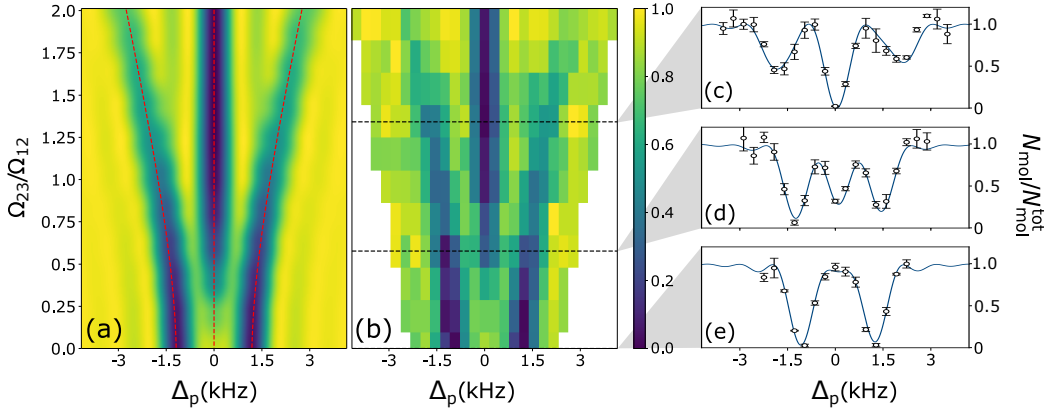


**Figure 7.4:** Controlling the hopping between adjacent sites in the synthetic dimension. (a) Theoretical modelling and (b) experimental results of  $N_{\text{pop}}/N_{\text{pop}}^{\text{tot}}$  represented by colour as a function of  $\Delta_p$  and  $\Omega_{23}/\Omega_{12}$ . Red dotted lines in (a) denote the eigenvalues of each eigenvector of the three-level model described in the text. (c-e) Example spectra data for (c)  $\Omega_{23}/\Omega_{12} = 1.35(3)$ , (d)  $\Omega_{23}/\Omega_{12} = 0.77(2)$  and (e)  $\Omega_{23}/\Omega_{12} = 0$ .

report the maximum ratio of  $\Omega_{23}$  to  $\Omega_{12}$  of  $1.91(5)$ . Using the parameters extracted from the fit, we produce the corresponding theory plot illustrated in Fig. 7.4(a). As we increase the ratio  $\Omega_{23}/\Omega_{12}$ , we begin to observe a feature at  $\Delta_p = 0$  as illustrated in Fig. 7.4(c-e) which is composed of only  $|N'' = 1\rangle$  and  $|N'' = 3\rangle$ .

## 7.5 SSH model

The Su-Schrieffer-Heeger (SSH) model, devised by W. P. Su, J. R. Schrieffer and A. J. Heeger in 1979 [221, 222] is a model that describes the effects of doping on the electrical conductivity of a polyacetylene,  $(\text{CH})_x$ , molecule. The polyacetylene structure is that of periodic alternating weak and strong bonds linking adjacent Carbon atoms. A simple analogy of the tight-binding model is often presented when describing the SSH whereby the state of an electron in a 1-dimensional crystal lattice with a two-site unit cell is considered. Inter and intra-cell hopping amplitudes are denoted as  $v$  and  $w$  respectively. Plotting out the energy dispersion relation across the Brillouin zone, in the cases where  $w \neq v$ , a band gap is present. However, if  $w = v$  there is no gap. As such, the act of varying the ratio of  $w/v$  elicits an insulator  $\leftrightarrow$  conductor transition.

Depending on the boundary conditions, the SSH becomes one of the sim-

plest models to exhibit non-trivial topological properties, indicated by the existence of ‘edge-states’ at zero energy. These edge states are remarkably robust to local deformations of the SSH structure such as changes in bulk hopping amplitudes and site depths. This robustness is linked to the topological nature of the SSH model and is hence termed ‘topological protection’ [223]. The conditions for realising a non-topological structure is that an even number of sites are present and the couplings to the edge sites in the finite chain are weak. Topological protection has been demonstrated using SSH structured synthetic dimensions manufactured from momentum states in BECs [224], photonic lattices [225] and Rydberg atom states [92].

In RbCs, we construct a 4-level synthetic dimension using the  $N'' = 1$  to  $N'' = 4$  spin-stretched states. We employ a second WindfreakV2 output and power splitter to combine the three RF signals that drive the transitions in our SSH, which is then connected to our microwave horn. Microwaves coupling neighbouring rotational states are set to resonance. We set the  $\Omega_{12} = \Omega_{34} \sim 2$  kHz. The form of Eq. 7.2 that describes our SSH is

$$\hat{H}_{\text{SSH}} = \frac{\hbar}{2} \begin{pmatrix} 0 & \Omega_A & 0 & 0 \\ \Omega_A & 0 & \Omega_B & 0 \\ 0 & \Omega_B & 0 & \Omega_A \\ 0 & 0 & \Omega_A & 0 \end{pmatrix}, \quad (7.3)$$

where  $\Omega_A = \Omega_{12} = \Omega_{34}$  and  $\Omega_B = \Omega_{23}$ . In the real dimension analogue,  $t_{12} = t_{34} = v$  and  $t_{23} = w$ .

As we perform spectroscopy of the  $(0, 5) \rightarrow (1, 6)$  transition with  $\Omega_p \sim 0.7$  kHz and  $\Omega_A \sim 1.6$  kHz as a function of  $\Omega_B/\Omega_A$ , we expect to recover the plot illustrated in Fig. 7.5(a). In the region  $\Omega_B \gg \Omega_A$ , we revert to an Autler-Townes doublet. In the real dimension, this corresponds to a dimerised configuration of two pairs of sites in isolation, as presented in Fig. 7.5(b). As  $\Omega_B/\Omega_A$  increases, we transition from a topologically trivial to a non-trivial regime where two eigenvalues corresponding to edge states tend to zero energy and valence/conduction band eigenvalues diverge.

However, we instead observed a drastic asymmetry in the resulting spectra, to such an extent that at regions of  $\Omega_B/\Omega_A \sim 3$ , we could not resolve valence and conduction band features. We therefore did not continue to produce a full mapping of Fig. 7.5(a) experimentally. We attribute this problem to deviations in Rabi frequencies in our SSH after calibration. This could be in part due to changes in the attenuation from the path of the microwave

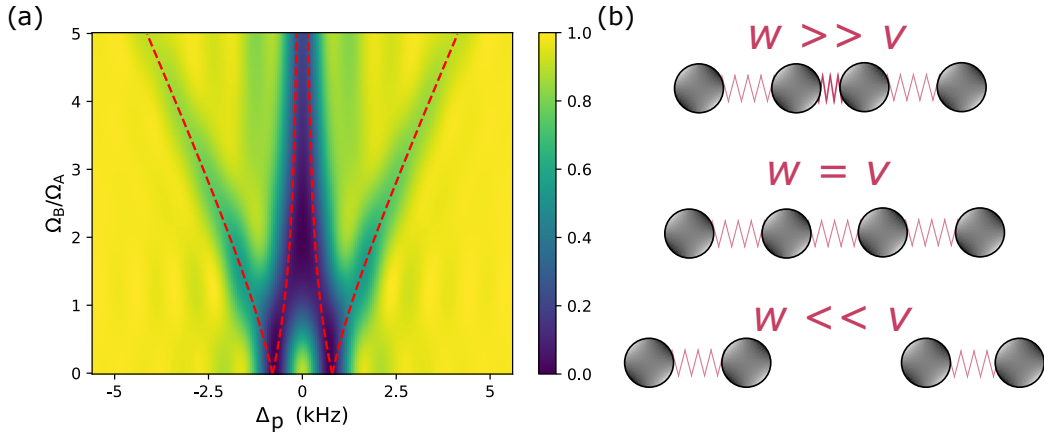


**Figure 7.5:** Probing the SSH synthetic dimension. (a) Theoretical plot of  $\Delta_p$  as a function of the ratio  $\Omega_B/\Omega_A$  up to  $\Omega_B/\Omega_A = 5$ . The colour indicates the ground state population,  $N_{\text{mol}}/N_{\text{mol}}^{\text{tot}}$ . Red dotted lines indicate the eigenvalues of eigenstates. (b) Cartoon of real dimension structure for different regimes of  $\Omega_B/\Omega_A$  ( $w/v$ ).

generator to the source. The calibration involved Rabi oscillations on transitions in isolation. Our RF combining setup may attenuate signals differently when all microwaves are on. Secondly, the Rabi frequencies drifted noticeably over a few hours, presumably due to sensitive connections between the microwave generators and the emitters. For future attempts at realising the SSH, power calibration should be performed with Rabi oscillations with all microwaves on but with relevant microwaves detuned. Care should be taken to not adjust the connections in the microwave setup to avoid unwanted Rabi frequency drifts after calibration.

## 7.6 Summary

In this chapter, we presented a method of realising synthetic dimensions using rotational states of RbCs. We began by outlining the structure of RbCs in the context of engineering synthetic dimensions, highlighting the complexities caused by hyperfine levels.

Next, we demonstrated our ability to control relative site depths in the synthetic dimension by changing the detunings of microwaves that couple neighbouring rotational states in a two-level system. We then demonstrated our methods of controlling hopping amplitudes in the synthetic dimension by adjusting the relative microwave powers. These proof-of-concept measure-

ments show the versatility and relative ease that the structure of synthetic dimensions can be adjusted. We then discussed the construction of non-trivial topological structures in our synthetic dimension. When attempted to be realised experimentally, we encountered difficulty.

We contextualise our results as an immediate outlook for future experiments using a more robust experimental setup. The chief improvement would involve producing a microwave source with robust output power and well-defined polarisation, avoiding off-resonant couplings to non-spin-stretched hyperfine states when larger Rabi frequencies are involved. This will be accomplished in future using the newly installed dipole antenna array described in chapter 3.

# Chapter 8

## Conclusion

Our goal throughout this work has been to access dipolar interactions in RbCs molecules and to develop methods of producing a sample of optically confined molecules. Dipolar interactions in a lattice provide a fantastic platform for performing quantum simulation experiments. Moreover, coupling multiple rotational states together to realise a synthetic dimension can be used in isolation and alongside the spatial lattice dimension to explore new physics.

### 8.1 Summary

We began this thesis by outlining the theoretical framework used throughout. We discussed the internal structure of RbCs molecules and how applying external fields can be used to encode pseudo-spins that form the foundation for quantum simulation experiments with the addition of dipolar interactions.

In chapter 3, we introduced our experimental setup. We outlined the typical experimental sequence carried out to produce and image ground state molecules. Towards the end of chapter 3, we presented work on maintaining and improving the experiment by installing new atomic dispensers, a new ion pump and a dipole antenna array. The dipole array will be used in the future to engineer a microwave source with well-defined polarisation, beneficial for coupling rotational states with high fidelity.

Spurred on by theoretical calculations performed by Guan *et al.* [172], we performed a comprehensive investigation into the electronic transitions used to create a rotationally magic trap for RbCs. We set up two new laser locking mechanisms and used the effects of photon scattering to identify  $X^1\Sigma^+(v'' = 0) \rightarrow b^3\Pi_0(v' = 0, 1, 2)$  transitions with hyperfine state resolu-

tion. By performing spectroscopy from different ground states, we extracted effective rotational constants for the  $b^3\Pi_0(v' = 0, 1)$  states. We observed ac Stark shifts in STIRAP transitions and lifetimes of ground state molecules in the presence of the probe light to extract partial and total linewidths. Using microwave spectroscopy on the  $(0,5) \rightarrow (1,6)$  transition, we coarsely mapped out differential ac Stark shifts in the presence of probe light around transitions to low-lying vibrational states of  $b^3\Pi_0$  in order to identify rotationally magic detunings. By increasing the probe beam intensity and repeating the measurement for different combinations of rotational states, we observed a detuning which is nearly magic for many rotational states. Finally, we performed a series of Ramsey interferometry experiments using different rotational states to demonstrate rotational coherence time is maximised when molecules are illuminated with light at a magic detuning.

Following our spectroscopic measurements in chapter 4, we trapped our molecular sample in a crossed-optical dipole trap which could be tuned to the rotationally magic frequency for different pairs of low-lying rotational states. First, we demonstrated our trap was compatible with long sample lifetimes by observing molecule population in the trap as a function of time for both magic wavelength light and 1064 nm light with matching trap frequencies. We repeat the measurement in the magic trap with a dipolar mixture, observing a faster loss rate, coinciding with results demonstrated by Gregory *et al.* [185]. Next, we performed a set of Ramsey measurements on molecules in the magic trap using a superposition of different rotational states. The Ramsey fringe contrast is maximised at the magic frequency for each pair of states, signifying the detuning which would result in a maximum coherence time. We then trapped our molecular sample in a non-dipolar superposition, observing coherence times of  $>1.4$  s at the 95% confidence interval. When we performed the same experiment with a dipolar superposition, we observed a substantial reduction in coherence time, confirming the existence of long-range dipole-dipole interactions in our sample. We then coarsely adjusted the strength of dipole-dipole interactions by preparing different superpositions of rotational states. We observed a coherence time proportional to the reciprocal of the dipole moment squared.

In chapter 6, we demonstrated a route to ground state RbCs in collaboration with researchers at the University of Innsbruck that is compatible with the Innsbruck method for loading RbCs Feshbach molecules into a lattice demonstrated by Reichsöllner and Schindewolf *et al.* in [50]. We began by outlining the procedure conducted in [50]. Next, we identified the magnetic fields where interspecies Feshbach resonances exist by observing the effects of

three-body loss when tuning the external magnetic field close to a Feshbach resonance. We then associated atoms into molecules using the Feshbach resonance 352.74 G and performed a series of spectroscopy experiments on the pump transition as a function of magnetic field. We observed that the Feshbach molecule population followed an avoided crossing between the ds6 and g2 states, away from the sd6 state with desirable characteristics for STIRAP. We jumped the avoided crossing with the addition of an RF-photon and accessed the sd6 state, following a procedure demonstrated in [208]. Next, we directly measured the diagonal and off-diagonal elements of the STIRAP Hamiltonian by performing spectroscopy and Rabi oscillations on the pump and Stokes transitions. We identified the ground state occupancy after STIRAP by performing spectroscopy on microwave transitions from the ground state.

In chapter 7, we explored utilising rotational states of RbCs as a platform for synthetic dimensions. We demonstrated how changing the Rabi frequencies and detunings of microwaves that couple adjacent rotational states can be adjusted to vary hopping amplitudes and site depths in our synthetic dimension. These results form the basis for realising arbitrary and non-trivial geometries in which to investigate new physics.

## 8.2 Outlook

The work in this thesis presents a key milestone in utilising RbCs molecules in quantum science. The advent of a rotationally magic trap could form the basis for many exciting experiments to come. The procedure of loading molecules into lattices outlined in chapter 6 could be applied to a lattice of rotationally magic wavelength and the multiply rotationally magic detuning window presents a fantastic opportunity for performing interacting synthetic dimension experiments.

### 8.2.1 Plans for a magic lattice

The immediate plan for the bulk gas laboratory in Durham is to install a magic optical lattice. The Innsbruck method for loading molecules into lattices using 1064 nm light applies to loading with 1145 nm given their similar polarisabilities at these wavelengths [226]. Also, the agreement between magnetic moments of  $b^3\Pi_0(v' = 0, 1, 2, N' = 0)$  states calculated in chapter 4 implies the magic detuning for a given pair of states and polarisation shouldn't vary drastically between 181.5 G and 305 G. Initially, a 1-dimensional (1D)

vertical lattice will be installed and subsequent horizontal lattices will be added using a bow-tie configuration. However, the installation of a simple 1D magic lattice brings with it many interesting prospects.

### 8.2.2 Interactions in 1D lattice pancakes.

The lattice geometry we expect from our single retro-reflected beam is that of pancakes. Molecules are confined to flat disks with periodic  $\lambda/2$  spacing in the axis of propagation of the trapping beams. We propose a possible experiment which probes the inter and intra-pancake dipolar interactions as illustrated in Fig. 8.1. First, ground state molecules are loaded into the lattice sites. A separate ‘shift’ beam is applied to  $\sim$  half the sites, causing ac Stark shifts in energy states of the molecules in these sites. A resonant microwave field coupling ( $N'' = 0$ ,  $M_F'' = 5$ ) to a (1,5) state is then applied, creating an equal superposition of (0,5) and (1,5) states for the molecules in sites with the absence of the shift beam. The process is repeated but ac Stark shifted regions swapped and resonant microwaves driving the (0,5)  $\rightarrow$  (1,6) transition is applied, creating a superposition between (0,5) and (1,6).

With the shift beam turned off, dipole-dipole interactions between molecules confined to the same pancake and molecules of neighbouring pancakes will cause decoherence of Ramsey fringes. Interacting dipoles of different superpositions only occur if the  $N'' = 1$  states are degenerate. This condition can be accessed using an external magnetic or electric field. In this case, five dipolar interaction terms are present. Interactions between molecules of (0,5) and (1,5) superpositions in the same lattice site and between neighbouring lattice sites,  $V_{dd}^\pi$  and  $V_{dd}^{\pi*}$  respectively as presented in Fig. 8.1(c). Similar terms correspond to molecules occupying (0,5) and (1,6) superpositions. Finally, a  $V_{dd}^{\sigma/\pi*}$  term corresponds to dipolar interactions between sites at the boundary of the different superpositions.

The choice of states, regions shifted and timings between microwave pulses can be used in tandem to produce a highly-tunable XXZ Hamiltonian, similar to the systems described in [85, 227] with extra terms relating to different dipolar interactions.

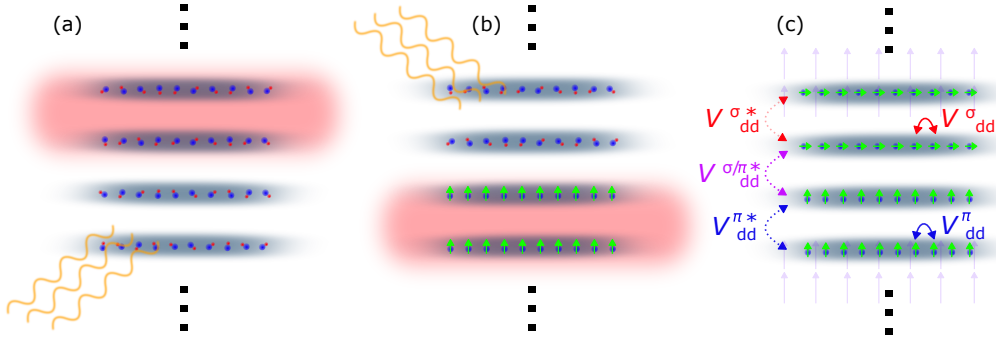


**Figure 8.1:** Interacting lattice pancakes. Molecules confined to optical lattice pancakes spatially separated by  $\lambda/2$ . (a) Molecules in the upper group of pancakes are ac Stark shifted, effectively detuning the microwaves that excite a  $\pi$  transition between rotational states in the lower pancake population. (b) The process is repeated but swapping the ac Stark shifted regions and driving a  $\sigma$  transition. (c) With the ac Stark shifting beam turned off, inter and intra-pancakes dipole-dipole interactions occur. At the boundary between the ac Stark shifted regions in (a) and (b), inter-pancake dipole-dipole interactions comprise dipoles rotating both around the quantisation axis and oscillating parallel to the quantisation axis providing an external field makes the  $N'' = 1$  states degenerate, as presented by the faint purple arrows.

### 8.2.3 3-level interacting system

The proximity of magic detunings for different combinations of rotational states are presented in chapter 5 provide an exciting prospect. A superposition of three (or more) rotational energy states in a magic potential could facilitate the observations of interactions in systems no longer described by spin-1/2 formalisation.

The theory presented in chapter 4 dictates that magic detunings are defined by the  $N''$  and  $M_N''$  quantum numbers. To achieve the longest coherence time between three rotational states, it's desirable to use two  $N'' = 0$  states as each will have a well-defined  $M_N''$  of 0. In Fig. 8.2, we illustrate a possible three-level  $\Lambda$ -type system that uses two  $N'' = 0$  states.

In our proposal, we consider states that are coupled via one  $\sigma^-$  and one  $\sigma^+$  transition as presented in Fig. 8.2(a). States in the figure are labelled using  $N''$  and  $M_F''$ . The value of the subscript  $k$  can be tailored in accordance with the optimal suppression of off-resonant couplings and the desired strengths of dipolar interactions. If a superposition of states was created using the  $\sigma^-$  transition, rotating dipoles in Fig. 8.2(b)(i) would result. However, rotating

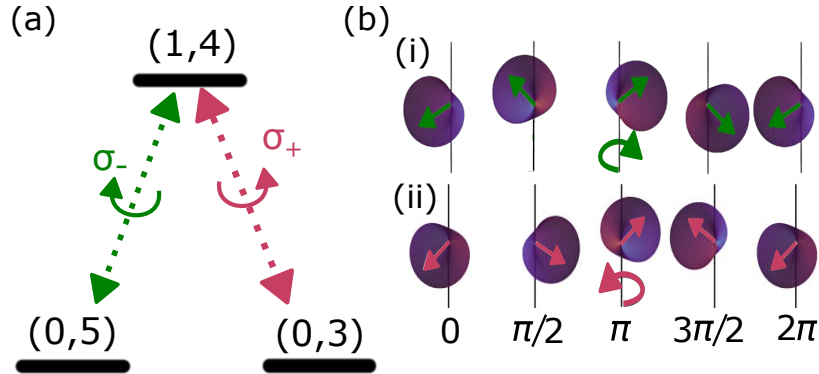


**Figure 8.2:** Interacting three-level system. (a) Possible  $\Lambda$ -type rotational energy level system.  $\sigma^-$  transition from the absolute ground state (0,5) to a (1,4) state which is in turn coupled to a (0,3) state. (1,4)  $\rightarrow$  (0,3) is a  $\sigma^+$  transition. Subscripts  $k$  for each state omitted. (b) Rotating dipole superpositions created using (i)  $\sigma^-$  and (ii)  $\sigma^+$  transitions.

dipoles in Fig. 8.2(b)(ii) would result from creating a superposition using the  $\sigma^+$  transition. This system is realised when the two states in  $N'' = 0$  are separated in energy on the order of dipolar interaction strength, which could be accomplished with the addition of an external field.

Generating a superposition of all three states produces long-range interactions described by spin-1 interacting Hamiltonians such as the Bose-Hubbard Hamiltonian [228, 229]. Hyperfine state-selective coupling forms an ideal platform for realising tunable spin-1 interacting systems.

### 8.2.4 Interacting SSH model

The addition of dipolar interactions enriches synthetic dimension systems, creating energy perturbations on the synthetic lattice sites. Topologically trivial and non-trivial phase transitions can be mediated by interactions between particles on synthetic lattice sites [91] and interacting synthetic dimensions in Rydberg atoms demonstrated that controlling the relative strengths of dipolar interactions and hopping amplitudes suppresses hopping in the synthetic dimension [92].

Considering a four-level SSH synthetic dimension structure with dipolar interactions as illustrated in Fig. 8.3, we can begin to realise many-body Hamiltonians that capture topological insulator phase transitions [230].

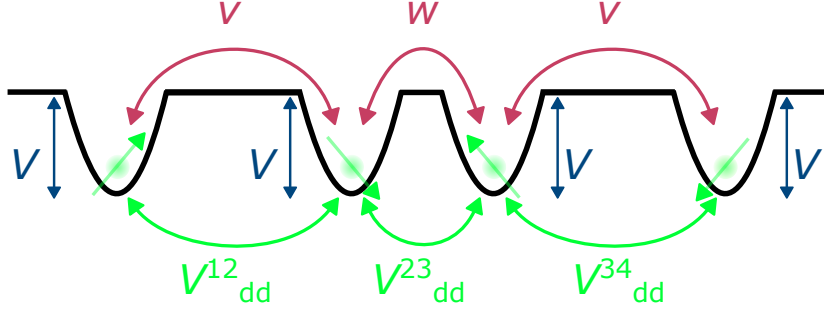


**Figure 8.3:** Interacting SSH model. Real dimension analogue of the synthetic dimension that comprises four rotational states in an SSH configuration. Dipole-dipole interaction between sites  $i$  and  $j$ ,  $V_{\text{dd}}^{ij}$ , can be tuned using different rotational states and relative microwave phase relations. The inter-site hopping terms  $v$  and  $w$  are tailored using different microwave powers with  $w \gg v$  to enter the SSH regime. The depths of sites  $V$  are all degenerate however, the addition of dipolar interactions breaks this degeneracy.

$$\hat{H}_{\text{SSH}^*} = \sum_{\langle i,j \rangle} \left( t_{ij} \hat{c}_j^\dagger \hat{c}_i + \text{h.c.} \right) + V_{\text{dd}}^{ij} \sum_{\langle i,j \rangle} \hat{n}_i \hat{n}_j, \quad (8.1)$$

where  $\langle i, j \rangle$  represents the nearest-neighbour sites  $i$  and  $j$ ,  $\hat{c}_j^\dagger (\hat{c}_i)$  are the fermionic creation (annihilation) operator of the lattice site  $i$  and h.c. is the hermitian conjugate.  $t_{ij}$  are replaced with  $v$  and  $w$  in the SSH model with  $w \gg v$ .  $V_{\text{dd}}^{ij}$  is the dipolar interaction between sites  $i$  and  $j$  and  $\hat{n}_i$  is the number operator at site  $i$ .

### 8.3 Concluding remarks

In this work, we have presented methods of accessing long-range dipole-dipole interactions between RbCs molecules, a key milestone in realising their applications for quantum science. We have explored the structure of the excited state potential that is used to produce rotationally magic traps and chartered a possible avenue for producing ground state RbCs in an optical lattice. Utilising the tools presented in this thesis opens up new grounds for future exploration of quantum science with ultracold molecules. The field is growing evermore expansive and groups around the world are producing beautiful results, encouraging other researchers to examine the rich quantum landscape ultracold polar molecules have to offer.

# Chapter 9

## Appendix

### 9.1 Analytical solutions to multi-level systems

We present the analytical solutions for eigenvalues and eigenvectors of systems which comprise multiple rotational states. We have adopted the convention that eigenvalues,  $\lambda$ , are numbered from the lowest to highest energy, i.e the energy of  $\lambda_1 <$  the energy of  $\lambda_2 <$   $\lambda_3$  etc. The eigenstate with eigenenergy  $\lambda_1$  is  $|\Psi_1\rangle$  etc. For systems involving  $>2$  rotational states, we have set the detunings of coupling microwaves to zero. We label the Rabi frequency coupling neighbouring rotational states and the detuning on the microwaves as  $\Omega_{ij}$  and  $\Delta_{ij}$  respectively, where  $i$  and  $j$  correspond to the connected states  $N$  and  $N + 1$ . However, for the SSH model, it's more appropriate to use the notation  $\Omega_A$  and  $\Omega_B$  where  $\Omega_A = \Omega_{12} = \Omega_{34}$  and  $\Omega_B = \Omega_{23}$ .

#### 9.1.1 2-level eigenvalues and eigenvectors

The 2-level system is equivalent to Autler-Townes splitting.

$$E_{0,1} = \frac{-\Delta_{12}}{2} \pm \frac{\sqrt{\Omega_{12}^2 + \Delta_{12}^2}}{2} \quad (9.1)$$

$$|\Psi_1\rangle = \frac{\Delta_{12} - \sqrt{\Omega_{12}^2 + \Delta_{12}^2}}{\Omega_{12} \sqrt{1 + \left| \frac{\Delta_{12} - \sqrt{\Omega_{12}^2 + \Delta_{12}^2}}{\Omega_{12}} \right|^2}} |N=1\rangle + \frac{1}{\sqrt{1 + \left| \frac{\Delta_{12} - \sqrt{\Omega_{12}^2 + \Delta_{12}^2}}{\Omega_{12}} \right|^2}} |N=2\rangle \quad (9.2)$$

$$|\Psi_2\rangle = \frac{\Delta_{12} + \sqrt{\Omega_{12}^2 + \Delta_{12}^2}}{\Omega_{12} \sqrt{1 + \left| \frac{\Delta_{12} + \sqrt{\Omega_{12}^2 + \Delta_{12}^2}}{\Omega_{12}} \right|^2}} |N=1\rangle + \frac{1}{\sqrt{1 + \left| \frac{\Delta_{12} + \sqrt{\Omega_{12}^2 + \Delta_{12}^2}}{\Omega_{12}} \right|^2}} |N=2\rangle \quad (9.3)$$

### 9.1.2 3-level eigenvalues and eigenvectors

The 3-level analytical solutions are equivalent to that in the STIRAP  $\Lambda$ -type scheme.

$$\lambda_1 = -\frac{\sqrt{\Omega_A^2 + \Omega_B^2}}{2} \quad (9.4)$$

$$\lambda_2 = 0 \quad (9.5)$$

$$\lambda_3 = \frac{\sqrt{\Omega_A^2 + \Omega_B^2}}{2} \quad (9.6)$$

$$|\Psi_1\rangle = \frac{1}{\sqrt{2}} \left[ \frac{\Omega_A}{\sqrt{\Omega_A^2 + \Omega_B^2}} |N=1\rangle - |N=2\rangle + \frac{\Omega_B}{\sqrt{\Omega_A^2 + \Omega_B^2}} |N=3\rangle \right] \quad (9.7)$$

$$|\Psi_2\rangle = -\frac{\Omega_B}{\sqrt{\Omega_A^2 + \Omega_B^2}} |N=1\rangle + \frac{\Omega_A}{\sqrt{\Omega_A^2 + \Omega_B^2}} |N=3\rangle \quad (9.8)$$

$$|\Psi_3\rangle = \frac{1}{\sqrt{2}} \left[ \frac{\Omega_A}{\sqrt{\Omega_A^2 + \Omega_B^2}} |N=1\rangle + |N=2\rangle + \frac{\Omega_B}{\sqrt{\Omega_A^2 + \Omega_B^2}} |N=3\rangle \right] \quad (9.9)$$

### 9.1.3 4-level SSH eigenvalues and eigenvectors

We have labelled the eigenvalues and eigenstates in accordance with their topological significance instead of their number, i.e  $|\Psi_{\text{Valence}}\rangle$  instead of  $|\Psi_1\rangle$  etc.

$$\lambda_1 = \lambda_{\text{Valence}} = \frac{1}{4} \left( -\sqrt{4\Omega_A^2 + \Omega_B^2} - \Omega_B \right) = -\frac{\Omega_A}{4} \left( R + \sqrt{R^2 + 4} \right) \quad (9.10)$$

$$\lambda_2 = \lambda_{\text{Edge1}} = \frac{1}{4} \left( \Omega_B - \sqrt{4\Omega_A^2 + \Omega_B^2} \right) = \frac{\Omega_A}{4} \left( R - \sqrt{R^2 + 4} \right) \quad (9.11)$$

$$\lambda_3 = \lambda_{\text{Edge2}} = \frac{1}{4} \left( \sqrt{4\Omega_A^2 + \Omega_B^2} - \Omega_B \right) = \frac{\Omega_A}{4} \left( \sqrt{R^2 + 4} - R \right) \quad (9.12)$$

$$\lambda_4 = \lambda_{\text{Conduction}} = \frac{1}{4} \left( \sqrt{4\Omega_A^2 + \Omega_B^2} + \Omega_B \right) = \frac{\Omega_A}{4} \left( R + \sqrt{R^2 + 4} \right), \quad (9.13)$$

where  $R = \frac{\Omega_B}{\Omega_A}$ .

It's unwieldy to write out the eigenstate solutions in full. Instead we label the coefficient of the compositions using either  $\kappa$  or  $\tau$ .

$$|\Psi_{\text{Valence}}\rangle = -\kappa |N=1\rangle + \tau |N=2\rangle - \tau |N=3\rangle + \kappa |N=4\rangle \quad (9.14)$$

$$|\Psi_{\text{Edge1}}\rangle = \tau |N=1\rangle - \kappa |N=2\rangle - \kappa |N=3\rangle + \tau |N=4\rangle \quad (9.15)$$

$$|\Psi_{\text{Edge2}}\rangle = \tau |N=1\rangle + \kappa |N=2\rangle - \kappa |N=3\rangle - \tau |N=4\rangle \quad (9.16)$$

$$|\Psi_{\text{Conduction}}\rangle = \kappa |N=1\rangle + \tau |N=2\rangle + \tau |N=3\rangle + \kappa |N=4\rangle, \quad (9.17)$$

where

$$\kappa = \frac{1}{\sqrt{R^2 + R\sqrt{R^2 + 4} + 4}} \quad (9.18)$$

$$\tau = \frac{1}{\sqrt{R^2 - R\sqrt{R^2 + 4} + 4}}. \quad (9.19)$$

# Bibliography

- [1] E. A. Cornell and C. E. Wieman, *Rev. Mod. Phys.* **74**, 875 (2002).
- [2] M. H. Anderson, J. R. Ensher, M. R. Matthews, C. E. Wieman, and E. A. Cornell, *Science* **269**, 198 (1995), <https://www.science.org/doi/pdf/10.1126/science.269.5221.198> .
- [3] K. B. Davis, M. O. Mewes, M. R. Andrews, N. J. van Druten, D. S. Durfee, D. M. Kurn, and W. Ketterle, *Phys. Rev. Lett.* **75**, 3969 (1995).
- [4] J. Huang, S. Wu, H. Zhong, and C. Lee, “Quantum metrology with cold atoms,” in *Annual Review of Cold Atoms and Molecules* (2014) Chap. 7, pp. 365–415, [https://www.worldscientific.com/doi/pdf/10.1142/9789814590174\\_0007](https://www.worldscientific.com/doi/pdf/10.1142/9789814590174_0007) .
- [5] L. Pezzè, A. Smerzi, M. K. Oberthaler, R. Schmied, and P. Treutlein, *Rev. Mod. Phys.* **90**, 035005 (2018).
- [6] D. Jaksch, *Contemporary Physics* **45**, 367 (2004), <https://doi.org/10.1080/00107510410001705486> .
- [7] I. Bloch, *Nature* **453**, 1016 (2008).
- [8] P. Scholl, M. Schuler, H. J. Williams, A. A. Eberharter, D. Barredo, K.-N. Schymik, V. Lienhard, L.-P. Henry, T. C. Lang, T. Lahaye, A. M. Läuchli, and A. Browaeys, *Nature* **595**, 233 (2021).
- [9] K. Burnett, P. S. Julienne, P. D. Lett, E. Tiesinga, and C. J. Williams, *Nature* **416**, 225 (2002).
- [10] J.-J. Zhu and X. Chen, *Phys. Rev. A* **103**, 023307 (2021).
- [11] H. Labuhn, D. Barredo, S. Ravets, S. de Léséleuc, T. Macrì, T. Lahaye, and A. Browaeys, *Nature* **534**, 667 (2016).

- 
- [12] D. Jaksch, C. Bruder, J. I. Cirac, C. W. Gardiner, and P. Zoller, *Phys. Rev. Lett.* **81**, 3108 (1998).
- [13] I. Bloch, J. Dalibard, and W. Zwerger, *Rev. Mod. Phys.* **80**, 885 (2008).
- [14] L.-M. Duan, M. D. Lukin, J. I. Cirac, and P. Zoller, *Nature* **414**, 413 (2001).
- [15] P. S. Julienne, in *Scattering*, edited by R. Pike and P. Sabatier (Academic Press, London, 2002) pp. 1043–1067.
- [16] A. Frisch, M. Mark, K. Aikawa, F. Ferlaino, J. L. Bohn, C. Makrides, A. Petrov, and S. Kotochigova, *Nature* **507**, 475 (2014).
- [17] A. V. Gorshkov, S. R. Manmana, G. Chen, E. Demler, M. D. Lukin, and A. M. Rey, *Phys. Rev. A* **84**, 033619 (2011).
- [18] V. A. M. Lewenstein, A. Sanpera, in *Ultracold Atoms in Optical Lattices* (Oxford University Press, 2017).
- [19] M. Lu, N. Q. Burdick, S. H. Youn, and B. L. Lev, *Phys. Rev. Lett.* **107**, 190401 (2011).
- [20] K. Aikawa, A. Frisch, M. Mark, S. Baier, A. Rietzler, R. Grimm, and F. Ferlaino, *Phys. Rev. Lett.* **108**, 210401 (2012).
- [21] A. Griesmaier, J. Werner, S. Hensler, J. Stuhler, and T. Pfau, *Phys. Rev. Lett.* **94**, 160401 (2005).
- [22] C. S. Adams, J. D. Pritchard, and J. P. Shaffer, *Journal of Physics B: Atomic, Molecular and Optical Physics* **53**, 012002 (2019).
- [23] X. Wu, X. Liang, Y. Tian, F. Yang, C. Chen, Y.-C. Liu, M. K. Tey, and L. You, *Chinese Physics B* **30**, 020305 (2021).
- [24] S. J. Evered, D. Bluvstein, M. Kalinowski, S. Ebadi, T. Manovitz, H. Zhou, S. H. Li, A. A. Geim, T. T. Wang, N. Maskara, H. Levine, G. Semeghini, M. Greiner, V. Vuletić, and M. D. Lukin, *Nature* **622**, 268 (2023).
- [25] R. Grimm, M. Weidemüller, and Y. B. Ovchinnikov, in *Optical Dipole Traps for Neutral Atoms*, *Advances In Atomic, Molecular, and Optical Physics*, Vol. 42, edited by B. Bederson and H. Walther (Academic Press, 2000) pp. 95–170.

- 
- [26] D. Bluvstein, H. Levine, G. Semeghini, T. T. Wang, S. Ebadi, M. Kalinowski, A. Keesling, N. Maskara, H. Pichler, M. Greiner, V. Vuletić, and M. D. Lukin, *Nature* **604**, 451 (2022).
- [27] T. Chalopin, C. Bouazza, A. Evrard, V. Makhalov, D. Dreon, J. Dalibard, L. A. Sidorenkov, and S. Nascimbene, *Nature Communications* **9**, 4955 (2018).
- [28] L. Weiss, A. Gritsch, B. Merkel, and A. Reiserer, *Optica* **8**, 40 (2021).
- [29] C. Yin, M. Rancic, G. G. de Boo, N. Stavrias, J. C. McCallum, M. J. Sellars, and S. Rogge, *Nature* **497**, 91 (2013).
- [30] Z. Zhang, M. Yuan, B. Sundar, and K. R. A. Hazzard, (2022), arXiv:2201.08463 [cond-mat.quant-gas] .
- [31] S. L. Cornish, M. R. Tarbutt, and K. R. A. Hazzard, “Quantum computation and quantum simulation with ultracold molecules,” (2024), arXiv:2401.05086 [cond-mat.quant-gas] .
- [32] A. Micheli, G. K. Brennen, and P. Zoller, *Nature Physics* **2**, 341 (2006).
- [33] R. Barnett, D. Petrov, M. Lukin, and E. Demler, *Phys. Rev. Lett.* **96**, 190401 (2006).
- [34] T. Byrnes, N. Y. Kim, K. Kusudo, and Y. Yamamoto, *Phys. Rev. B* **78**, 075320 (2008).
- [35] M. Hughes, A. U. J. Lode, D. Jaksch, and P. Morigini, *Phys. Rev. A* **107**, 033323 (2023).
- [36] A. V. Gorshkov, S. R. Manmana, G. Chen, J. Ye, E. Demler, M. D. Lukin, and A. M. Rey, *Phys. Rev. Lett.* **107**, 115301 (2011).
- [37] T. Schuster, F. Flicker, M. Li, S. Kotochigova, J. E. Moore, J. Ye, and N. Y. Yao, *Phys. Rev. A* **103**, 063322 (2021).
- [38] L. Pollet, J. D. Picon, H. P. Büchler, and M. Troyer, *Phys. Rev. Lett.* **104**, 125302 (2010).
- [39] E. Zohar, J. I. Cirac, and B. Reznik, *Reports on Progress in Physics* **79**, 014401 (2015).
- [40] Y. Bao, S. S. Yu, L. Anderegg, E. Chae, W. Ketterle, K.-K. Ni, and J. M. Doyle, *Science* **382**, 1138 (2023), <https://www.science.org/doi/pdf/10.1126/science.adf8999> .

- [41] B. Gadway and B. Yan, *Journal of Physics B: Atomic, Molecular and Optical Physics* **49**, 152002 (2016).
- [42] C. M. Holland, Y. Lu, and L. W. Cheuk, *Science* **382**, 1143 (2023), <https://www.science.org/doi/pdf/10.1126/science.adf4272> .
- [43] B. Yan, S. A. Moses, B. Gadway, J. P. Covey, K. R. A. Hazzard, A. M. Rey, D. S. Jin, and J. Ye, *Nature* **501**, 521 (2013).
- [44] L. Christakis, J. S. Rosenberg, R. Raj, S. Chi, A. Morningstar, D. A. Huse, Z. Z. Yan, and W. S. Bakr, *Nature* **614**, 64 (2023).
- [45] R. Bause, M. Li, A. Schindewolf, X.-Y. Chen, M. Duda, S. Kotochigova, I. Bloch, and X.-Y. Luo, *Phys. Rev. Lett.* **125**, 023201 (2020).
- [46] A. J. Park, L. R. B. Picard, G. E. Patenotte, J. T. Zhang, T. Rosenband, and K.-K. Ni, *Phys. Rev. Lett.* **131**, 183401 (2023).
- [47] S. Burchesky, L. Anderegg, Y. Bao, S. S. Yu, E. Chae, W. Ketterle, K.-K. Ni, and J. M. Doyle, *Phys. Rev. Lett.* **127**, 123202 (2021).
- [48] W. G. Tobias, K. Matsuda, J.-R. Li, C. Miller, A. N. Carroll, T. Bilitewski, A. M. Rey, and J. Ye, *Science* **375**, 1299 (2022), <https://www.science.org/doi/pdf/10.1126/science.abn8525> .
- [49] J. A. Blackmore, L. Caldwell, P. D. Gregory, E. M. Bridge, R. Sawant, J. Aldegunde, J. Mur-Petit, D. Jaksch, J. M. Hutson, B. E. Sauer, M. R. Tarbutt, and S. L. Cornish, *Quan. Sci. Technol.* **4**, 014010 (2018).
- [50] L. Reichsöllner, A. Schindewolf, T. Takekoshi, R. Grimm, and H.-C. Nägerl, *Phys. Rev. Lett.* **118**, 073201 (2017).
- [51] M. D. Di Rosa, *The European Physical Journal D - Atomic, Molecular, Optical and Plasma Physics* **31**, 395 (2004).
- [52] C. Adams and E. Riis, *Progress in Quantum Electronics* **21**, 1 (1997).
- [53] H. J. Williams, S. Truppe, M. Hambach, L. Caldwell, N. J. Fitch, E. A. Hinds, B. E. Sauer, and M. R. Tarbutt, *New Journal of Physics* **19**, 113035 (2017).
- [54] J. F. Barry, D. J. McCarron, E. B. Norrgard, M. H. Steinecker, and D. DeMille, *Nature* **512**, 286 (2014).

- [55] S. Truppe, H. J. Williams, M. Hambach, L. Caldwell, N. J. Fitch, E. A. Hinds, B. E. Sauer, and M. R. Tarbutt, *Nature Physics* **13**, 1173 (2017).
- [56] L. Anderegg, B. L. Augenbraun, E. Chae, B. Hemmerling, N. R. Hut- zler, A. Ravi, A. Collopy, J. Ye, W. Ketterle, and J. M. Doyle, *Phys. Rev. Lett.* **119**, 103201 (2017).
- [57] A. L. Collopy, S. Ding, Y. Wu, I. A. Finneran, L. Anderegg, B. L. Augenbraun, J. M. Doyle, and J. Ye, *Phys. Rev. Lett.* **121**, 213201 (2018).
- [58] J. Lim, J. R. Almond, M. A. Trigatzis, J. A. Devlin, N. J. Fitch, B. E. Sauer, M. R. Tarbutt, and E. A. Hinds, *Phys. Rev. Lett.* **120**, 123201 (2018).
- [59] R. L. McNally, I. Kozyryev, S. Vazquez-Carson, K. Wenz, T. Wang, and T. Zelevinsky, *New Journal of Physics* **22**, 083047 (2020).
- [60] B. K. Stuhl, B. C. Sawyer, D. Wang, and J. Ye, *Phys. Rev. Lett.* **101**, 243002 (2008).
- [61] S. Stellmer, B. Pasquiou, R. Grimm, and F. Schreck, *Phys. Rev. Lett.* **109**, 115302 (2012).
- [62] A. Green, J. H. See Toh, R. Roy, M. Li, S. Kotochigova, and S. Gupta, *Phys. Rev. A* **99**, 063416 (2019).
- [63] K. M. Jones, E. Tiesinga, P. D. Lett, and P. S. Julienne, *Rev. Mod. Phys.* **78**, 483 (2006).
- [64] M. Kitagawa, K. Enomoto, K. Kasa, Y. Takahashi, R. Ciuryło, P. Naidon, and P. S. Julienne, *Phys. Rev. A* **77**, 012719 (2008).
- [65] E. R. I. Abraham, W. I. McAlexander, C. A. Sackett, and R. G. Hulet, *Phys. Rev. Lett.* **74**, 1315 (1995).
- [66] M. T. Bell and T. P. Softley, *Molecular Physics* **107**, 99 (2009), <https://doi.org/10.1080/00268970902724955> .
- [67] C. A. Regal, C. Ticknor, J. L. Bohn, and D. S. Jin, *Nature* **424**, 47 (2003).

- [68] C. Zener and R. H. Fowler, Proceedings of the Royal Society of London. Series A, Containing Papers of a Mathematical and Physical Character **137**, 696 (1932), <https://royalsocietypublishing.org/doi/pdf/10.1098/rspa.1932.0165> .
- [69] C. Ospelkaus, S. Ospelkaus, L. Humbert, P. Ernst, K. Sengstock, and K. Bongs, Phys. Rev. Lett. **97**, 120402 (2006).
- [70] K. Aikawa, D. Akamatsu, J. Kobayashi, M. Ueda, T. Kishimoto, and S. Inouye, New Journal of Physics **11**, 055035 (2009).
- [71] T. Takekoshi, M. Debatin, R. Rameshan, F. Ferlaino, R. Grimm, H.-C. Nägerl, C. R. Le Sueur, J. M. Hutson, P. S. Julienne, S. Kotochigova, and E. Tiemann, Phys. Rev. A **85**, 032506 (2012).
- [72] M. P. Köppinger, D. J. McCarron, D. L. Jenkin, P. K. Molony, H.-W. Cho, S. L. Cornish, C. R. Le Sueur, C. L. Blackley, and J. M. Hutson, Phys. Rev. A **89**, 033604 (2014).
- [73] J. W. Park, S. A. Will, and M. W. Zwierlein, Phys. Rev. Lett. **114**, 205302 (2015).
- [74] R. Bause, A. Kamijo, X.-Y. Chen, M. Duda, A. Schindewolf, I. Bloch, and X.-Y. Luo, Phys. Rev. A **104**, 043321 (2021).
- [75] M.-J. Zhu, H. Yang, L. Liu, D.-C. Zhang, Y.-X. Liu, J. Nan, J. Rui, B. Zhao, J.-W. Pan, and E. Tiemann, Phys. Rev. A **96**, 062705 (2017).
- [76] T. A. Schulze, T. Hartmann, K. K. Voges, M. W. Gempel, E. Tiemann, A. Zenesini, and S. Ospelkaus, Phys. Rev. A **97**, 023623 (2018).
- [77] F. Wang, X. Li, D. Xiong, and D. Wang, Journal of Physics B: Atomic, Molecular and Optical Physics **49**, 015302 (2015).
- [78] W. B. Cairncross, J. T. Zhang, L. R. B. Picard, Y. Yu, K. Wang, and K.-K. Ni, Phys. Rev. Lett. **126**, 123402 (2021).
- [79] A.-C. Voigt, M. Taglieber, L. Costa, T. Aoki, W. Wieser, T. W. Hänsch, and K. Dieckmann, Phys. Rev. Lett. **102**, 020405 (2009).
- [80] M.-S. Heo, T. T. Wang, C. A. Christensen, T. M. Rvachov, D. A. Cotta, J.-H. Choi, Y.-R. Lee, and W. Ketterle, Phys. Rev. A **86**, 021602 (2012).

- 
- [81] A. V. Gorshkov, S. R. Manmana, G. Chen, J. Ye, E. Demler, M. D. Lukin, and A. M. Rey, *Phys. Rev. Lett.* **107**, 115301 (2011).
- [82] A. V. Gorshkov, S. R. Manmana, G. Chen, E. Demler, M. D. Lukin, and A. M. Rey, *Phys. Rev. A* **84**, 033619 (2011).
- [83] T. Bilitewski, L. De Marco, J.-R. Li, K. Matsuda, W. G. Tobias, G. Valtolina, J. Ye, and A. M. Rey, *Phys. Rev. Lett.* **126**, 113401 (2021).
- [84] S. A. Moses, *A quantum gas of polar molecules in an optical lattice*, PhD thesis, University of Colorado (2016).
- [85] J.-R. Li, K. Matsuda, C. Miller, A. N. Carroll, W. G. Tobias, J. S. Higgins, and J. Ye, *Nature* **614**, 70 (2023).
- [86] A. Micheli, G. Pupillo, H. P. Büchler, and P. Zoller, *Phys. Rev. A* **76**, 043604 (2007).
- [87] E. Lake, M. Hermele, and T. Senthil, *Phys. Rev. B* **106**, 064511 (2022).
- [88] B. Capogrosso-Sansone, C. Trefzger, M. Lewenstein, P. Zoller, and G. Pupillo, *Phys. Rev. Lett.* **104**, 125301 (2010).
- [89] K. R. A. Hazzard and B. Gadway, *Physics Today* **76**, 62 (2023), [https://pubs.aip.org/physicstoday/article-pdf/76/4/62/16779074/62\\_1\\_online.pdf](https://pubs.aip.org/physicstoday/article-pdf/76/4/62/16779074/62_1_online.pdf).
- [90] T. Ozawa and H. M. Price, *Nature Reviews Physics* **1**, 349 (2019).
- [91] X. Zhou, J.-S. Pan, and S. Jia, *Phys. Rev. B* **107**, 054105 (2023).
- [92] S. K. Kanungo, J. D. Whalen, Y. Lu, M. Yuan, S. Dasgupta, F. B. Dunning, K. R. A. Hazzard, and T. C. Killian, *Nature Communications* **13**, 972 (2022).
- [93] M. Lohse, C. Schweizer, H. M. Price, O. Zilberberg, and I. Bloch, *Nature* **553**, 55 (2018).
- [94] H. M. Price, O. Zilberberg, T. Ozawa, I. Carusotto, and N. Goldman, *Phys. Rev. Lett.* **115**, 195303 (2015).
- [95] M. Hughes, M. D. Frye, R. Sawant, G. Bhole, J. A. Jones, S. L. Cornish, M. R. Tarbutt, J. M. Hutson, D. Jaksch, and J. Mur-Petit, *Phys. Rev. A* **101**, 062308 (2020).
- [96] D. DeMille, *Phys. Rev. Lett.* **88**, 067901 (2002).

- [97] K.-K. Ni, T. Rosenband, and D. D. Grimes, *Chem. Sci.* **9**, 6830 (2018).
- [98] L. Gyongyosi and S. Imre, *Scientific Reports* **11**, 5172 (2021).
- [99] R. Sawant, J. A. Blackmore, P. D. Gregory, J. Mur-Petit, D. Jaksch, J. Aldegunde, J. M. Hutson, M. R. Tarbutt, and S. L. Cornish, *New J. Phys.* **22**, 013027 (2020).
- [100] D. Bluvstein, S. J. Evered, A. A. Geim, S. H. Li, H. Zhou, T. Manovitz, S. Ebadi, M. Cain, M. Kalinowski, D. Hangleiter, J. P. Bonilla Ataides, N. Maskara, I. Cong, X. Gao, P. Sales Rodriguez, T. Karolyshyn, G. Semeghini, M. J. Gullans, M. Greiner, V. Vuletić, and M. D. Lukin, *Nature* **626**, 58 (2024).
- [101] J. A. Blackmore, P. D. Gregory, S. L. Bromley, and S. L. Cornish, *Phys. Chem. Chem. Phys.* **22**, 27529 (2020).
- [102] T. E. Wall, *Journal of Physics B: Atomic, Molecular and Optical Physics* **49**, 243001 (2016).
- [103] A. D. Sakharov, *Soviet Physics Uspekhi* **34**, 392 (1991).
- [104] V. Andreev, D. G. Ang, D. DeMille, J. M. Doyle, G. Gabrielse, J. Haefner, N. R. Hutzler, Z. Lasner, C. Meisenhelder, B. R. O’Leary, C. D. Panda, A. D. West, E. P. West, X. Wu, and A. C. M. E. Collaboration, *Nature* **562**, 355 (2018).
- [105] J. J. Hudson, D. M. Kara, I. J. Smallman, B. E. Sauer, M. R. Tarbutt, and E. A. Hinds, *Nature* **473**, 493 (2011).
- [106] T. S. Roussy, L. Caldwell, T. Wright, W. B. Cairncross, Y. Shagam, K. B. Ng, N. Schlossberger, S. Y. Park, A. Wang, J. Ye, and E. A. Cornell, *Science* **381**, 46 (2023), <https://www.science.org/doi/pdf/10.1126/science.adg4084> .
- [107] D. J. McCarron, *A Quantum Degenerate Mixture of  $87^{Rb}$  and  $133Cs$* , PhD thesis, Durham University (2011).
- [108] H. W. Cho, D. J. McCarron, D. L. Jenkin, M. P. Köppinger, and S. L. Cornish, *The European Physical Journal D* **65**, 125 (2011).
- [109] D. J. McCarron, H. W. Cho, D. L. Jenkin, M. P. Köppinger, and S. L. Cornish, *Phys. Rev. A* **84**, 011603 (2011).

- 
- [110] D. L. Jenkin, *Feshbach spectroscopy of an ultracold Rb-Cs mixture*, PhD thesis, Durham University (2012).
- [111] M. P. Köppinger, *Creation of ultracold RbCs molecules*, PhD thesis, Durham University (2014).
- [112] M. P. Köppinger, D. J. McCarron, D. L. Jenkin, P. K. Molony, H.-W. Cho, S. L. Cornish, C. R. Le Sueur, C. Blackley, and J. M. Hutson, *Phys. Rev. A* **89**, 033604 (2014).
- [113] P. K. Molony, *Creation of ultracold polar ground-state RbCs molecules*, PhD thesis, Durham University (2016).
- [114] P. K. Molony, P. D. Gregory, Z. Ji, B. Lu, M. P. Köppinger, C. R. Le Sueur, C. L. Blackley, J. M. Hutson, and S. L. Cornish, *Phys. Rev. Lett.* **113**, 255301 (2014).
- [115] P. K. Molony, P. D. Gregory, A. Kumar, C. R. Le Sueur, J. M. Hutson, and S. L. Cornish, *ChemPhysChem.* **17**, 3811 (2016).
- [116] P. K. Molony, A. Kumar, P. D. Gregory, R. Kliese, T. Puppe, C. R. Le Sueur, J. Aldegunde, J. M. Hutson, and S. L. Cornish, *Phys. Rev. A* **94**, 022507 (2016).
- [117] P. Gregory, *Coherent control of ultracold polar molecules*, PhD thesis, University of Durham (2018).
- [118] P. D. Gregory, J. Aldegunde, J. M. Hutson, and S. L. Cornish, *Phys. Rev. A* **94**, 041403 (2016).
- [119] P. D. Gregory, J. A. Blackmore, J. Aldegunde, J. M. Hutson, and S. L. Cornish, *Phys. Rev. A* **96**, 021402 (2017).
- [120] J. A. Blackmore, R. Sawant, P. D. Gregory, S. L. Bromley, J. Aldegunde, J. M. Hutson, and S. L. Cornish, *Phys. Rev. A* **102**, 053316 (2020).
- [121] P. D. Gregory, L. M. Fernley, A. L. Tao, S. L. Bromley, J. Stepp, Z. Zhang, S. Kotochigova, K. R. A. Hazzard, and S. L. Cornish, *Nature Physics* (2024), 10.1038/s41567-023-02328-5.
- [122] P. D. Gregory, J. A. Blackmore, S. L. Bromley, J. M. Hutson, and S. L. Cornish, *Nature Physics* **17**, 1149 (2021).

- [123] A. Das, P. D. Gregory, T. Takekoshi, L. Fernley, M. Landini, J. M. Hutson, S. L. Cornish, and H.-C. Nägerl, *SciPost Phys.* **15**, 220 (2023).
- [124] J. M. Brown and A. Carrington, *Rotational Spectroscopy of Diatomic Molecules*, Cambridge Molecular Science (Cambridge University Press, 2003).
- [125] E. Nikitin and R. Zare, *Molecular Physics* **82**, 85 (1994), <https://doi.org/10.1080/00268979400100074> .
- [126] K.-K. Ni, *A Quantum Gas of Polar Molecules*, PhD thesis, University of Colorado (2009).
- [127] J. Adams, in *Encyclopedia of Materials: Science and Technology*, edited by K. J. Buschow, R. W. Cahn, M. C. Flemings, B. Ilschner, E. J. Kramer, S. Mahajan, and P. Veysseyre (Elsevier, Oxford, 2001) pp. 763–767.
- [128] C. Fellows, R. Gutterres, A. Campos, J. Vergès, and C. Amiot, *Journal of Molecular Spectroscopy* **197**, 19 (1999).
- [129] T. Bergeman, C. E. Fellows, R. F. Gutterres, and C. Amiot, *Phys. Rev. A* **67**, 050501 (2003).
- [130] O. Docenko, M. Tamanis, R. Ferber, T. Bergeman, S. Kotochigova, A. V. Stolyarov, A. de Faria Nogueira, and C. E. Fellows, *Phys. Rev. A* **81**, 042511 (2010).
- [131] J. M. Hollas, in *Modern Spectroscopy*, edited by J. Wiley and I. Sons (John Wiley and Sons Ltd, West Sussex PO19 8SQ, England, 2001).
- [132] T. E. Wall, J. F. Kanem, J. J. Hudson, B. E. Sauer, D. Cho, M. G. Boshier, E. A. Hinds, and M. R. Tarbutt, *Phys. Rev. A* **78**, 062509 (2008).
- [133] V. Zhelyazkova, A. Cournol, T. E. Wall, A. Matsushima, J. J. Hudson, E. A. Hinds, M. R. Tarbutt, and B. E. Sauer, *Phys. Rev. A* **89**, 053416 (2014).
- [134] R. J. Hendricks, D. A. Holland, S. Truppe, B. E. Sauer, and M. R. Tarbutt, *Frontiers in Physics* **2** (2014), 10.3389/fphy.2014.00051.
- [135] H. Fahs, A. R. Allouche, M. Korek, and M. Aubert-Frécon, *Journal of Physics B: Atomic, Molecular and Optical Physics* **35**, 1501 (2002).

- [136] P. D. Gregory, J. Aldegunde, J. M. Hutson, and S. L. Cornish, *Phys. Rev. A* **94**, 041403(R) (2016).
- [137] P. D. W. Demtröder, in *Atoms, Molecules and Photons: n Introduction to Atomic-, Molecular and Quantum-Physics* (Springer Berlin Heidelberg New York).
- [138] G. Herzberg, in *Spectra of Diatomic Molecules, 2nd ed., Molecular Spectra and Molecular Structure, Vol. 1* (D.Van Nostrand Company Inc., 1950).
- [139] J. Aldegunde, B. A. Rivington, P. S. Żuchowski, and J. M. Hutson, *Phys. Rev. A* **78**, 033434 (2008).
- [140] J. Aldegunde and J. M. Hutson, *Phys. Rev. A* **96**, 042506 (2017).
- [141] J. A. Blackmore, P. D. Gregory, J. M. Hutson, and S. L. Cornish, *Computer Physics Communications* **282**, 108512 (2023).
- [142] J. Blackmore and T. Hepworth, “Diatomic-py,” <https://github.com/durham-qlm/diatomic-py?tab=readme-ov-file> (2020).
- [143] P. D. Gregory, J. A. Blackmore, J. Aldegunde, J. M. Hutson, and S. L. Cornish, *Phys. Rev. A* **96**, 021402(R) (2017).
- [144] T. Hepworth, *Controlling Quantum Synthetic Dimensions with Python*, MSci dissertation, University of Durham (2023).
- [145] P. K. Molony, P. D. Gregory, Z. Ji, B. Lu, M. P. Köppinger, C. R. Le Sueur, C. L. Blackley, J. M. Hutson, and S. L. Cornish, *Phys. Rev. Lett.* **113**, 255301 (2014).
- [146] T. Takekoshi, L. Reichsöllner, A. Schindewolf, J. M. Hutson, C. R. Le Sueur, O. Dulieu, F. Ferlaino, R. Grimm, and H.-C. Nägerl, *Phys. Rev. Lett.* **113**, 205301 (2014).
- [147] M. L. Wall, K. Maeda, and L. D. Carr, *New Journal of Physics* **17**, 025001 (2015).
- [148] S. A. Malininskaya and I. Novikova, *From Atomic to Mesoscale* (WORLD SCIENTIFIC, 2015) <https://www.worldscientific.com/doi/pdf/10.1142/9613> .
- [149] M. L. Harris, *Realisation of a cold mixture of rubidium and caesium*, PhD thesis, Durham University (2008).

- [150] P. Tierney, *Magnetic Trapping of an Ultracold  $^{87}\text{Rb}$  -  $^{133}\text{Cs}$  Atomic Mixture*, PhD thesis, Durham University (2009).
- [151] J. Blackmore, *Coherence and Collisions in Ultracold  $^{87}\text{Rb}^{133}\text{Cs}$  Molecules*, PhD thesis, University of Durham (2020).
- [152] J. Herbig, T. Kraemer, M. Mark, T. Weber, C. Chin, H.-C. Nägerl, and R. Grimm, *Science* **301**, 1510 (2003), <https://www.science.org/doi/pdf/10.1126/science.1088876> .
- [153] M. Debatin, T. Takekoshi, R. Rameshan, L. Reichsöllner, F. Ferlaino, R. Grimm, R. Vexiau, N. Bouloufa, O. Dulieu, and H.-C. Nägerl, *Phys. Chem. Chem. Phys.* **13**, 18926 (2011).
- [154] P. K. Molony, P. D. Gregory, A. Kumar, C. R. LeSueur, J. M. Hutson, and S. L. Cornish, *ChemPhysChem* **17**, 3811 (2016), <https://chemistry-europe.onlinelibrary.wiley.com/doi/pdf/10.1002/cphc.201600501> .
- [155] P. D. Gregory, P. K. Molony, M. P. Köppinger, A. Kumar, Z. Ji, B. Lu, A. L. Marchant, and S. L. Cornish, *New J. Phys.* **17**, 055006 (2015).
- [156] “Agilent high and ultra-high vacuum for science research,” [https://www.agilent.com/cs/library/training/Public/UHV\\_Seminar\\_Handbook.pdf](https://www.agilent.com/cs/library/training/Public/UHV_Seminar_Handbook.pdf), accessed: 03-04-2024.
- [157] “Leybold vacuum bake out: its importance and implementation,” <https://www.leybold.com/en-uk/knowledge/blog/vacuum-bake-out>, accessed: 03-04-2024.
- [158] J. Lin, G. Chen, M. Jin, Z. Shi, F. Deng, W. Zhang, G. Quéméner, T. Shi, S. Yi, and D. Wang, *Phys. Rev. X* **13**, 031032 (2023).
- [159] L. Anderegg, S. Burchesky, Y. Bao, S. S. Yu, T. Karman, E. Chae, K.-K. Ni, W. Ketterle, and J. M. Doyle, *Science* **373**, 779 (2021), <https://www.science.org/doi/pdf/10.1126/science.abg9502> .
- [160] T. Karman and J. M. Hutson, *Phys. Rev. Lett.* **121**, 163401 (2018).
- [161] A. Schindewolf, R. Bause, X.-Y. Chen, M. Duda, T. Karman, I. Bloch, and X.-Y. Luo, *Nature* **607**, 677 (2022).
- [162] N. Bigagli, W. Yuan, S. Zhang, B. Bulatovic, T. Karman, I. Stevenson, and S. Will, “Observation of bose-einstein condensation of dipolar molecules,” (2023), arXiv:2312.10965 [cond-mat.quant-gas] .

- [163] C. A. Balanis, in *Antenna Theory: Analysis and Design, 4th Edition* (Wiley, 2016) pp. 32–34.
- [164] H. M. Aumann and K. A. Tuttle, AMTA 2016 Proceedings , 1 (2016).
- [165] C. J. Foot, *Atomic physics*, Oxford master series in atomic, optical, and laser physics (Oxford University Press, Oxford, 2007).
- [166] J. A. Blackmore, R. Sawant, P. D. Gregory, S. L. Bromley, J. Aldegunde, J. M. Hutson, and S. L. Cornish, *Phys. Rev. A* **102**, 053316 (2020).
- [167] M. Takamoto, F.-L. Hong, R. Higashi, and H. Katori, *Nature* **435**, 321 (2005).
- [168] S. S. Kondov, C.-H. Lee, K. H. Leung, C. Liedl, I. Majewska, R. Moszynski, and T. Zelevinsky, *Nature Physics* **15**, 1118 (2019).
- [169] K. H. Leung, B. Iritani, E. Tiberi, I. Majewska, M. Borkowski, R. Moszynski, and T. Zelevinsky, *Phys. Rev. X* **13**, 011047 (2023).
- [170] F. Seeßelberg, X.-Y. Luo, M. Li, R. Bause, S. Kotochigova, I. Bloch, and C. Gohle, *Phys. Rev. Lett.* **121**, 253401 (2018).
- [171] S. Kotochigova, Q. Guan, V. Scarola, B. DeMarco, and B. Gadway, (2023), arXiv:2310.16215 [quant-ph] .
- [172] Q. Guan, S. L. Cornish, and S. Kotochigova, *Phys. Rev. A* **103**, 043311 (2021).
- [173] S. Kotochigova and E. Tiesinga, *Phys. Rev. A* **73**, 041405(R) (2006).
- [174] R. Vexiau, D. Borsalino, M. Lepers, A. Orbán, M. Aymar, and O. Dulieu, *Int. Rev. Phys. Chem.* **36**, 709 (2017).
- [175] M. Li, A. Petrov, C. Makrides, E. Tiesinga, and S. Kotochigova, *Phys. Rev. A* **95**, 063422 (2017).
- [176] S. Subhankar, A. Restelli, Y. Wang, S. L. Rolston, and J. V. Porto, *Rev. Sci. Instrum.* **90**, 043115 (2019).
- [177] B. E. Jones, J. W. Thomas, A. Selyem, S. Jones, D. Bremner, L. A. Downes, P. A. Marsden, P. Brown, and K. J. Weatherill, in *Quantum Sensing and Nano Electronics and Photonics XVIII*, Vol. PC12009, edited by M. Razeghi, G. A. Khodaparast, and M. S. Vitiello, International Society for Optics and Photonics (SPIE, 2022) p. PC12009J.

- [178] D. J. McCarron, S. A. King, and S. L. Cornish, *Measurement Science and Technology* **19**, 105601 (2008).
- [179] D. W. Preston, *American Journal of Physics* **64**, 1432 (1996), [https://pubs.aip.org/aapt/ajp/article-pdf/64/11/1432/11979448/1432\\_1\\_online.pdf](https://pubs.aip.org/aapt/ajp/article-pdf/64/11/1432/11979448/1432_1_online.pdf) .
- [180] J. M. Hutson and C. R. Le Sueur, *Computer Physics Communications* **241**, 9 (2019).
- [181] S. Kotochigova and E. Tiesinga, *The Journal of Chemical Physics* **123**, 174304 (2005), [https://pubs.aip.org/aip/jcp/article-pdf/doi/10.1063/1.2107607/13577205/174304\\_1\\_online.pdf](https://pubs.aip.org/aip/jcp/article-pdf/doi/10.1063/1.2107607/13577205/174304_1_online.pdf) .
- [182] R. Grimm, M. Weidemüller, and Y. B. Ovchinnikov, “Optical dipole traps for neutral atoms,” (1999), arXiv:physics/9902072 [physics.atom-ph] .
- [183] O. Docenko, M. Tamanis, R. Ferber, T. Bergeman, S. Kotochigova, A. V. Stoljarov, A. de Faria Nogueira, and C. E. Fellows, *Phys. Rev. A* **81**, 042511 (2010).
- [184] P. D. Gregory, J. A. Blackmore, S. L. Bromley, and S. L. Cornish, *Phys. Rev. Lett.* **124**, 163402 (2020).
- [185] P. D. Gregory, M. D. Frye, J. A. Blackmore, E. M. Bridge, R. Sawant, J. M. Hutson, and S. L. Cornish, *Nature Communications* **10**, 3104 (2019).
- [186] S. F. Yelin, K. Kirby, and R. Côté, *Phys. Rev. A* **74**, 050301 (2006).
- [187] Y. L. Zhou, M. Ortner, and P. Rabl, *Phys. Rev. A* **84**, 052332 (2011).
- [188] K. R. A. Hazzard, S. R. Manmana, M. Foss-Feig, and A. M. Rey, *Phys. Rev. Lett.* **110**, 075301 (2013).
- [189] B. Sundar, B. Gadway, and K. R. A. Hazzard, *Sci. Rep.* **8**, 3422 (2018).
- [190] B. Sundar, M. Thibodeau, Z. Wang, B. Gadway, and K. R. A. Hazzard, *Phys. Rev. A* **99**, 013624 (2019).
- [191] C. Feng, H. Manetsch, V. G. Rousseau, K. R. A. Hazzard, and R. Scalettar, *Phys. Rev. A* **105**, 063320 (2022).
- [192] Y. Bao, S. S. Yu, L. Anderegg, E. Chae, W. Ketterle, K.-K. Ni, and J. M. Doyle, arXiv:2211.09780 (2022).

- [193] C. M. Holland, Y. Lu, and L. W. Cheuk, arXiv:2210.06309 (2022).
- [194] P. D. Gregory, J. A. Blackmore, S. L. Bromley, and S. L. Cornish, Phys. Rev. Lett. **124**, 163402 (2020).
- [195] G. J. Feldman and R. D. Cousins, Phys. Rev. D **57**, 3873 (1998).
- [196] I. Hughes and T. Hase, *Measurements and Their Uncertainties: A Practical Guide to Modern Error Analysis* (OUP Oxford, 2010).
- [197] B. Efron and R. J. Tibshirani, *An Introduction to the Bootstrap*, Monographs on Statistics and Applied Probability No. 57 (Chapman & Hall/CRC, Boca Raton, Florida, USA, 1993).
- [198] K. R. A. Hazzard, B. Gadway, M. Foss-Feig, B. Yan, S. A. Moses, J. P. Covey, N. Y. Yao, M. D. Lukin, J. Ye, D. S. Jin, and A. M. Rey, Phys. Rev. Lett. **113**, 195302 (2014).
- [199] L. Cardarelli, S. Julià-Farré, M. Lewenstein, A. Dauphin, and M. Müller, Quantum Science and Technology **8**, 025018 (2023).
- [200] M. Greiner, O. Mandel, T. Esslinger, T. W. Hänsch, and I. Bloch, Nature **415**, 39 (2002).
- [201] T. Volz, N. Syassen, D. M. Bauer, E. Hansis, S. Dürr, and G. Rempe, Nature Physics **2**, 692 (2006).
- [202] S. B. Roy, in *Mott Insulators*, 2053-2563 (IOP Publishing, 2019) pp. 3-1 to 3-35.
- [203] S. A. Moses, J. P. Covey, M. T. Miecnikowski, B. Yan, B. Gadway, J. Ye, and D. S. Jin, Science **350**, 659 (2015), <https://www.science.org/doi/pdf/10.1126/science.aac6400> .
- [204] F. Riboli and M. Modugno, Phys. Rev. A **65**, 063614 (2002).
- [205] S. B. Papp, J. M. Pino, and C. E. Wieman, Phys. Rev. Lett. **101**, 040402 (2008).
- [206] D. van Oosten, P. van der Straten, and H. T. C. Stoof, Phys. Rev. A **63**, 053601 (2001).
- [207] P. O. Fedichev, M. W. Reynolds, and G. V. Shlyapnikov, Phys. Rev. Lett. **77**, 2921 (1996).

- [208] F. Lang, P. v. d. Straten, B. Brandstätter, G. Thalhammer, K. Winkler, P. S. Julienne, R. Grimm, and J. Hecker Denschlag, *Nature Physics* **4**, 223 (2008).
- [209] F. Lang, *Coherent transfer of Ultracold Molecules: From weakly to deeply bound*, PhD thesis, University of Innsbruck (2009).
- [210] L. T. A. Ho and L. F. Chibotaru, *Phys. Chem. Chem. Phys.* **16**, 6942 (2014).
- [211] L. Liu, D.-C. Zhang, H. Yang, Y.-X. Liu, J. Nan, J. Rui, B. Zhao, and J.-W. Pan, *Phys. Rev. Lett.* **122**, 253201 (2019).
- [212] L. Yuan, Q. Lin, M. Xiao, and S. Fan, *Optica* **5**, 1396 (2018).
- [213] A. Celi, P. Massignan, J. Ruseckas, N. Goldman, I. B. Spielman, G. Juzeliūnas, and M. Lewenstein, *Phys. Rev. Lett.* **112**, 043001 (2014).
- [214] H. M. Price, T. Ozawa, and N. Goldman, *Phys. Rev. A* **95**, 023607 (2017).
- [215] O. Boada, A. Celi, J. I. Latorre, and M. Lewenstein, *Phys. Rev. Lett.* **108**, 133001 (2012).
- [216] T. Ozawa, H. M. Price, N. Goldman, O. Zilberberg, and I. Carusotto, *Phys. Rev. A* **93**, 043827 (2016).
- [217] M. Mancini, G. Pagano, G. Cappellini, L. Livi, M. Rider, J. Catani, C. Sias, P. Zoller, M. Inguscio, M. Dalmondo, and L. Fallani, *Science* **349**, 1510 (2015), <https://www.science.org/doi/pdf/10.1126/science.aaa8736> .
- [218] C. Braun, R. Saint-Jalm, A. Hesse, J. Arceri, I. Bloch, and M. Aidelsburger, (2023), arXiv:2304.01980 [cond-mat.quant-gas] .
- [219] N. Goldman, J. Dalibard, A. Dauphin, F. Gerbier, M. Lewenstein, P. Zoller, and I. B. Spielman, *Proceedings of the National Academy of Sciences* **110**, 6736 (2013), <https://www.pnas.org/doi/pdf/10.1073/pnas.1300170110> .
- [220] M. Hafezi, S. Mittal, J. Fan, A. Migdall, and J. M. Taylor, *Nature Photonics* **7**, 1001 (2013).

- 
- [221] W. P. Su, J. R. Schrieffer, and A. J. Heeger, *Phys. Rev. Lett.* **42**, 1698 (1979).
- [222] W. P. Su, J. R. Schrieffer, and A. J. Heeger, *Phys. Rev. B* **22**, 2099 (1980).
- [223] Z. Fedorova (Cherpakova), C. Jörg, C. Dauer, F. Letscher, M. Fleischhauer, S. Eggert, S. Linden, and G. von Freymann, *Light: Science & Applications* **8**, 63 (2019).
- [224] D. Xie, W. Gou, T. Xiao, B. Gadway, and B. Yan, *Quantum Information* **5**, 55 (2019).
- [225] Z. Wang, X. Wang, Z. Hu, D. Bongiovanni, D. Jukić, L. Tang, D. Song, R. Morandotti, Z. Chen, and H. Buljan, *Nature Physics* **19**, 992 (2023).
- [226] M. S. Safronova, B. Arora, and C. W. Clark, *Phys. Rev. A* **73**, 022505 (2006).
- [227] S. V. Syzranov, M. L. Wall, V. Gurarie, and A. M. Rey, *Nature Communications* **5**, 5391 (2014).
- [228] B. Yang, H. Sun, R. Ott, H.-Y. Wang, T. V. Zache, J. C. Halimeh, Z.-S. Yuan, P. Hauke, and J.-W. Pan, *Nature* **587**, 392 (2020).
- [229] W. C. Chung, J. de Hond, J. Xiang, E. Cruz-Colón, and W. Ketterle, *Phys. Rev. Lett.* **126**, 163203 (2021).
- [230] P. B. Melo, S. a. A. S. Júnior, W. Chen, R. Mondaini, and T. Paiva, *Phys. Rev. B* **108**, 195151 (2023).